University of Texas at El Paso
DigitalCommons@UTEP

Open Access Theses & Dissertations

2017-01-01

Comprehensive Finite Element Modeling Of Ti-6Al-4V Cellular Solids Fabricated By Electron Beam Melting

Edel Arrieta
University of Texas at El Paso, edelarrieta@gmail.com

Follow this and additional works at: https://digitalcommons.utep.edu/open_etd

 Part of the Materials Science and Engineering Commons, Mechanical Engineering Commons, and the Mechanics of Materials Commons

Recommended Citation
Arrieta, Edel, "Comprehensive Finite Element Modeling Of Ti-6Al-4V Cellular Solids Fabricated By Electron Beam Melting" (2017). *Open Access Theses & Dissertations*. 600.
https://digitalcommons.utep.edu/open_etd/600

This is brought to you for free and open access by DigitalCommons@UTEP. It has been accepted for inclusion in Open Access Theses & Dissertations by an authorized administrator of DigitalCommons@UTEP. For more information, please contact lweber@utep.edu.

COMPREHENSIVE FINITE ELEMENT MODELING OF Ti-6Al-4V CELLULAR SOLIDS FABRICATED BY ELECTRON BEAM MELTING

EDEL ARRIETA

Doctoral Program in Civil Engineering

APPROVED:

Cesar Carrasco, Ph.D., Chair

Ryan B. Wicker, Ph.D.

Calvin Stewart, Ph.D.

Carlos Ferregut, Ph.D.

Ramana Chintalapalle, Ph.D.

Charles Ambler, Ph.D.
Dean of the Graduate School

Copyright ©

by

Edel Arrieta

2017

COMPREHENSIVE FINITE ELEMENT MODELING OF Ti-6Al-4V CELLULAR SOLIDS FABRICATED BY ELECTRON BEAM MELTING

by

EDEL ARRIETA, M.S. in Civil Engineering

DISSERTATION

Presented to the Faculty of the Graduate School of

The University of Texas at El Paso

in Partial Fulfillment

of the Requirements

for the Degree of

Doctor of Philosophy

Department of Civil Engineering

THE UNIVERSITY OF TEXAS AT EL PASO

May 2017

Acknowledgements

I wish to tank Dr. Cesar Carrasco for directing this dissertation, for his interest and support during the accomplishment of the work presented herein; thank you!

Special thanks and appreciation is expressed to Dr. Ryan Wicker and M.S.M.M.E. Jorge Mireles, Director and Research Manager, respectively, of the W.M. Keck Center for 3D Innovation at The University of Texas at El Paso. Without their unconditional support, encouragement and interest, it would have been impossible to accomplish this work; thank you!

I wish to thank M.S.M.E. David Espalin, manager, and all the staff and friends at the Keck Center for amazingly welcoming me to the center, making me part of it, and giving me access to the facilities. Thanks to Israel Segura for the fabrication of the specimens and Jose Gonzalez for his support.

I wish to express total gratitude to Dr. Calvin Stewart for his trust in me by providing me with practically unrestricted access to his testing equipment at cSERT Challenger-Columbia Lab, DIC system and instrumentation; thanks for his support, encouragement and interest shown all the time. Without his support, the significance of the present work would have been impossible to achieve.

I would also like to thank Dr. Carlos Ferregut for congratulating and cheering me when external recognition was given to this research. His words and awareness about this work made difference in rough times.

I wish to thank Dr. Ramana Chintalapalle for his guidance and advice, especially during the early stage of this work. His advice is highly appreciated and was key to conceptualize the experiments.

Gratitude is expressed to the W.M. Keck Center for 3D Innovation and its NSF Grant No.1405526 that partially funded the fabrication of the specimens.

Thanks to the Center for Transportation Infrastructure Systems and its staff for facilitating the system for the compression tests of solid metals.

Finally, I wish to thank my family and friends for their encouragement throughout my graduate studies.

Edel Arrieta

Abstract

Additive manufacturing permits the fabrication of cellular metals which are materials that can be highly customizable and possess multiple and extraordinary properties such as damage tolerance, metamorphic and auxetic behaviors, and high specific stiffness. This makes them the subject of interest for innovative applications. With interest in these materials for energy absorption applications, this work presents the development of nonlinear finite element models in commercial software platforms (MSC Patran/Nastran) that permit the analysis of the deformation mechanisms of these materials under compressive loads. In the development of these models, a detailed multiscale study on the different factors affecting the response of cellular metals was conducted with the objective to understanding the physics with the objective of selecting the most appropriate experiments. In that manner, a series of experiments were conducted on Ti-6Al-4V specimens fabricated by electron beam melting at different manufacturing orientations. Digital image correlation was presented as a vital tool for the measurement of strains in specimens with complex shapes; the experiments contemplated compression and tension tests of Ti-6Al-4V solid components, as well as compression tests on cellular lattices of the same alloy. FEMs were developed from the same CAD file utilized for the fabrication of the lattices; in addition, different meshing approaches and mesh convergence analysis were discussed. The mesh density showed convergence in models with over 70,000 elements, permitting the evaluation of the stress/strain-distribution mechanisms in the lattices. However, because of the considerable variability of the experimental material properties, some numerical results showed significant errors in predicting the compressive force applied to the lattices during the experiments; thus suggesting the need to improve the quality control in the manufacturing process and develop better technologies in computational mechanics for the modeling of cellular metals.

Table of Contents

Acknowledgements iv

Abstract vi

Table of Contents vii

List of Tables x

List of Figures xi

Chapter 1 : Introduction 1

1.1 Additive Manufacturing 2

1.2 Cellular Solids 5

1.3 Scope of Work 7

1.4 Outline 8

Chapter 2 : Overview of Cellular Solids Fabricated by EBM 10

2.2 Microscale 10

2.2.1 Manufacturing Technology 11

2.2.2 File Format 11

2.2.3 Constituent Solid 12

2.2.4 Manufacturing Parameters 14

2.2.5 Manufacturing Process 16

2.2.6 Degradation of the Mechanical Properties 16

2.3 Mesoscale 17

2.3.1 Stochasticity 17

2.3.2 Nested Hierarchical Levels 18

2.3.3 Aspect Ratio 19

2.3.4 Maxwell Stability Criterion 19

2.3.5 Auxetics 21

2.3.6 Relative Density 22

2.4 Macroscale 23

2.4.2 Lattice Orientation 24

2.4.3 Deformation Mode 26

2.4.4 Brittleness 26

2.4.5 Recovery 26
2.4.6 Unit-cell Specifics 27
2.4.7 Remarks on the Multiscale Analysis Approach 27

Chapter 3 : Material Properties Characterization 31
3.1 ASTM E9 Standard Compression Test of EBM Ti-6Al-4V 33
3.1.1 Specimens 34
3.1.2 Apparatus 34
3.1.3 Procedure 36
3.1.4 Results 37
3.2 ASTM E8 Standard Tension Test of EBM Ti-6Al-4V 38
3.2.1 Test Specimens 39
3.2.2 Apparatus 39
3.2.3 Procedure 40
3.2.4 Results 41
3.3 Tension Test of EBM Ti-6Al-4V Microstruts 48
3.3.1 Test Specimens 48
3.3.2 Apparatus 49
3.3.3 Procedure 49
3.3.4 Results 50
3.4 Compression Test of EBM Ti-6Al-4V Cellular Lattices 52
3.4.1 Specimens 52
3.4.2 Apparatus 53
3.4.3 Procedure 54
3.4.4 Results 55

Chapter 4 : Multiscale Analysis of Cellular Solids Fabricated by EBM 58
4.1 Microscale 58
4.1.1 Manufacturing Parameters 59
4.1.2 Manufacturing Process 60
4.1.3 Degradation of the Mechanical Properties 66
4.2 Mesoscale 68
4.2.1 Maxwell Stability Criterion 69
4.2.2 Auxetics 71

4.2.3 Relative Density 74
4.3 Macroscale 75
4.3.1 Deformation Mode 75
4.3.2 Brittleness 77
4.3.3 Recovery 77
4.3.4 Unit-cell Specifics 79
Chapter 5 : FEM of EBM Ti-6Al-4V cellular lattices 84
5.1 Finite Element Model 84
5.2 Finite Element Analysis 88
5.3 Convergence Analysis 88
5.4 Results 90
Chapter 6 : Conclusions 99
6.1 Remarks 99
6.2 Conclusions. 99
6.3 Recommendations and Future Work. 101
Chapter 7 : References 103
Vita 108

List of Tables

Table 2.1 Summary of the determinants of design followed in a multiscale analysis. 29

Table 3.1 Strength of microstruts 52

Table 3.2 Compressive properties of lattices. The mass of monolithic plates is excluded. 57

Table 5.1 Summary of FEMs at different mesh density and material properties. 98

List of Figures

Figure 1.1 EBM Ti-6Al-4V 3D shapes fabricated at W. M. Keck Center for 3D Innovation..... 3

Figure 1.2 (a)EBM systems at UTEP Keck Center for 3D Innovation. From ("W.M. Keck Center for 3D Innovation," n.d.). (b) EBM system schematic: (1) Electron gun assembly; (2) EB focusing lens; (3) EB deflection coils (x-y); (4) Powder cassettes; (5) Powder layer rake; (6) solid build ; (7) Build table. From (L. E. Murr et al. 2009). 4

Figure 1.3 EBM Ti-6Al-4V (a) metal foam and (b) lattice. 6

Figure 1.4 EBM Ti-6Al-4V specimens for testing. 9

Figure 2.1 Scale levels for the analysis of cellular solids 10

Figure 2.2 The rigid Atomic Body-Centered Cubic (BCC) atomic structure (Left) can constitute brittle materials (similar to β-phase Ti). Although efficiently packed, Hexagonal Close Packed (HCP) Atomic structure (Right) is softer, thus tending to constitute more ductile materials (e.g. α-phase Ti) 13

Figure 2.3 Prealloyed ARCAM Ti1-6Al-4V with some sintered particles; 1mm scale mark (left). A flaw in a 30° standard tension specimen; unmelted material and rounded shapes of partially melted particles are observed; arrow indicating build direction; 50µm scale mark (right). 14

Figure 2.4 Void at one of the internal nodes in a reentrant hexagonal lattice (left). Profile of an internal microstrut in a hexagonal lattice (right). 1mm scale marks and arrow indicating build direction. 15

Figure 2.5 Profile and top view (left and right) of a 90°, 0.8mm x 0.8mm square microstrut. 1mm scale mark and arrow indicating build direction. 15

Figure 2.6 EBM fabricated Ti-6Al-4V cellular solids: foam (Left) and lattice (Right). 18

Figure 2.7 Example of axially-dominated and bending-dominated unit-cells, where axially-dominated unit-cells are characterized by triangles only. 21

Figure 2.8 Representations of different compressive responses of cellular solids, highlighting behavior originated by specific features. a) Ideal 3-stages Response of ductile, bending-dominated lattices ($M<0$); b) 3-stage response of brittle, axially-dominated lattices ($M\geq0$); c) expected response of lattices fabricated with brittle constituents; d) Expected cyclic response of auxetic, self-bracing unit-cells. 24

Figure 2.9 Node and microstruts in a lattice (left). 60° microstrut in a hexagonal lattice, highlighting step-like features measuring 480µm long by 250µm tall, approximately (right). 1mm scale marks. 25

Figure 2.10 Schematic responses of orthogonally symmetric cellular solids to the loading direction. 25

Figure 3.1 Schematic of components fabricated at different build angles. XZ defines the powder bed plane and Y indicates the direction of the beam; arrowheads indicate the building direction (vertical, parallel to the beam) while hatch represents the layering pattern. 33

Figure 3.2 30° specimen (a) with support (b), as-fabricated from ARCAM A2 system. 34

Figure 3.3 70MN Instron 5594 UTM and compression platens with spherical seat. 35

Figure 3.4 a) rapid prototype bearing base for compression test, b) cross sectional stresses in the assembly, c) isosurface at 80% maximum stress recommended for the steel platens, d) isosurface at 80% the EBM Ti-6Al-4V yield stress. 36

Figure 3.5 Specimen setup. 37

Figure 3.6 Compression stress-strain curve for EBM Ti-6Al-4V. Last two digits on the right in series name indicate built angle. 38

Figure 3.7 Permanent deformation of 0°, 30°, 60°, 90° specimens (left to right) 38

Figure 3.9 DIC workstation (1); UTM workstation (2); cameras (3); LED spotlights (4); UTM control module at the frame; clip extensometer installed in specimen (6). 40

Figure 3.10 Specimen setup for dual strain-measurement tests. 41

Figure 3.11 Strain measured by: virtual (thin line) and clip (thick line) extensometers. 42

Figure 3.12 Tensile stress-strain of specimens at different orientations. 0° (a) to 90° (d). 43

Figure 3.13 Tensile stress-strain curve of specimens at different build direction. 44

Figure 3.14 Optical microscopy of regions near failure of 30° (left) and 90° (right) specimens. 1mm scale mark. 44

Figure 3.15 Micrographs of 90° specimen (left) and 30° Ti-6AL-4V microstructure. 45

Figure 3.16 DIC strain fields comparison on specimens with different build angles. 46

Figure 3.17 Failure profiles of 0°, 30°, 60°, 90° (a, b, c, d) specimens. 1mm scale marks. 47

Figure 3.18 Comparison of a 90° internal microstrut in a hexagonal lattice (Left) and a 90° microstrut specimen (right). 1mm scale marks. 48

Figure 3.19 ADMET expert 5603 (1); ADMET control (2); cameras (3); 49

LED spotlights (4); wedge grips (5). 49

Figure 3.20 45° microstrut and DIC setup (left) and after failure (right) 50

Figure 3.21 DIC linear stress-strain curves of 0°, 30°, 45°, 60° and 90° microstruts (top to bottom). 51

Figure 3.22 Hexagonal (left) and reentrant hexagonal (right) lattices with 7mm, 6mm and 5mm unit-cell size (back to front). Three of each specimens shown were fabricated and tested. 53

Figure 3.23 MTS Landmark 370 (1); MTS control (2); cameras (3); LED spotlights (4). 54

Figure 3.24 Setup of specimen (5mm HEX, left) and virtual extensometers (6mm REHEX, right). 55

Figure 3.25 Stress-strain curves of hexagonal (top) and reentrant hexagonal lattices with different unit-cell size. 56

Figure 4.1 Scale levels for the analysis of cellular solids 58

Figure 4.2 Bi-modal microstructure uniformly distributed acicular, α-phase (HCP) surrounded by β-phase (BCC) (dark) in Ti-6Al-4V cylindrical rods at 90° (left). Fracture surface at perspective displaying ductile features such a prominent crest and dimples; 50µm scale mark (right) 60

Figure 4.3 Strength variability between batches of microstruts with different orientations. 61

Figure 4.4 From left to right: 0°, 30°, 45°, 60° and 90° microstruts top and lateral-right views displaying layering striations with partially melted particles. 62

Figure 4.5 Failure profiles of 0°, 30°, 60°, 90° (a, b, c, d respectively) standard tension specimens displaying necking and shear lips for 0° and 90°. 1mm scale marks. 63

Figure 4.6 Flaw in a 60° standard tension test specimen. 100µm scale mark. 63

Figure 4.7 Stress-strain of 60° tensile specimens. 60deg99 representing the specimen with an interrupted building. 64

Figure 4.8 Fractography with mixed ductile and brittle features in a tensile specimen with the interrupted building process; 500µm scale grid (left). Failed specimen (right) 65

Figure 4.9 Setup and failed specimens under compression and tension (a, b and c, d). 65

Figure 4.10 Average and standard deviation of tensile and compressive yield strengths on specimens at different orientations. 66

Figure 4.12 The elastic modulus of 60° Ti-6Al-4V calculated for 0.8mm x 0.8mm microstruts is over 25% lower than that for the standard tension test specimens (116Gpa approx). 67

Figure 4.13 Stress-strain curve of 0°, 30°, 45°, 60° and 90° microstruts. Microstruts fabricated at lower build angles showed to be stiffer and stronger. All orientations observed a practically linear response. 68

Figure 4.14 Representation of 30° (a) and 60° (b) microstruts. Conceptually, with a layer thickness of 0.3mm, the effective cross-section widths are 0.54mm and 0.65mm for the 30° and 60° microstruts when loaded axially. 68

Figure 4.15 Examples of mechanistic unit-cells (M<0). 69

Figure 4.16 Cut-section of the lattice model highlighting the measured unit-cell and the bearing points where the load is transferred between unit-cells levels (Top). DIC images of 5mm hexagonal lattice: an instant before fracture (a) and after fracture (b). The double arrow at (a) indicates the location of the virtual extensometer. 70

Figure 4.17 Nonlinear stress-strain curve of a single 5mm hexagonal unit-cell during the compression test on the lattice. 71

Figure 4.18 5mm reentrant hexagonal unit-cell (left) and FEM of a single unit-cell displaying negative Poisson's effect. 1mm scale mark. 72

Figure 4.19 DIC images of a 5mm reentrant hexagonal lattice: an instant before fracture (a) and after fracture (b). The double arrows at (a) indicate the location of the axial and transverse virtual extensometers (Top). Measured Poisson's ration at the unit-cell indicated by the extensometers. 73

Figure 4.20 Poisson's ratio of a reentrant hexagonal lattice (7mm) during compression. 74

Figure 4.21 Ultimate compressive strength and specific density (top) of the EBM cellular Ti-6Al-4Vspecimens (bottom). 75

Figure 4.22 Compressive responses of hexagonal lattices with different unit-cell sizes. 76

Figure 4.23 Stress fluctuations in a nonlinear segment of the response of a 5mm hexagonal lattice. 77

Figure 4.24 Progressive collapse of unit-cell levels in lattices displaying recovery and accumulated damage. Reentrant hexagonal lattices (left) and hexagonal lattices (right) at different unit-cell size. 78

Figure 4.25 Compressive response of reentrant hexagonal lattices with different unit-cell sizes. 79

Figure 4.26 Stress-strain curves of hexagonal and reentrant hexagonal lattices at different unit-cell size. 80

Figure 4.27 Comparison of lattices at different loading stages: unloaded (a, 1), an instant before failure (b, 2), the instant at failure (c, 3) and after failure (d, 4). The energy releasing events of the two unit-cell configurations totally opposite (c, 3). Images from video recordings at 29 frames/s. 81

Figure 4.28 Deformation of a reentrant hexagonal unit-cell: jaw-like (a); schematic of the expected unit-cell transformation (b); rendering of the new unit-cell after transformation (c); rendering of the top view of a deformed reentrant hexagonal unit-cell reconfigured into four new triangular unit-cells (d) 83

Figure 5.1 Stress-strain data plots. For clarity, only 30° and 90° standard tension are shown.... 86

Figure 5.2 FEM of the hexagonal, 6mm lattice loaded with 1mm element-uniform displacement. MPC and resultant force vector at the bottom. 88

Figure 5.3 Mesh convergence curves for hexagonal (left) and reentrant hexagonal (right) models. 5mm, 6mm and 7mm unit-cell sizes (top to bottom); two material properties per graph are shown. Solid line representing the experimental average ultimate load. 90

Figure 5.4 von Mises stress distribution (MPa) in hexagonal (left) and reentrant hexagonal (right) 5mm lattices. Darker colors indicate lower stress. 92

Figure 5.5 Stress "Y" component in MPa; purely compressive stress state in 7mm hexagonal lattices (left). Tension (-) and compression (+) stresses in 7mm reentrant lattices (left). 92

Figure 5.6 Inclined microstruts, in light color, indicating higher von Mises stress (MPa). 93

Figure 5.7 Stressed microstruts and low-stress columns in reentrant hexagonal lattices. Columns in hexagonal lattices dispersing compressive stresses from microstruts (left). 93

Figure 5.8 Dimetric of 6mm lattices displaying von Mises stress distribution (MPa). 94

Figure 5.9 Shear stress distribution in 7mm lattices (MPa). 94

Figure 5.10 von Mises plastic strain hexagonal (top) and reentrant hexagonal (bottom) lattices with 5mm (left) and 7mm (right) unit-cells. 96

Figure 5.11 Plastic strain in interior microstruts. 96

Figure 5.12 Undeformed model wireframe in highlighted light color on the left side face of the lattice, highlighting the auxetic behavior. 97

Chapter 1: Introduction

Cellular metals display tremendously varied properties; they can possess high specific strength or crush and absorb energy, they can be good conductors for heat exchange or act as insulators; they can interact with biological tissues in the form of implants that integrate with bone, or they can also survive in aggressive chemical environments as high surface area electrodes, if fabricated from an appropriate precursor. The common circumstance to these examples is that now, thanks to additive manufacturing (AM), this wide range of material properties can be highly manageable by design, besides allowing combination of properties, thus developing so-called metamaterials.

Given the ability to sustain large deformations at lower stresses, compared to conventional solids, cellular materials are often presented as ideal for the energy absorption of impacts. The literature on the mechanical properties of these materials can be found from the microstructure of the precursors, to the failure mode of different cell geometries, but the scope is often limited to particular interests of authors. For example, research is found discussing metallurgical features, but overlooking the structural stability of the unit-cell (Zhao et al. 2016); others specifically refer to characteristics from additive manufacturing (A. Cheng et al. 2014), while other investigators discuss the deformation mechanisms of the unit-cells and omit the contributions of microstructural features in their performance (Vigliotti and Pasini 2013). Although the current research work substantially contributes, from different scopes, to the understanding of these materials, the cellular lattices could be further analyzed in a multiscale approach, by delving into different scale levels to reveal different features, and how they interact to define the mechanical properties of cellular solids. The freedom of design in metals, provided by powder bed fusion technologies allows exerting certain control over features as small as microstructures, as well as over defining unit-cell geometries resulting in cellular solids with mechanical properties as product of combined effects from the different features at different scales. Numerous factors are identified in this work, and diverse their possible combinations that can result in tougher cellular metals with enhanced

deformation capabilities ideal for energy absorption applications, but these combinations can also producer stiffer and lighter lattices better suited for structural applications. Thus, a comprehensive understanding of all these factors, their interactions, and effects in the response of cellular metals is vital in developing custom designs with tailored responses.

As more applications are developed to use these materials as energy absorbers, structurally efficient members, or a combination of applications, experimental testing of these materials has become a significant component of their development and study. Experimental testing demands valuable resources; numerical simulations ease the bridging from materials science into engineering applications and increase the chances of early experimental success. The development of computer models of cellular materials grants us the availability to modify features on their design and explore their response; all in the same CAD model from which the components will be fabricated by AM.

Following, a brief discussion about additive manufacturing and cellular solids is presented. Chapter 2 reviews different factors affecting the response of cellular metals. Chapter 3 presents a series of experiments on EBM Ti-6Al-4V components, addressing its features and mechanical properties. Chapter 4 performs comprehensive design cases of lattices with two different unit-cell shapes. In Chapter 5, finite element modeling of the compressive response of the lattices is presented. Chapter 6 finalizes the study with discussion and remarks.

1.1 Additive Manufacturing

Often referred to as 3D printing, the powder bed fusion process starts from 3D Computer-Aided Designs (CAD) that are sent and discretized into slices in the fabrication system unit where the component is formed by adding, or *printing*, successive layers of powder metal melted one over the previous. Compared to more conventional processes, AM of metals can immediately produce ready-to-use components with minimum waste, and given that no molds are required, there is zero mold-reactivity effects unlike casting (Li et al. 2012). Advantages of EBM include

higher freedom of design that results in unique geometries that are not possible with subtracting processes such as milling. However limitations in size, powder removal, "step-like" errors in the construction direction, surface finishing and material availability are still challenges being addressed (L. E. Murr et al. 2010). Direct Metal Laser Sintering (DMLS) or Selective Laser Melting (SLM) and Electron Beam Melting (EBM) are two innovative AM technologies that have shown promising results in building complex, innovative geometries (Figure 1.1) from metal alloy precursors such as Copper, Aluminum, stainless steel, Cobalt, Nickel and Titanium (Lawrence E. Murr et al. 2012).

Figure 1.1 EBM Ti-6Al-4V 3D shapes fabricated at W. M. Keck Center for 3D Innovation.

Because of their similarity and superior advantages over traditional manufacturing processes, SLM and EBM, rather than competitors should be seen as allies in the evolution of AM technologies. Being the source of energy the main difference between these technologies, their discrepancy in the mechanical properties are mainly related to the cooling and solidification rates of the melt pool that result in different microstructures. Whereas SLM has been found to produce builds with slightly higher yield and ultimate tensile strengths on Titanium alloys, EBM builds of the same material have shown less residual stresses and elongations (L. E. Murr et al. 2009) indicating higher ductility, thus a more suitable material for energy absorption applications.

Developed by Swedish Arcam AB, EBM manufacturing systems have been commercially available for more than a decade ("Arcam History" 2014). This process takes place in a vacuum chamber at high temperatures (~0.4 - 0.6 melting temperature) where components are built layer by layer from metal powder, melted by an electron beam. Metal is raked in beds from powder fed hoppers and melted in layers as thin as 10μm (0.1mm), each defined from a "sliced" 3D CAD model directing the beam; after the layer has melted, the building table lowers, and a new layer starts from raking the powder (Figure 1.2). Finally, the finished components are taken into a recovery unit where the unmelted powder is blown by an air gun for later reclamation (Lawrence E. Murr et al. 2012).

(a)  (b) 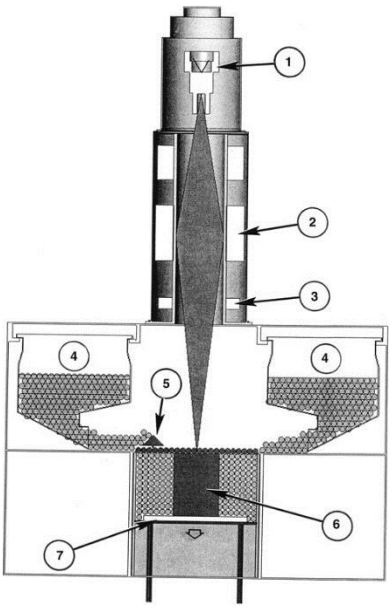

Figure 1.2 (a)EBM systems at UTEP Keck Center for 3D Innovation. From ("W.M. Keck Center for 3D Innovation," n.d.). (b) EBM system schematic: (1) Electron gun assembly; (2) EB focusing lens; (3) EB deflection coils (x-y); (4) Powder cassettes; (5) Powder layer rake; (6) solid build ; (7) Build table. From (L. E. Murr et al. 2009).

As discussed earlier, SLM normally produce more structural efficient components when compared to EBM, however the latter is more suitable for energy absorption structures and has been selected for this study. Moreover, the limited available literature on EBM suggests the lack of research on the matter presumably due the considerably fewer EBM systems compared to SLM

on service around the globe nowadays ("Multi-Year Overview | Ir.arcam.se" 2014, "EOS Global Presence" 2014).

Furthermore of the potential of lattices in enhancing energy absorption mechanisms (Zhu et al. 2010), we shall highlight the in-situ production on demand among the advantages that indeed are positioning AM technologies, such as EBM, at the technological forefront. In-situ production on demand refers to the possibility to have AM systems for the fabrication of components where required, when required. Currently partnered with NASA (Made in Space 2013a), the American Made in Space, from Moffett Field, CA has successfully installed the first 3D printer in the space at the International Space Station for the manufacturing of components for NASA. Asserting the importance of this event, Made in Space CEO Aaron Kemmer expressed: "Imagine an astronaut needing to make a life-or-death repair on the International Space Station… rather than hoping that the necessary parts and tools are on the station already, what if the parts could be 3D printed when they needed them?" (Made in Space 2013b). Finally, but not less important, the transportation of AM precursors possess the advantage of fluid-like materials acquiring any shape of the available cargo space, compared to components already manufactured with voids and creating dead-spaces when stacked.

1.2 Cellular Solids

Unlike the liquid state processes, additive manufacturing by powder bed fusion provides incredibly design freedom where the once novel metallic foams can now be precisely designed and fabricated as lattices, thus upgrading their already plausible features such as specific stiffness and toughness. As per the architecture of its network we differentiate these materials as foams and lattices (Figure 1.3). Often referred as sponges, foams present stochastic networks, meaning they possess poorly patterned geometries often resembling organic shapes. Lattices, or mesh arrays, are defined by non-stochastic networks with well-defined geometries typically characterized by a network of straight segments often called struts, or microstruts, and whose symmetry resembles a

truss. Depending on the boundaries of the cells in the network, foams and lattices can be additionally defined as open-cell or closed-cell where the thickness and slenderness of the struts and walls respectively play an important role in their mechanical properties (Tan, Reid, and Harrigan 2012).

(a)  (b) 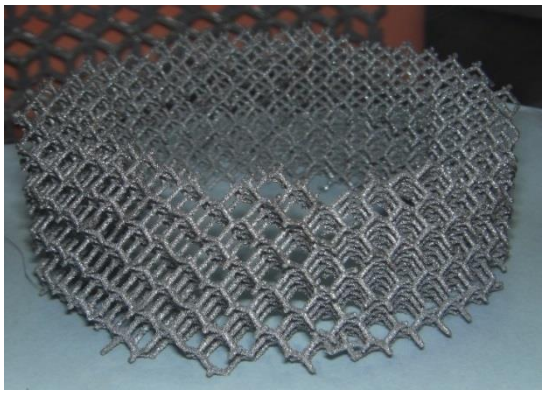

Figure 1.3 EBM Ti-6Al-4V (a) metal foam and (b) lattice.

Lattice structures typically are more damage tolerant, displaying more uniform mechanical properties in comparison to stochastic foams (Queheillalt and Wadley 2005). Numerical models suggest that latticed materials are more tolerant to defects compared to foams. By randomly removing struts, the modulus and compressive strength of open-cell foams decreased more rapidly than for lattices. Although varied results are reported, investigations coincide in the proportionality of the elastic modulus to density of open-cell materials (Kwon, Cooke, and Park 2003); thus in regards to damage sensitivity, the removal of struts reduces the modulus in a faster manner than the thinning of these (Wallach and Gibson 2001). Well-designed sandwich plates with cellular lattices in the core showed to withstand larger blast impulses than solid plates of the same material and weight(Zhu et al. 2010). Other investigations with sandwich panels revealed the post-yield response under dynamic loads to be insensitive to the low velocity range of impact; furthermore, a more localized deformation was observed for high velocities. In underwater explosion tests, lattices were found to crush in a progressive manner by a subsequent buckling of struts layers, providing insights as to the effects of filling materials in enhancing plastic deformation of the metal

(Tan, Reid, and Harrigan 2012). Thus, for the particular interest of energy absorption applications exposed herein, lattices are selected as better alternatives than foams. Additionally, these non-stochastic architectures have been reported to behave within the characteristic parameters for cellular solids defined in Ashby, M. F. et al. (2000), such as slenderness, aspect ratio, relative density and modulus among others (Ushijima et al. 2011).

Expressed as the rate of the externally applied energy divided by the amount of mass of the material withstanding it, the normalized absorbed energy is the common parameter to evaluate the capability of materials to dissipate energy. Empirical evidence reports that the bending of struts, the formation and manipulation of multiple shear bands, and microcracking of the constituent material among many other features, also contribute to the absorption of energy (Zhu et al. 2010).

Properties of cellular solids can be summarized to be driven by mostly three aspects: (a) the properties of the solid precursor, (b) the topology of the unit-cells, and (c) the relative density, which is expressed as the ratio of the density of the cellular material divided by its density as a solid (Ashby, M. F. et al. 2000).

1.3 Scope of Work

The multiple outstanding properties of these, fairly called, metamaterials derive from a complex multiscale interaction of several manipulable features extending from material phases to the cellular solid itself. There is no doubt that there is a significant interest in exploiting the capabilities of lattices for multiple applications. For this reason, it is important to develop numerical models that can emulate their deformation mechanisms and predict their mechanical properties while accelerating the design and understanding of these materials and their behavior.

The extraordinary, often multifunctional, properties of cellular solids make them subject of great attention from a variety of disciplines such as electromagnetics, mechanical and acoustical. The major attention is probably driven by the high customization inherent to additive manufacturing. However, the number of variables involved in the designing of these materials is

immense, and probably, some are still unknown and threaten the integrity of the intended design by neglecting some side effects of modifying design variables.

In the development of FEMs, a knowledge-based approach provides fundamental notion of the expected performance of simulations, and its correct interpretation; it also provides background and support for identifying limitations of the numerical processes representing physics. Thus, the comprehensive multiscale analysis presented in this research leads to a structured way of thinking when designing cellular metals. The better understanding of all the design variables eases the identification of those that can contribute the most toward the desired performance of the material, and also helps in evaluating any side effects during the design process. This investigation is not only describing and identifying each of the factors and their complex interrelationships participating in the response of cellular metals, but it is also evidencing and supporting them with a variety of experiments, including two different design-modeling cases; one based on 3D hexagonal unit-cells, and another based on 3D reentrant hexagonal unit-cells performing with a negative Poisson's ratio. In this context, a rapid methodology for the modeling and prototyping of Ti-6Al-4V cellular lattice solids in commercial platforms is presented as follows: CAD from Dassault Systèmes Solidworks, manufacturing from an ARCAM A2 system, and modeling and simulation from MSC Patran/Nastran 2014.1.

1.4 Outline

In Chapter 1, a brief introduction to additive manufacturing and cellular solids is presented. Chapter 2 overviews different factors found affecting the response of cellular metals fabricated by powder bed fusion, and proposes a multiscale analysis that identifies and classifies these variables according to size. Chapter 3 features four different series of experiments on Ti-6Al-4V specimens (Figure 1.4); ASTM E8 standard tension, ASTM E9 standard compression, uniaxial tension test of microstruts and uniaxial compression test of cellular lattices. Variables such as manufacturing orientation and size effect, mainly, are experimentally evidenced influencing the mechanical

properties of the metal. More important is the data gathering from testing, data that serves as input for the properties of the finite element models and also as benchmark for the simulations. Chapter 4 delivers a comprehensive multiscale analysis of two different lattice designs: 3D hexagonal and 3D reentrant hexagonal. The analysis in this chapter addresses the multiple considerations in designing these cellular metals. The influence of each factor influencing the response of the cellular metal is also discussed and supported by the findings from experiments, digital Image correlation, failure analysis and metallography. Chapter 5 presents the finite element modeling of lattice specimens and a comparison to experimental results. Finally, Chapter 6 includes discussion, remarks and future work for this investigation.

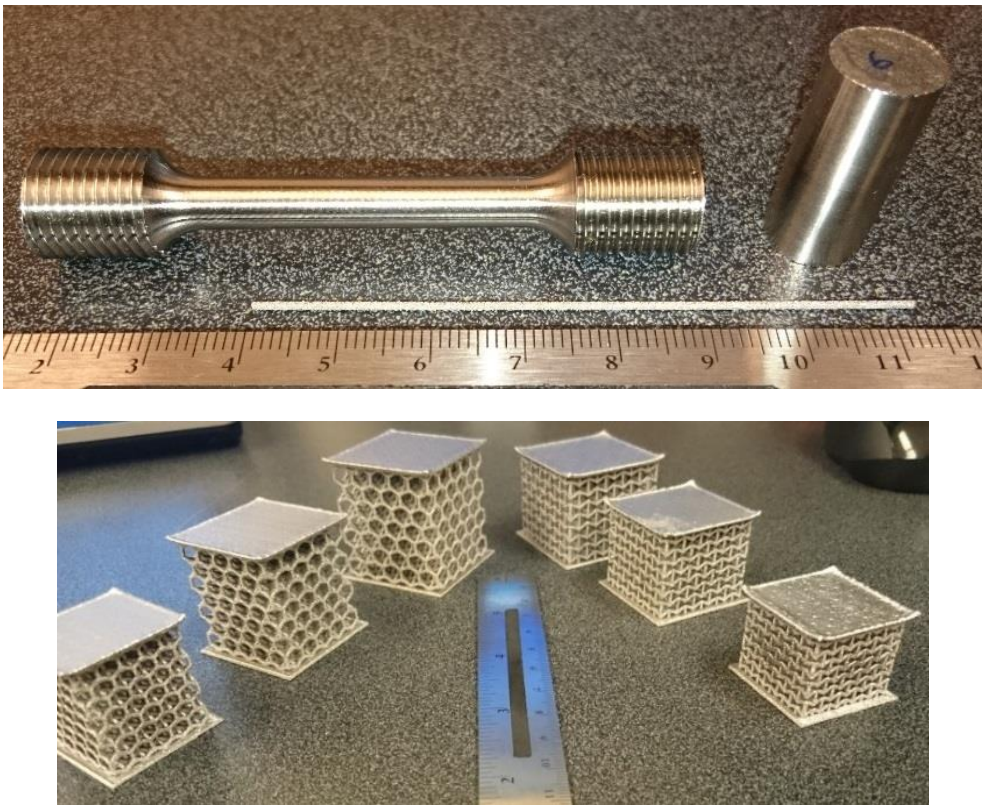

Figure 1.4 EBM Ti-6Al-4V specimens for testing.

Chapter 2: Overview of Cellular Solids Fabricated by EBM

The response of cellular metals can be affected by multiple factors. In general, the manufacturing technology, the constituent solid, and the geometrical features, among others, give the cellular metals a variety of characteristics that combined result in very unique responses. The diversity of features can be introduced in different manners and their effects may be complex and interdependent. Thus, when designing these materials it is important to identify important desired features to determine if they can be introduced through the manufacturing process. This chapter presents a brief discussion of these features starting at the microscale and moving all the way to macroscale (Figure 2.1).

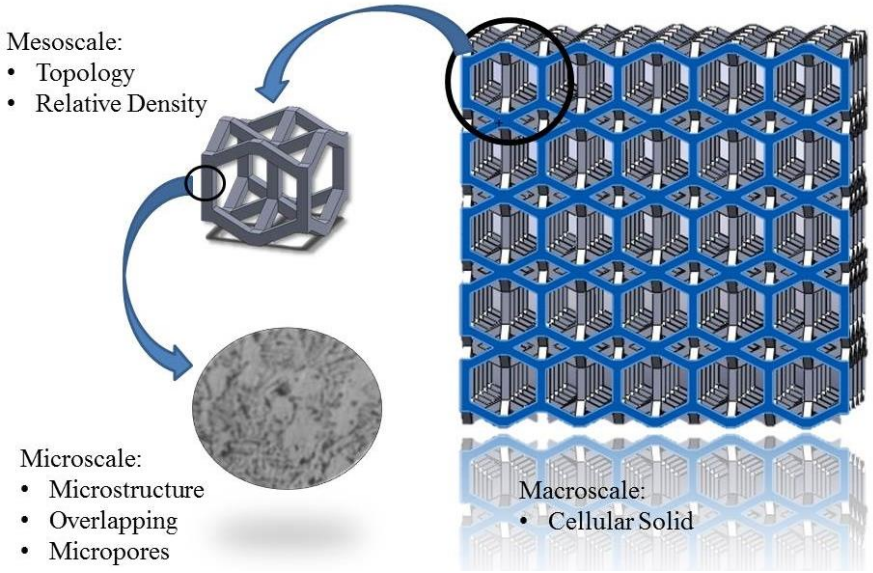

Figure 2.1 Scale levels for the analysis of cellular solids

2.2 Microscale

At this scale, the material designer has the most limited control and flexibility because of size restrictions. The design features at this scale extend from surface roughness up to atomic structures, however, the limited control and flexibility at this level result in cellular solids material

properties that possess a certain level of randomness. The factors that control these microscale features include manufacturing technology, file format, constituent solid, manufacturing parameters, manufacturing process, and mechanical properties degradation.

2.2.1 Manufacturing Technology

EBM and SLM may be considered two of the most convenient AM techniques for the structured fabrication of cellular metals. The higher beam energy in the EBM compared to SLM process normally produces builds with lower residual stress and coarser surfaces producing stress concentrators that become critical as the cross-section area of the microstruts decreases (Cheng et al., 2012; Hernández-Nava et al., 2016; Murr et al., 2009). Normally, Ti-6Al-4V components fabricated by EBM display larger amounts of the more ductile α-phase (Hexagonal Close Packed) microstructure than those by SLM, displaying α'-phase microstructure (Murr et al., 2009). Additionally, the atmosphere in the manufacturing chamber, and the availability and characteristics of the precursor powders from each manufacturer, such as the particle size distribution and chemical composition influence the efficiency of the beam, the purity and the physical and chemical characteristics of the solidified builds (Wang et al., 2014). In general, the selection of precursor powder and technology is based on availability.

2.2.2 File Format

The stereolithography (.STL) file format is currently the most common file for additive manufacturing systems. This format describes volumetric objects by representing only their surfaces, which in turn are discretized into planar triangles exclusively. The layering discretization approach from the AM technologies combined with the geometric representation of planar triangles, that also neglects color and texture, can reduce the flexibility of design, and potentially introduce flaws and defects in the components. In this context, if significant inaccuracies compromising the component are produced, these can be addressed by overdesigning, until a more

precise format such as the Additive Manufacturing File (AMF) is fully developed and becomes a new standard. (Paul and Anand 2015).

2.2.3 Constituent Solid

Properties from the constituent solid directly contribute to the performance of lattices and foams; hence the mechanical, thermal, electrical, and other properties from the constituent are directly transferred to the cellular solid. Therefore, it is most likely that a brittle constituent will produce unit-cells that also fail brittle, and similarly for ductile constituents.

Thus, the mechanical response of the cellular metals could be tailored by combining the deformation mechanisms of the unit-cells with microstructural features, at the mesoscale and microscale respectively (L. E. Murr et al. 2009; Biamino et al. 2011). In that context, the capability to deform as a mechanism (van der Giessen 2011; Maxwell 1864) of the 3D hexagonal honeycomb unit-cell could be enhanced if fabricated utilizing solids with microstructures rich in ductile material phase, such is the case of α-phase titanium. Otherwise, the deformation capability of the unit-cell can be reduced if fabricated with constituent solids with predominantly rigid crystalline structures such as β-phase titanium, to exemplify our material selection (Figure 2.2).

For metals, a crystal unit cell is the smallest structural unit and characterizes the properties of that material; crystalline structures are repetitive, and oriented in a manner that can influence the mechanical properties of solids (Wielewski et al. 2015; Semiatin et al. 2013), that can be seen as additional hierarchical levels in cellular metals. Thus, it is important in designing cellular lattices, to consider these fundamentals and be cautious of the cooling rates since some direct energy deposition fabrication methods are capable of producing allotropes by delivering localized amounts of energy, and potentially promote more ductile/brittle material phases as required.

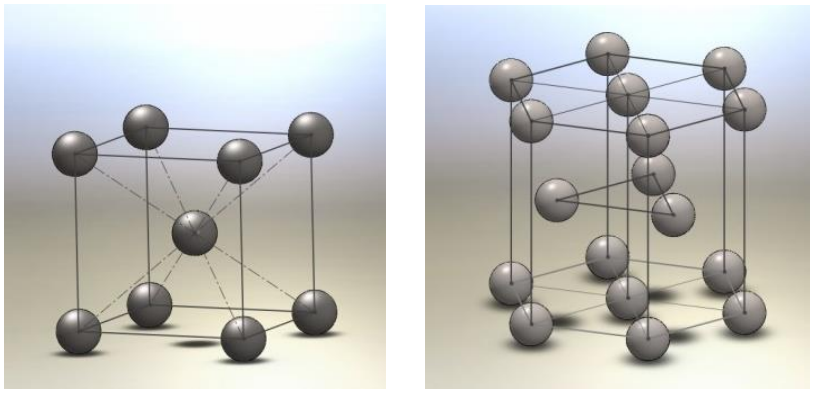

Figure 2.2 The rigid Atomic Body-Centered Cubic (BCC) atomic structure (Left) can constitute brittle materials (similar to β-phase Ti). Although efficiently packed, Hexagonal Close Packed (HCP) Atomic structure (Right) is softer, thus tending to constitute more ductile materials (e.g. α-phase Ti)

The spatial concepts of allotropy are also extended in understanding the development of alloys, where a different element is introduced in the base crystalline structure to reconfigure it and alter its physical properties. For the powder bed fusion, the availability of prealloyed powders should be considered, as well as its particle-size distribution. It is also important to consider the number of life cycles of the reclaimed powder given that, from the previous cycles, some particles could have been fused to each other, besides suffering alterations in their microstructure, originating abnormal shapes that can result in flaws and defects (Figure 2.3). Thus, in reducing the variability of the physical properties due to the powder precursor, the quality and size distribution of the particles shall be maintained as uniform as possible. Additionally, it has been observed that the coarseness of the surface is close to the order of the size of the smallest particles. (Hernández-Nava et al. 2016).

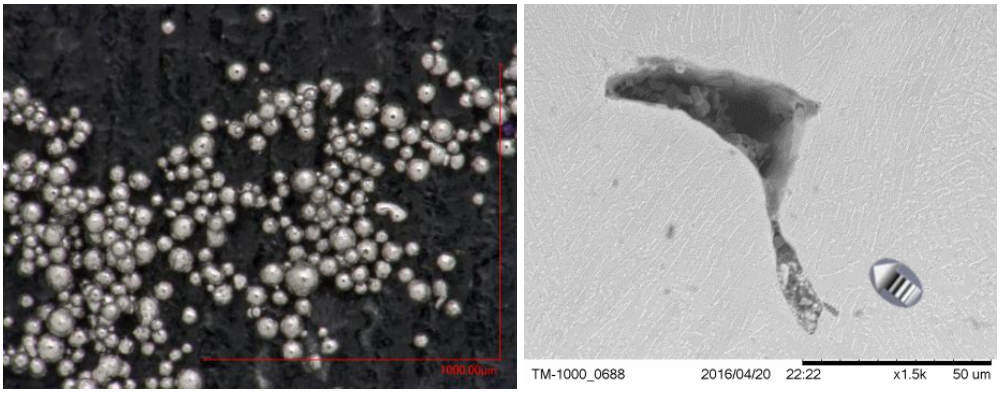

Figure 2.3 Prealloyed ARCAM Ti1-6Al-4V with some sintered particles; 1mm scale mark (left). A flaw in a 30° standard tension specimen; unmelted material and rounded shapes of partially melted particles are observed; arrow indicating build direction; 50µm scale mark (right).

2.2.4 Manufacturing Parameters

Some of the main differences between SLM and EBM are the type and the intensity of the beam energy, as well as the manufacturing atmosphere, however, most of the features produced by the manufacturing parameters of both technologies are comparable. It is of special attention that SLM and EBM are capable of producing a variety of material phases by controlling manufacturing settings (Lawrence E. Murr et al. 2012).

Manufacturing parameters such as the layer thickness and beam power have a direct effect on the surface roughness and the density of the material that significantly can compromise the integrity of components with small cross sectional areas, such as the microstruts used in this study; thin layers and high beam power will tend to produce nearly fully dense material, minimizing the presence of unmelted, sintered powder, and pores that might act as critical stress concentrators (Figure 2.4) (Gong et al. 2013). Similarly, longer exposure times will produce larger and more uniform melting pools, resulting in denser solids. Thus, occurrence of internal flaws, the uniformity of the surfaces, and properties of the builds are directly affected by the manufacturing time and energy spent during fabrication (Tsopanos et al. 2010). For example, the microstrut specimens used in this study were fabricated with nominal dimensions of 0.8mm x 0.8mm x

70mm; however, their cross-section was barely noticeable as squared and clearly not constant along the microstrut longitudinal axis (Figure 2.5).

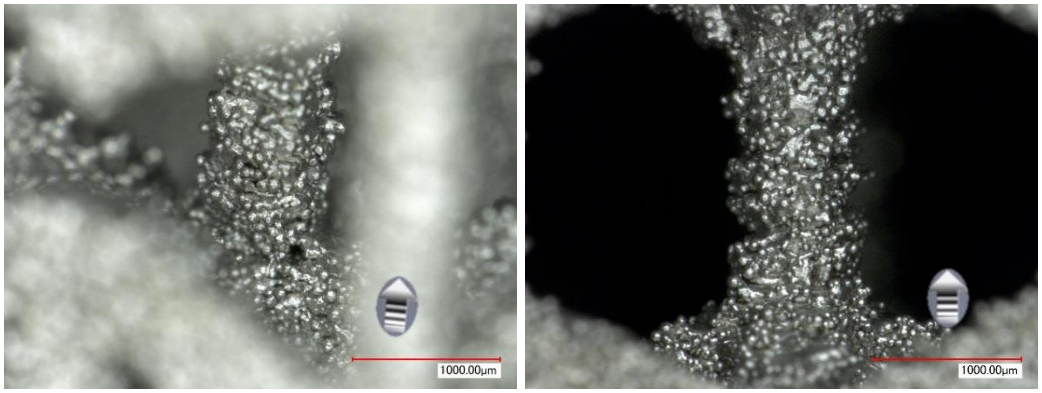

Figure 2.4 Void at one of the internal nodes in a reentrant hexagonal lattice (left). Profile of an internal microstrut in a hexagonal lattice (right). 1mm scale marks and arrow indicating build direction.

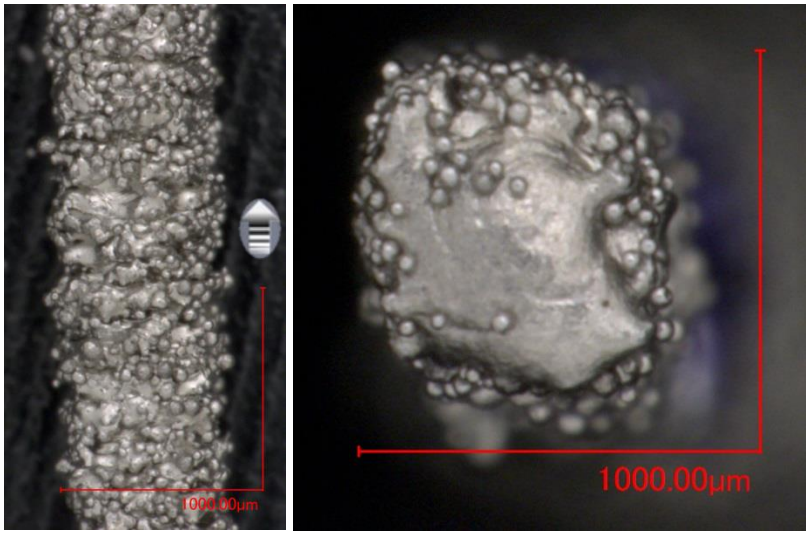

Figure 2.5 Profile and top view (left and right) of a 90°, 0.8mm x 0.8mm square microstrut. 1mm scale mark and arrow indicating build direction.

2.2.5 Manufacturing Process

While the Manufacturing parameters refer to all those settings that can be controlled from the manufacturing system, the Manufacturing process contemplates all those aspects mainly from preferred practices of the manufacturers; for example, the location and orientation of a component, may be defined from the optimization of the available space in the manufacturing chamber, and are not related to the system settings such as beam power and time of exposure. Cooling and solidification rates depend on multiple factors; they are affected by the manufacturing parameters, the manufacturing layout of components being fabricated, and the geometry of the component itself, including any support required for its fabrication. These rates have been found to alter the microstructure, phases and grain sizes in Titanium alloys. (Cansizoglu et al. 2008; L. E. Murr et al. 2010)

In general, heat loss tends to be more uniform and slower in large volume solids, and objects with smaller area to volume ratios, consequently, the cooling and solidification rates are also dependent on the geometry of the parts. Therefore, by carefully managing the manufacturing settings, it is possible to induce the formation of different, beneficial, microstructural features throughout the components at specific regions that, probably because its geometry, may develop spots whose cooling rates do not favor the formation of the desired microstructural features. For example, promoting the formation of ductile material phases around the nodes of mechanistic ($M<0$; refer *Maxwell Stability Criterion*) unit-cells can enhance their ability to develop plastic hinges, thus improving the toughness of the lattice.

2.2.6 Degradation of the Mechanical Properties

Powder bed fusion systems enabled the fabrication of very detailed and complex components when compared to conventional subtractive methods. However, this new manufacturing approach implies step-like surface features that can produce geometrical inconsistencies or inaccuracies, sometimes impractical or difficult to measure with an acceptable

level of certainty. This leads to the degradation of mechanical properties, dependent on the build angle and layer thickness. Regardless of the flaws and defects addressed in the manufacturing process, the deterioration of the mechanical properties shall be considered, especially when designing components with large area to volume ratios, such as the microstruts forming the lattices.

2.3 Mesoscale

At this level, mostly geometric features are incorporated in the design, although they are not exclusive of powder bed fusion technologies, these methods have shown probably the most versatile and controlled free forming capabilities for creating open-cell cellular metals. Thus, it is important that the geometric attributes are considered when designing cellular solids fabricated by powder bed fusion systems. Here, the mechanical properties of the lattice are customized by modifications in the architecture of the unit-cell. The important factors at this level include stochasticity, nested hierarchical levels, aspect ratio, the Maxwell stability criterion, relative density, and auxetics. Noteworthy is that changes in these factors will inherently result in different cooling and solidification rates, with the possibility of substantial alterations in the microstructure (Kwon, Cooke, and Park 2003; L. E. Murr et al. 2010; Yang, Harrysson, et al. 2012). The geometric factors at this scale can be considered to be the major contributors to the mechanical properties of the cellular solids.

2.3.1 Stochasticity

Additive Manufacturing has made possible the fabrication of unit-cells in practically limitless shapes; however, the deformation mechanisms influencing the performance of the cellular solid are, in general, the same. The introduction of hierarchical levels is mostly what transforms a constituent solid into a metamaterial. The most general differentiation between cellular materials is that from observing its networking: stochastic or foams, and non-stochastic or lattices (Figure 2.6). Lattices were observed to fail in a more predictable manner while displaying

more uniform properties, better structural performance, and more damage tolerance when compared to foams (Gorny et al., 2011; Wallach and Gibson, 2001).

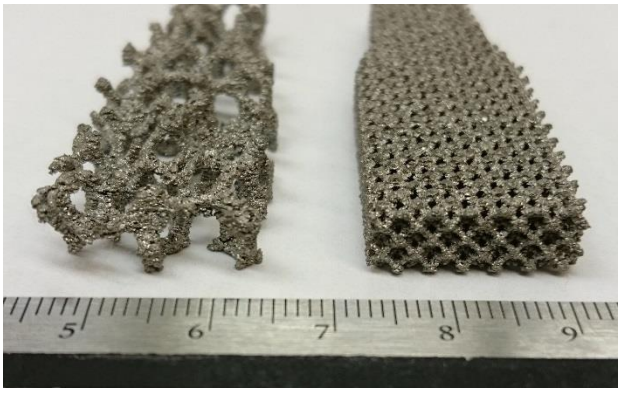

Figure 2.6 EBM fabricated Ti-6Al-4V cellular solids: foam (Left) and lattice (Right).

2.3.2 Nested Hierarchical Levels

Materials in nature display hierarchical structures at different scales; a common example is the bamboo, where hierarchical levels with different densities can be identified across the stem resulting in the large moment of inertia required to withstand the large bending deformations; similarly, the material phases discussed at the microscale are seen as embedded levels in the unit-cell. It has been determined that nesting hierarchical levels improves the mechanical properties and enhances the energy absorption capabilities of cellular materials (Vigliotti and Pasini 2013). Additionally, the embedded hierarchical levels can constitute cellular solids with different and specific stages of response for superior damage tolerance. Aided by AM powder bed fusion, the material designers are now able to nest multiple hierarchical levels and enhance the material properties. In the form of 3D hexagonal and 3D reentrant hexagonal, the lattice specimens for this study enclosed single-level unit-cells only (Figure 4.15).

2.3.3 Aspect Ratio

The mechanical response of lattices also reacts to the aspect ratio of the unit-cell; research work suggests its influence on the compressive strength and stiffness, independently of the architecture of the unit-cell (Gümrük and Mines 2013; M. Smith, Guan, and Cantwell 2013; Ushijima et al. 2011; Yang, Harrysson, et al. 2012). Similar to the slenderness ratio on microstruts, under compression, tall and narrow unit-cells are expected to display higher yield strengths when loaded vertically, but they are more likely to collapse by elastic buckling if they lack of proper lateral support. The designer should be aware of this instability in the unit-cell which can be alleviated by the lateral support of the adjacent cells.

2.3.4 Maxwell Stability Criterion

The topology of the network in cellular solids defines the forces acting on the microstruts carrying the load. Therefore, for energy absorption applications, the unit-cell structure needs to be designed to deform while distributing, absorbing, or storing energy; thus, maximizing its specific energy, which is defined by the area under the stress-strain curve divided by the density of the cellular solid. Considering the type of forces developing in the microstruts, the unit-cells are typically referred as *stretch-dominated*, or *bending-dominated* (Ashby 2006), however, because the inherent unidirectionality of the *stretch-dominated* term, and the possibility of the microstruts acting under tension, or compression, the term might not be appropriated. In that manner, the deformation of these structures can be: *axially-dominated*, when the loading is mostly axially dispersed along the microstruts, or *bending-dominated*, when the loading distribution originates moments at the nodes. Here, the nodal geometry and the slenderness ratio of the microstruts play an important role in resisting moment effects.

The unit-cells require to be analyzed and determined if they will behave either as axially-dominated, or bending-dominated; and evaluating the *necessary* generalized Maxwell's criterion (Maxwell 1864) is enough to determine it for most of the configurations. It is important to

emphasize that axially-dominated structures are generally stiffer and stronger, but they normally collapse abruptly; whereas bending-dominated lattices collapse progressively, a desirable feature for energy absorption applications such armoring and shock absorbers. (Deshpande, Ashby, and Fleck 2001; Ushijima, Cantwell, and Chen 2013, 200; van der Giessen 2011; Zhu et al. 2010).

The Maxwell stability criterion can be used to determine if a structure deforms either axially-dominated or bending-dominated. A generalized matrix approach on a generalized Maxwell stability criterion was presented by (Pellegrino and Calladine 1986) to additionally detect the absence of kinematic equilibrium as another requirement for a rigid axially-dominated structure. The analysis can also provide insight of how biased the structure is toward the Axially-dominated threshold; where, purely axially-dominated unit-cells are defined by $M \geq 0$ (Figure 2.7) (Pellegrino and Calladine 1986). The generalized Maxwell Criterion for 3D structures is given by:

$$M = b-3j+6 = s-m$$

Where $M<0$ indicates that a unit-cell with b number of struts, j frictionless joints, s number of self-stress states, and m number of possible mechanisms will collapse in mechanistic manner (bending-dominated). For simplicity purposes, note that the simple Maxwell stability criterion ($M = b-3j+6$) is a *necessary* condition, and we can identify that the axially-dominated unit-cells ($M \geq 0$, statically + kinematically determined) are those strictly formed from stiff triangles only, with no hinges at the nodes.

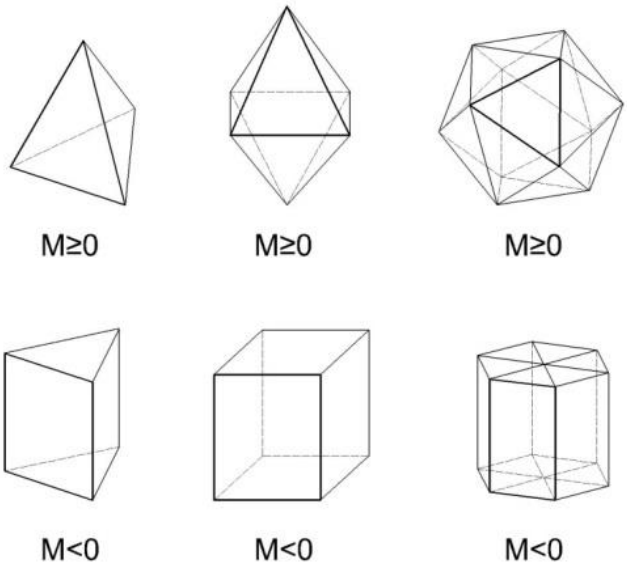

Figure 2.7 Example of axially-dominated and bending-dominated unit-cells, where axially-dominated unit-cells are characterized by triangles only.

Given that the Maxwell criterion considers frictionless joints, friction-equivalent expressions in function of the defined yield strength of the material at the node could be developed to predict the formation of plastic hinges and determine the nodal design to permit it. This will enhance the mechanistic deformation, material recovery, and specific energy.

Considering a purely geometrical approach, the limited deformation capability of axially-dominated cellular metals can be increased by the inclusion of substantial amounts of material phases characterized by ductile crystalline structures such as HCP. In this manner, we can compensate, or extend, the deformation capabilities of the cellular solids and their constituent solid materials by design approaches at different scale levels.

2.3.5 Auxetics

Since the first reported designed negative Poisson's ratio material (R. Lakes 1987), it has been mostly polymers that have been produced with this characteristic. These auxetic materials can still be considered rare, but now easier to design and fabricate thanks to AM technologies. Powder bed fusion systems make possible the fabrication of engineered metals with negative

Poisson's ratio. Materials with negative Poisson's effect have a shear modulus substantially larger than their bulk modulus, thus superior behavior against torsion, bending stiffness and energy absorption efficiency are expected (Yang, Cormier, et al. 2012). A variety of auxetic architectures can be developed to take advantage of their high shear modulus. Some auxetic geometries can experience different stress distribution modes as they are able to reconfigure themselves under loading, and displaying a new stage in the response that it is different than that of the original unit-cell configuration (Figure 2.8 and Figure 4.19) (R. S. Lakes and Witt 2002; Larsen et al. 1997; C. W. Smith, Grima, and Evans 2000; Warren 1990; Yang, Cormier, et al. 2012).

2.3.6 Relative Density

Defined as the ratio of the density of the cellular solid divided by the density of its constitutive solid, the relative density has been found in many cases to be proportional to the elastic modulus and strength. This is the cornerstone of the widely and experimentally accepted Gibson and Ashby model for the mechanical properties of cellular solids (Ashby 2006). However, this experimental relationship presents inaccuracies as the relative density increases (Liebenstein, Sandfeld, and Zaiser 2016; Sing et al. 2016).

The Gibson and Ashby model for E and σ. Where E is the Elastic Modulus, ρ is the density, $\boldsymbol{C}$ and $\boldsymbol{n}$ are experimental constants; s subscripts denote solid material

$$\frac{E}{E_s} = C\left(\frac{\rho}{\rho_s}\right)^n \quad ; \qquad \frac{\sigma}{\sigma_s} = C\left(\frac{\rho}{\rho_s}\right)^n$$

It is important to have in mind that focusing only in increasing the relative density to obtain stronger lattices may lead to unexpected results and inefficient structures (Sing et al. 2016). In that manner, we could be incrementing the density by adding only idle material; it is only when conjugating the effect of effectively increasing the relative density with all variables discussed in this chapter, that the designer can fully represent the complex optimization problem being

addressed and whose objective function is to make the constitutive solid the most useful in absorbing, storing, or dissipating energy.

The relative density of a lattice can be changed in different manners. Powder bed fusion fabrication allows for a controlled and effective material distribution. Alternatively, changing the relative density of the lattice by modifying the unit-cell size, for example, the cross-section of the microstruts could result in a more suitable slenderness ratio to resist or favor buckling. Similarly, at the nodes in the lattice, the amount and placement of the deposited material affects the development of plastic hinges during deformation. In that manner, an approach for adding the minimum amount of material required is to produce microstruts and nodes with geometrical features that enhance their moments of inertia.

2.4 Macroscale

Similar to the mesoscale, the characteristics at the macroscale level may not be exclusive of EBM, but as mentioned before, it probably is one of the most versatile methods to fabricating cellular metals. One of the most useful and practical analyses that can be done on the performance of cellular materials, as a solid itself, is by determining its stress-strain curve to be able to interpret behaviors and diagnose the most convenient attributes to modify toward the desired performance (Figure 2.8). The important factors at this level include: lattice orientation, deformation mode, brittleness, recovery, and unit-cell specifics. At this stage, because the many uncertainties, the design strength of the lattice is recommended to be estimated by the superposition of the individual strength of the unit-cells. This is the convenient scale level for reverse engineering and material development.

The compressive response of cellular materials is ideally characterized by three major phases. First, an elastic region, up to the yielding point in which the microstruts start to buckle, fracture or yield. As the structure progressively collapses at nearly constant stress, the stress-strain curve displays a plateau; this second stage is often where the majority of the energy from loading

might be absorbed. Once all the unit-cells levels have collapsed, the stress steeply rises, indicating the start of the densification stage, when the collapsed microstruts make significant contact and create friction with each other filling the remaining void space in the collapsed lattice (Ashby 2006) (Figure 2.8a).

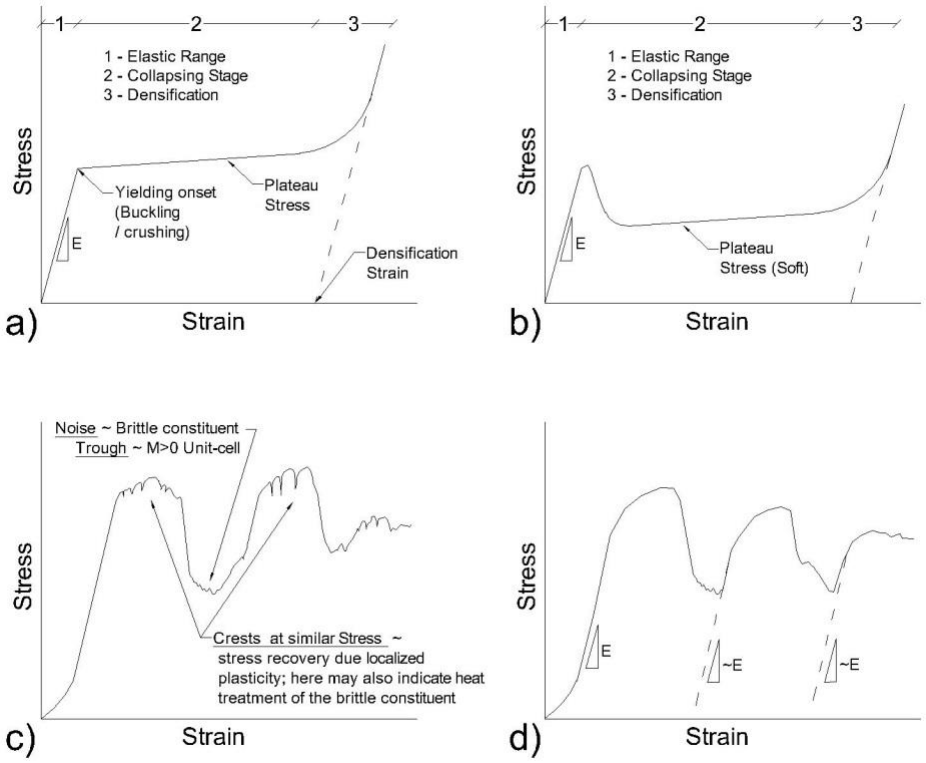

Figure 2.8 Representations of different compressive responses of cellular solids, highlighting behavior originated by specific features. a) Ideal 3-stages Response of ductile, bending-dominated lattices ($M<0$); b) 3-stage response of brittle, axially-dominated lattices ($M\geq0$); c) expected response of lattices fabricated with brittle constituents; d) Expected cyclic response of auxetic, self-bracing unit-cells.

2.4.2 Lattice Orientation

The overlapping effect inherent to powder bed fusion fabrication especially affects the properties of microstruts with oblique manufacturing angles (Figure 2.9). Orthogonally symmetric cells react stronger and stiffer when loaded parallel to the manufacturing direction, thus *sharper* shaped stress-strain curves are expected whereas shorter and longer curves are related to loads

applied perpendicularly. Besides the unit-cell design, these step-like features can also result in cellular solids with noticeable orthotropic properties (Figure 2.10). It should be mentioned that for the purposes of energy absorption, a long stress-strain curve with constant stress is generally preferred as the area underneath typically is larger compared to thin and tall curves (Cansizoglu et al. 2008).

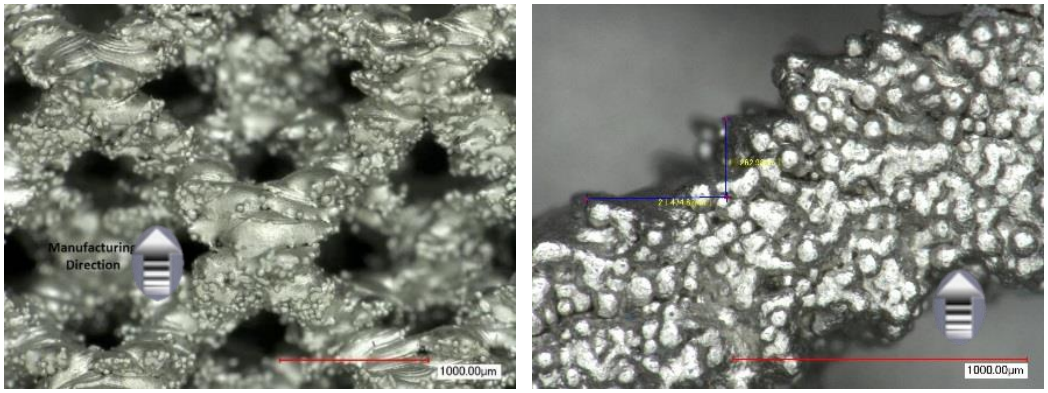

Figure 2.9 Node and microstruts in a lattice (left). 60° microstrut in a hexagonal lattice, highlighting step-like features measuring 480µm long by 250µm tall, approximately (right). 1mm scale marks.

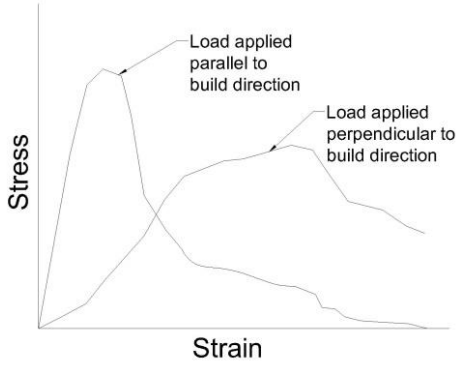

Figure 2.10 Schematic responses of orthogonally symmetric cellular solids to the loading direction.

2.4.3 Deformation Mode

Lattices formed by axially-dominated unit-cells ($M \geq 0$) are normally stiffer and possess higher yield strengths when compared to bending-dominated lattices ($M < 0$), however, they display a soft plateau stress when collapsing. Thus axially-dominated lattices are normally stronger, but bending-dominated are better performers for energy absorption purposes, as they display long plateau stress without the softening (Figure 2.8a and Figure 2.8b). Further analysis of the *necessary* Maxwell stability criterion, for lattices to deform as structures, not as mechanisms, makes evident that only the unit-cell architectures whose microstruts configuration is exclusively based on triangles can create strictly axially-dominated lattices (Ashby 2006; van der Giessen 2011).

2.4.4 Brittleness

A brittle constituent can be identified by several stress fluctuations in the collapsing stage. As the unit-cells progressively collapse in a catastrophic manner, the stress-strain curve resembles a noisy signal-like graph (Figure 2.8c) (X. Y. Cheng et al. 2012; Lorna J. Gibson and Michael F. Ashby 1999). Furthermore, a deeper understanding and analysis on the constitutive solid and its relationship with these fluctuations could be helpful in the identification and quantification of material phase transformations occurred during the fabrication of after heat treatment.

2.4.5 Recovery

Peak stresses in the stress-strain curve normally describe the progressive collapse of groups of unit-cells, where each peak ends with the failure of one of these groups and the loading redistribution to another group, affecting a whole unit-cell level, or several unit-cells from various levels. Peak stresses failing to regain a previous maximum stresses could indicate brittle unit-cells with accumulated damage; this, given the scarce development of plastic hinges permitting the release of stress and recovery in the material (Figure 2.8d); whereas buckling microstruts in ductile structures come in contact and redistribute the stress without major ruptures. Constant stress from

the plasticity in the buckling process, permit the next weakest level of cells to recover and withstand a second stress of similar magnitude (Figure 2.8d). When manufacturing lattices made of constituents known to be brittle show consecutive stress peaks of similar magnitude it may suggest a post-manufacturing heat treatment favoring ductility. This behavior could be investigated as indicator of the effectiveness of the treatment leading to phase transformations (X. Y. Cheng et al. 2012; Gorny et al. 2011; Hernández-Nava et al. 2016).

2.4.6 Unit-cell Specifics

Microstruts fabricated with variable cross section, specific local orientation, nodal geometry, reentrant angles, multimaterial (Mireles 2016), and others, are examples of more specific features that can be engineered into the unit-cells for a tailored response. These singular features combined could result in unique stress-strain curves with a variety of behaviors; for example, a reentrant hexagonal unit-cell may initially display a nonlinear section, followed by a linear, probably stiffer, section in its stress-strain curve, after changing its configuration an axially-dominated one (Figure 4.28) (Deshpande, Ashby, and Fleck 2001; Yang, Harrysson, et al. 2012). The contribution of these features should be analyzed independently such as in the case of unit-cells with auxetic behavior, where these cellular solids are normally expected stiffer and stronger.

2.4.7 Remarks on the Multiscale Analysis Approach

At a microscale, hierarchical levels in the microstructure can be controlled through the manufacturing settings by promoting the formation of convenient atomic arrangements in the solid. Mesoscale attributes are practically limited by imagination in the designing of unit-cells since almost any topology can now be introduced in the solid. Finally, at a macroscale, the response can be controlled by the quantity and arrangement of the unit-cells.

Just as the crystalline structures represent the minimum unit of volume containing the structural and geometric information to characterize solids, the macroscale unit-cell is similar for

the cellular materials, thus it is expected that the topology at the mesoscale level contributes the most toward the overall response.

An important aspect of the present work is to encourage and prioritize the comprehensive knowledge of the cellular metals towards a better understanding of their design. Thus, the multiple factors contributing to the performance of these materials have been presented according to scale (Table 2.1). In this manner, after the understanding of the service requirements, it is advisable to start the conceptual design at the mesoscale, where the determinant factors are highly customizable and are major contributors to the performance of the cellular solid. For example, where energy absorption is of special interest, a cellular metal could be designed as a lattice, with a primary level of unit-cells with $M<0$ embedding a softer $M<<0$ hierarchical level for energy dispersion, with equilateral 3D aspect ratio, and non-auxetic. Once the unit-cell has been conceptualized, the design is enhanced at the microscale where the variables are less controllable; thus, EBM Grade 2 Titanium may be a good option given its formability, lightweight, and corrosion resistance. In this case, the effects of manufacturing parameters shall be analyzed for the possibility to promoting the stiffer β-phase in the primary unit-cells, and produce the α-phase in the secondary level. The degradation of the mechanical properties could be addressed by either oversizing the microstruts, or by obtaining all-inclusive material properties from specimens that include manufacturing defects. Variability of the mechanical properties product of the manufacturing process are recommended to follow a more statistical approach, especially if the manufacturing systems serve different operations. As the common file format for AM system, the effects of *.STL* should be addressed together with the mechanical properties degradation until a more precise file format becomes dominant. At the macroscale the lattice manufacturing direction should be parallel to the direction of the main load for larger energy dissipation. Finally, the response of the cellular solid can be interpreted to identifying features to address and developing tailored responses; for example, consecutively lowering peak-stresses may suggest cumulative damage in a constitutive brittle solid; therefore, it could be advisable to search the lattice for regions where microcracking

may exist, evaluate the microstructure in these zones, and develop the methodology to promoting for the formation of more of the ductile material phase.

Table 2.1 Summary of the determinants of design followed in a multiscale analysis.

Determinant	Specific energy enhancement:	Variables
Microscale		
Manufacturing Technology	EBM builds normally display lager elongation that SLM.	Powder bed fusion technologies.
File Format	.stl is currently the common file in additive manufacturing technologies. It implies discretize geometries into triangles that may limit the design and introduce flaws and defects.	.stl, CAD, others available.
Constituent solid	Prefer those with atomic structures recognized to deform as mechanisms and similar life cycles.	Available powder precursors and their condition.
Manufacturing Parameters	Increase energy and time of exposure for higher density, therefore less early failure. Control settings that produce ductile material phases.	power, time, layer thickness.
Manufacturing Process	Procure cooling and solidification rates that do not alter, but promote microstructures with ductile phases.	manufacturing layout, self-geometry, supports, process interruptions.
Degradation of the Mechanical Properties	Compensate for the degradation of mechanical properties due scale factor, mostly.	scale factor, slenderness ratio, layer thickness, orientation, CAD draft errors.
Mesoscale		
Stochasticity	lattices are normally more damage tolerant, more uniform properties, and fail in a more controllable manner	foams, lattices.
Nested Hierarchical Levels	Include nested levels that enhance energy absorption.	number and individual performance of nested levels.
Aspect ratio	Prefer Slenderness ratios close to 1.	length, width, height, slenderness ratio, effective length.
Maxwell Stability Criterion	M<<0	number of joints, number of self-stress states, number of mechanisms.
Auxetic	Negative Poisson effect normally increases stiffness; as a general advice, avoid purely auxetic structures.	re-entrant angles, unrestricted motion.
Relative density	Density is normally proportional to strength, but not necessarily a major contributor for specific energy.	nodal geometry, microstrut aspect and slenderness ratios.
Macroscale		
Lattice Orientation	Prefer layering deposition direction to be perpendicular to the expected loadings.	x, y, z
Deformation Mode	Prefer bending-dominated lattices.	M, nodal geometry, microstrut aspect and slenderness ratios.
Brittleness	Avoid geometry brittleness.	Constituent precursor.
Recovery	After the collapse of a unit-cells level, the stress recovery will extend specific energy.	Constituent precursor, topology, post-manufacturing treatments.
Unit-cell specific	uniquenesses of unit-cells can benefit specific energy.	Imagination.

It is important to mention that the concepts discussed herein may also be valid for materials other than metals, such as polymers with highly deformable molecules. Future work of this approach may include its expansion to structures with more scale, or energetic levels, as well as their responses under dynamic loads.

Additive Manufacturing technologies provided the opportunity for practically unlimited unit-cell designs. The design of cellular materials, as a discipline, is not close to a standardized system of theories, methods, however, with the multiscale analysis approach herein, the identification of determinants of design has been structured. Nonetheless, it is still on the experience, availability and convenience of the designer to discern which of the presented attributes to customize toward achieving the expected lattice response.

On the investigation of the mechanical properties of EBM Ti-6Al-4V, as the constitutive solid for this work, the following Chapter 3 presents a series of experiments dedicated to evidencing and characterizing this material at different orientations and under different loading conditions, besides generating the material properties input data to assigning to the elements in the development of FEMs; whereas Chapter 4 further interprets and merges the experimental findings into the multiscale analysis, as proposed in this chapter.

Chapter 3: Material Properties Characterization

The mechanical properties of metal components fabricated by powder bed fusion are influenced by many factors inherent to the process (Gong et al. 2013; Hernández-Nava et al. 2016; Hrabe and Quinn 2013); for example, the surface texture of builds is characterized by sintered precursor powder particles and pores that can act as stress concentrators threatening the integrity of the parts. Additionally, the localized way in which the energy to melt the powder particles is delivered, linked to the cooling and solidification rate can result in microstructures particular of this fabrication method. Furthermore, the orientation with respect to the powder bed (Figure 3.1), in which the part is manufactured, probably is among the most studied characteristics affecting the mechanical properties of components fabricated by powder bed fusion; for example, under tension, cylindrical bars fabricated parallel to the horizontal plane (0°) are expected to be stronger that those fabricated perpendicularly (90°), given that the material layers have been deposited along the bar, and are parallel to the load, therefore, the strength is not compromised by any defects that may occur in the layers interface. Moreover, from observing the fabricated lattices (Figure 1.4), solid bearing plates and microstruts at different orientations, presumably with different mechanical properties, can be identified. For the measurement of properties, a Digital Image Correlation (DIC) system was mostly used; this system records images at specified time intervals of the deforming specimens during tests, and measures deformations by tracking displacements of defined points on visible surfaces from one image to another, in that manner, strain fields can be measured by tracking several points in the specimen, or virtual tools such as extensometers, can be used to compare two specific points. By synchronizing DIC with the system applying the load, it is possible to obtain the stress-strain relationship without any contact to the specimen, neither the need of special instrumentation for specimens with complicated shapes. Thus, in the understanding and measurement of the mechanical properties of the metal under these different conditions and orientations, part of this investigation consisted in different experiments resembling these conditions to generating the necessary stress-strain curves as input data for the finite element

models, where the generated data should be assigned to the elements with similar conditions and orientation in the lattice.

These series of experiments were conducted on specimens designed in Solidworks and exported in STL format for fabrication using Ti-6Al-4V prealloyed precursor powder from ARCAM AB in an ARCAM A2 system with ARCAM AB's standard parameters for 50μm layers. The tested components consisted of cylindrical ASTM E8 and E9 specimens fabricated at 0°, 30°, 60° and 90°; 0.8mm x 0.8mm x 73mm wires fabricated at 0°, 30°, 45°, 60° and 90°; and hexagonal and reentrant hexagonal lattices at three different densities (Figure 1.4). The standard manufacturing parameters consist of layer-by-layer preheat steps taking place to maintain the fabrication environment at approximately half of the material's melting point (~700-760°C for Ti-6Al-4V). Powder within the fabrication environment is deposited using a raking mechanism and selectively melted using a current of up to 18mA with beam speeds of 500-1,000mm/s. The process takes place in a high vacuum environment of up to 10 -4mBar and repeated until fabrication is complete. The specimens were fabricated in variants of orientation at 0°, 30°, 60° and 90°; only microstruts were fabricated at an additional orientation of 45° (Figure 3.1). Components fabricated at 30° and 60°, except microstruts require support for good quality fabrication (Figure 3.2); additionally to restraining the components in the powder bank inside the build chamber, and supporting it from the effects of gravity, the main purpose of manufacturing supports is the relief of thermal gradients originating distortions and residual stresses during the cooling and solidification of the metal. It is important to note that although the manufacturing settings were set same for all, the manufacturing space restrictions and production schedules of the EBM system made it difficult for the specimens to be fabricated in a single batch. Once the process has been completed, the solid components have higher density and gained more heat than the surrounding powder material, thus the heat loss can be different through the chamber, and potentially affect differently the formation of microstructures in the solidifying metal. The orientation and identification of specimens are of special importance and were preserved at all times; labeling of specimens consists of three parts: two first digits indicating the build angle followed by the suffix

"deg" for degrees, and ending with a unique numerical identification number. Capitalized "DEG" denotes specimens whose strain has been measured by virtual and physical means. For example, 60DEG12 stands for a standard tensile test specimen fabricated at 60° manufacturing angle, measured with clip and virtual extensometers. All testing is conducted at room temperature of 23 °C and 37% relative humidity.

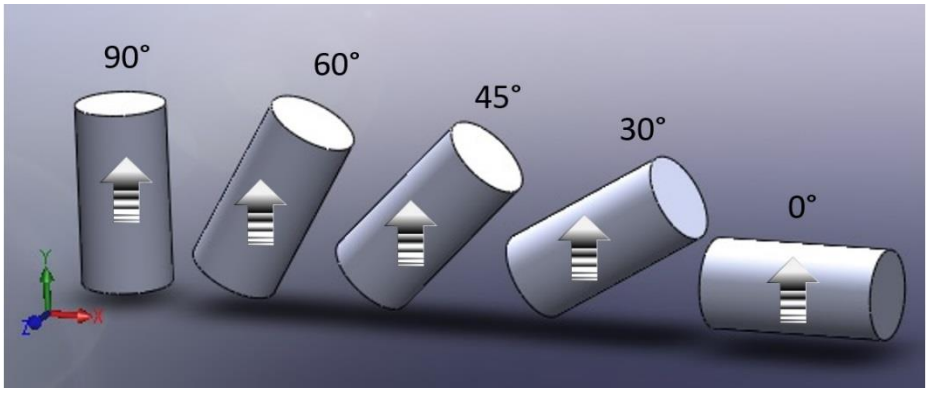

Figure 3.1 Schematic of components fabricated at different build angles. XZ defines the powder bed plane and Y indicates the direction of the beam; arrowheads indicate the building direction (vertical, parallel to the beam) while hatch represents the layering pattern.

Further analysis and interpretation of the results of the discrete testing is merged into multiscale design approach in Chapter 4, where multiple and manageable factors influencing the performance of cellular metals are discussed.

3.1 ASTM E9 Standard Compression Test of EBM Ti-6Al-4V

The main objective of this test was to set a benchmark for the comparison between titanium in lattice and solid forms. All apparatus, specimens and procedures are in accordance to ASTM E9 (ASTM International 2009).

3.1.1 Specimens

Three specimens of each manufacturing orientation were tested 3x(0°, 30°, 60°, 90°). Medium-length specimens were selected as they are the recommended size for determining the compressive strengths of high-strength materials. The specimens had and average weight of 11.68g, 12.25mm diameter, and 25.04mm height, for L/D ratio close to 2.0. The surface of the cylinders was CNC machined following ARCAM recommendations (Arcam, n.d.) to reduce stress concentrators, mostly, from the removal of the required supports for low angle manufacturing (Figure 3.2).

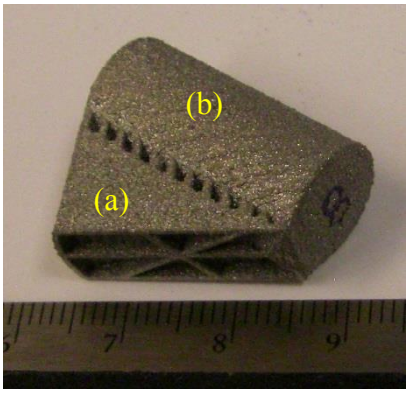

Figure 3.2 30° specimen (a) with support (b), as-fabricated from ARCAM A2 system.

3.1.2 Apparatus

The compression test specimens were tested as per ASTM E9 standard in an Instron 5594 universal testing machine with an installed load cell capacity of 70MN and equipped with 9in compression high carbon steel platens with spherical seat (Figure 3.3).

Figure 3.3 70MN Instron 5594 UTM and compression platens with spherical seat.

Taking necessary provisions to avoid damaging the steel platens by the harder Ti-6Al-4V specimens, linear finite element simulations were used for rapid prototyping of a bearing base aimed at distributing the stress (Figure 3.4a). The assembly to protect the plates consisted of a pair (top and bottom) of EBM Ti-6Al-4Al bearing bases built at 90°, supported in turn, by 2in x 2in x 1/2in commercial cast Ti-6Al-4V plates (Figure 3.4b). Loaded with a pressure 20% higher than the estimated maximum for the specimen to fail, the finite element model showed that the stress over the steel platens was less than the 80% maximum recommended by the manufacturer (Figure 3.4c). Moreover, an isosurface with stresses over 80% of the typical EBM Ti-6Al-4V 950MPa yield stress reported by ARCAM showed that the high stresses that could potentially damage the steel plates were all within the rapid prototype bearing base, demonstrating the effectiveness of the support assembly (Figure 3.4d)

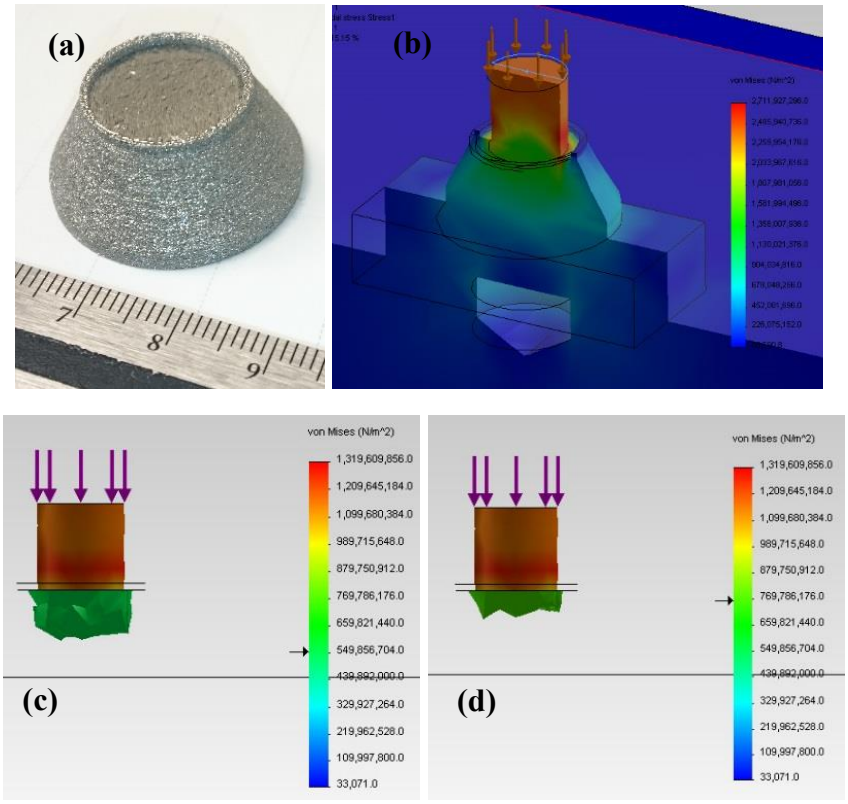

Figure 3.4 a) rapid prototype bearing base for compression test, b) cross sectional stresses in the assembly, c) isosurface at 80% maximum stress recommended for the steel platens, d) isosurface at 80% the EBM Ti-6Al-4V yield stress.

3.1.3 Procedure

The specimens were carefully centered, aligned and mated with the bearing base and platens. A lithium complex additive lubricant was applied to the contact surfaces between the specimens and bearing base before each testing (Figure 3.5). Testing was controlled by crosshead speed equivalent to a strain rate of 0.003mm/mm·min. Testing was defined as complete after the strain exceeded 8%.

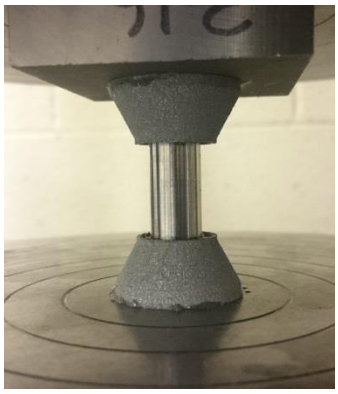

Figure 3.5 Specimen setup.

3.1.4 Results

The average stress-strain curves described a bi-linear behavior of the metal with a yield strength range of 1034-827MPa with a mean μ=944.24MPa and standard deviation σ=88.17MPa (Figure 4.10), compared to the 950MPa reported by ARCAM. The highest yield strength was observed for the 0° specimen. The strength progressively decreased as the building angle increased (Figure 3.6). The permanent deformation of all the specimens was that S-shaped typically observed for specimens with L/D=2.0. Regardless of the layering orientation, no significant differences in deformation mechanisms were noticed (Figure 3.7).

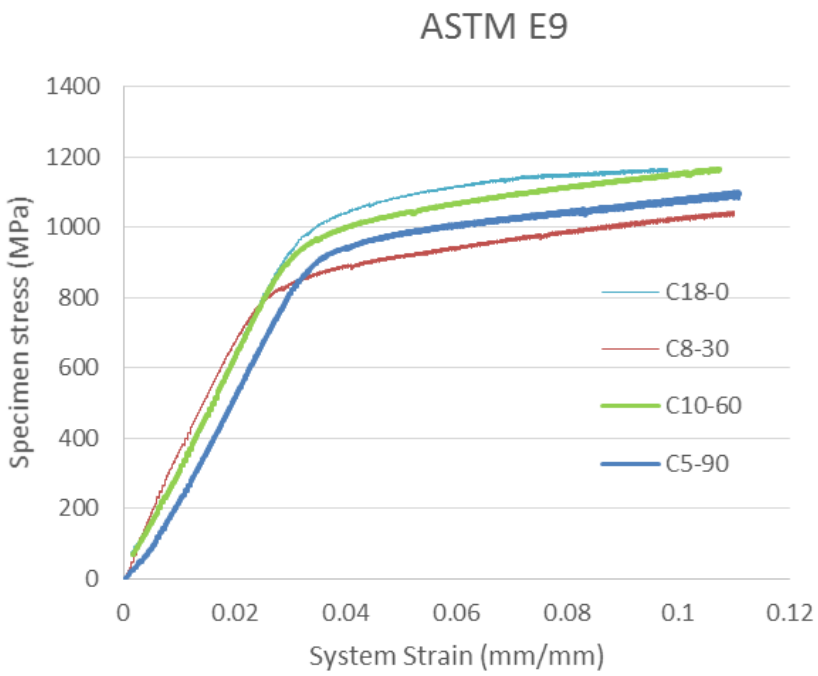

Figure 3.6 Compression stress-strain curve for EBM Ti-6Al-4V. Last two digits on the right in series name indicate built angle.

Figure 3.7 Permanent deformation of 0°, 30°, 60°, 90° specimens (left to right)

3.2 ASTM E8 Standard Tension Test of EBM Ti-6Al-4V

The objectives in conducting this test method included the determination of the mechanical properties of EBM Ti-6Al-4V fabricated at different angles, obtaining the corresponding stress-strain curve values for input to FEM, investigation of any size effects compared to microstruts and

the observance of any potential shear effects created by the manufacturing technique. All apparatus, specimens and procedures were in accordance to ASTM E8 (ASTM International 2016).

3.2.1 Test Specimens

Three specimens of each manufacturing orientation were tested 3x(0°, 30°, 60°, 90°). Round specimens with threaded ends were selected. The specimens were CNC machined from EBM Ti-6Al-4V rough cylindrical bars following ARCAM recommendations (Arcam, n.d.); the machined specimens averaged a weight of 19.7g, 5.9mm diameter, and 37mm gauge length. The specimens subjected to DIC testing were prepared with speckle patterns following CS recommendations with flat spray paint (Figure 3.8).

Figure 3.8 Standard tension test specimen painted with speckles for DIC (left). Speckle pattern (right). 1mm scale mark.

3.2.2 Apparatus

The standard tension test specimens were tested in an Instron 5969 UTM with an installed load cell capacity of 50kN equipped with threaded grips. An Instron 25.4mm axial clip extensometer was used for strain measuring. Additionally, a digital image correlation system (DIC) from Correlated Solutions (CS) was used to measure axial strain and strain fields by means

of virtual gauges and extensometers available in VIC-3D and VIC-gauge software, all from CS (Figure 3.9).

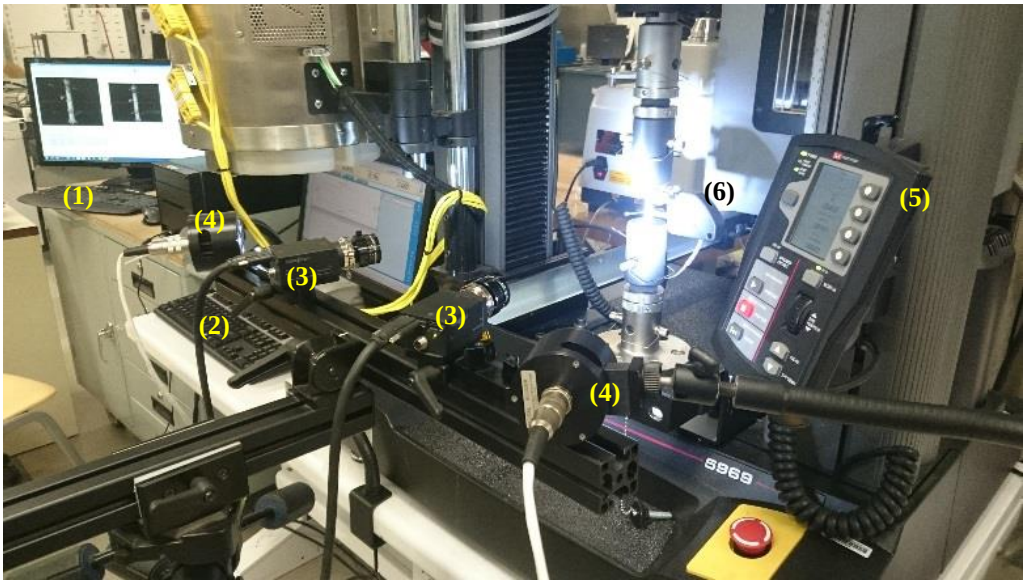

Figure 3.9 DIC workstation (1); UTM workstation (2); cameras (3); LED spotlights (4); UTM control module at the frame; clip extensometer installed in specimen (6).

3.2.3 Procedure

Specimens were installed in threaded grips; axial strain was measured by a 25.4mm clip extensometer. Axial strain was dual-measured with a clip extensometer and DIC virtual extensometer in one specimen of each orientation, for strain fields and DIC validation (Figure 3.10). DIC system was setup and calibrated as per CS recommendations. Testing was controlled by crosshead speed equivalent to a strain rate of 0.003mm/mm·min. until specimen failure.

Figure 3.10 Specimen setup for dual strain-measurement tests.

3.2.4 Results

The different orientations displayed stress-strain curves with bi-linear behavior and average yield strengths in the range of 820-1100MPa with median μ=971.25MPa, standard deviation σ=115.21MPa and c.o.v. = 0.119 (Figure 4.10), compared to the 950MPa reported by ARCAM, and the 758MPa and 860MPa required in ASTM F1108 and ASTM F1472 for cast and wrought Ti-6Al-4V respectively.

A comparison of stress-strain curves obtained from clip and virtual (DIC) extensometers displayed almost identical curves from both techniques, thus, validating the use of virtual extensometers to measuring deformations (Figure 3.11).

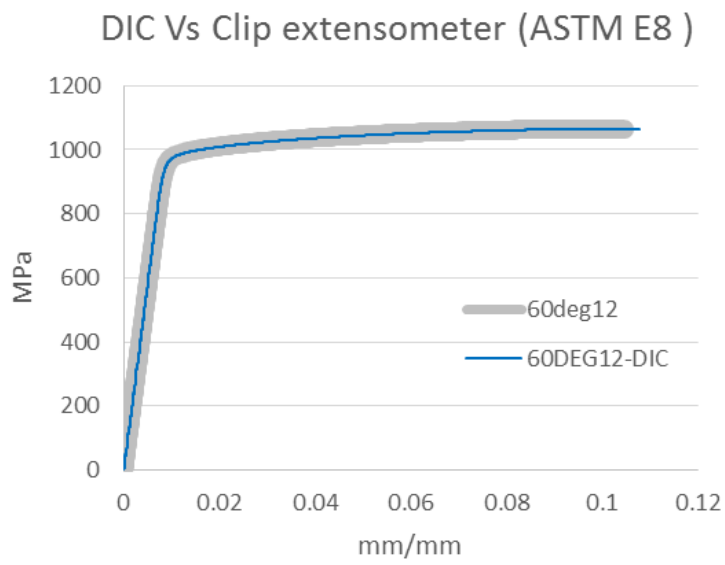

Figure 3.11 Strain measured by: virtual (thin line) and clip (thick line) extensometers.

The DIC system allowed for estimation of the Poisson's ratio from virtual gauges on areas of interest; values of 0.32, 0.30, 0.29 and 0.33 were found for the 0°, 30°, 60° and 90° orientations respectively at the failure region. The average Young's modulus determined during these tests showed similar to the 120GPa reported by ARCAM; the average elastic modulus for the 0°, 30°, 60° and 90° values were calculated as 115GPa, 103GPa, 110GPa and 110GPa respectively, displaying no significant variation due to the manufacturing orientation (Figure 3.12). However, when comparing the median specimen from each orientation, the yield and ultimate tensile strengths were found to be inversely proportional to the manufacturing angle, except for the 90° orientation (Figure 3.13). The presence of less and smaller flaws in the 90° specimens could have resulted in strengths surpassing the strength reduction effect due low build angles. Moreover, the lower strengths of 30° and 60° specimens is, in part, due the orientation of internal stress concentrators mostly originated by flaws present in the layering interface (Figure 3.14). Similarly, flaws could be critical when developing internal stress fields threatening the consistent higher material elongations than those required by ASTM standards (Figure 3.12). Therefore, the assurance of quality builds is extremely important in predicting materials performance. Quality assurance of additive manufacturing metal components is still an extremely challenging task given

the sensitivity of the components to the many known, and probably still unknown, factors such as precursor quality, cooling rate, manufacturing process, manufacturing settings and manufacturing orientation, each of these dependent of complex relationships between multiple variables, a situation explained in extend in Chapter 2 and Chapter 4.

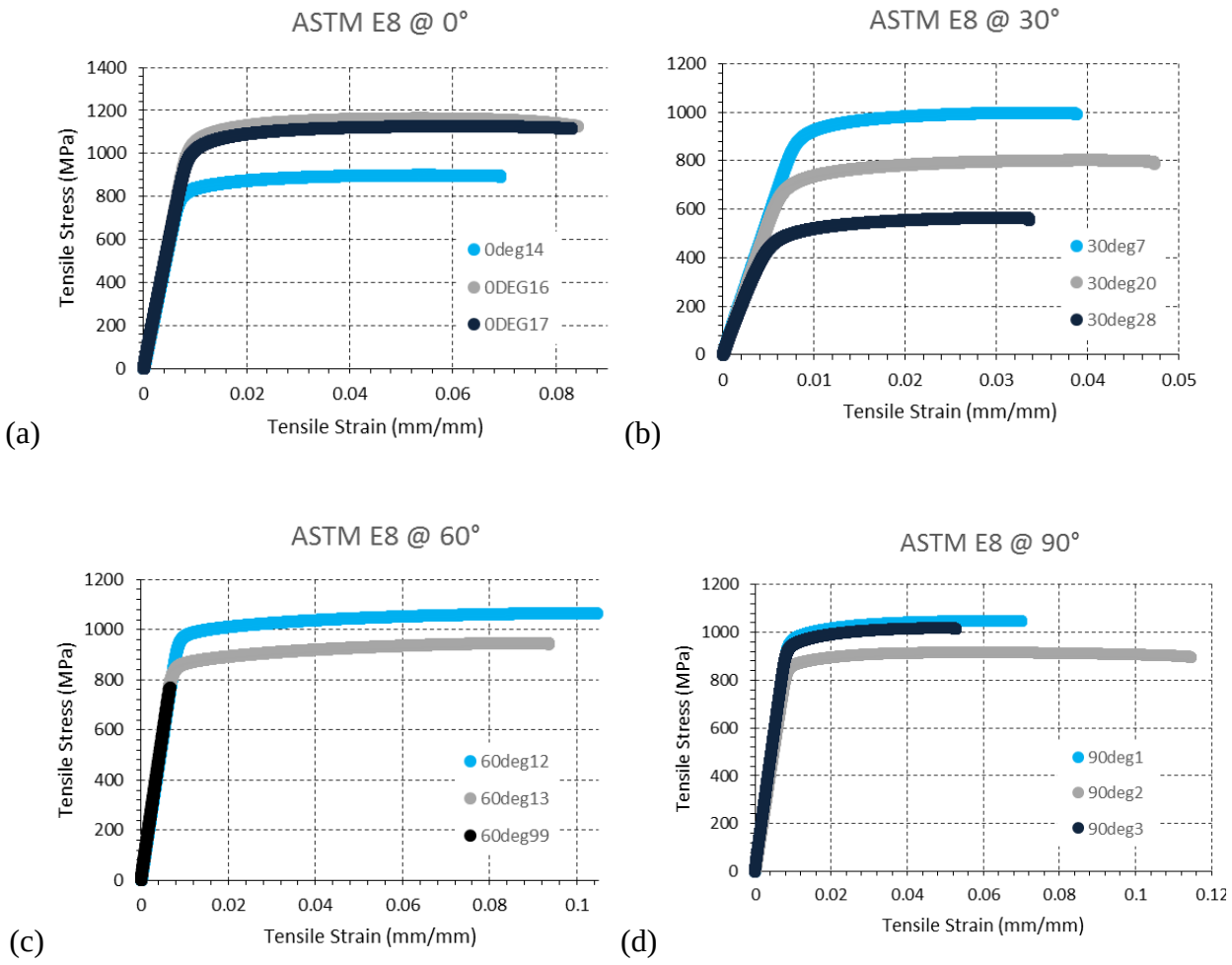

Figure 3.12 Tensile stress-strain of specimens at different orientations. 0° (a) to 90° (d).

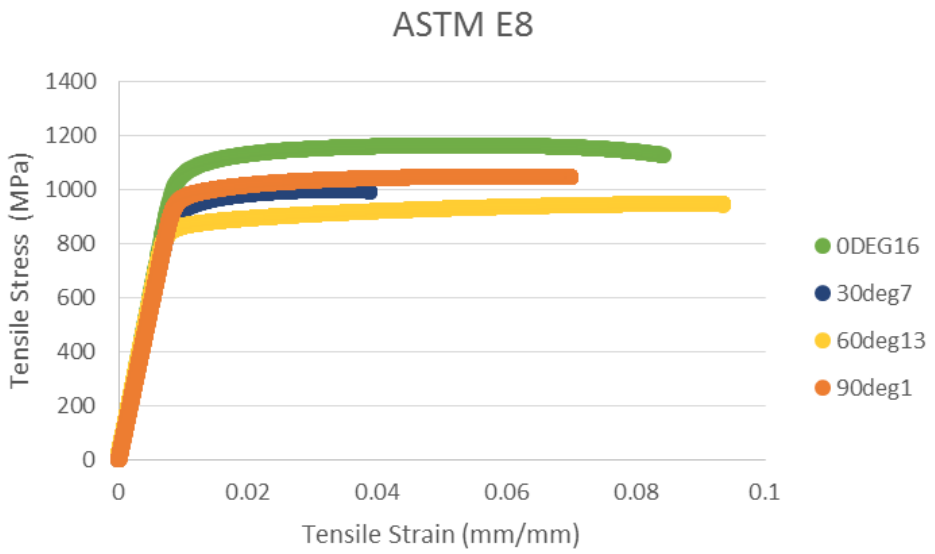

Figure 3.13 Tensile stress-strain curve of specimens at different build direction.

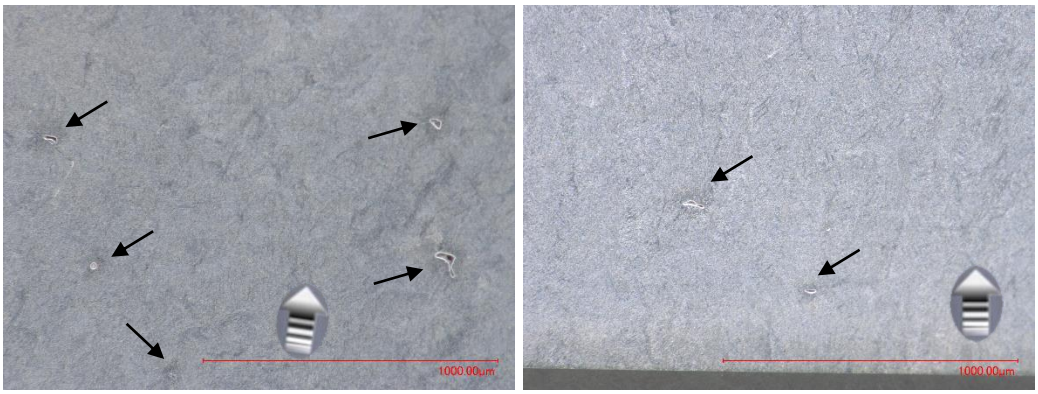

Figure 3.14 Optical microscopy of regions near failure of 30° (left) and 90° (right) specimens. 1mm scale mark.

The layering approach of powder bed fusion manufacturing suggests that shear bands could potentially develop under uniaxial loading. In the investigation of these shear effects, micrographs of the specimens showed a uniform metal matrix with no visible layer interface nor phase discontinuity (Figure 3.15) that could potentially result in the layers sliding over each other. However, strain field recordings developed by DIC showed different shear strains for differently oriented specimens. Although shear bands were not clearly identified in axial-asymmetric specimens (30°, 60°), scattered shear zones developed and added up to the strain tensor, thus likely

defining the fracture, whereas for axial-symmetric specimens (0°, 90°), the fracture was practically dependent on principal strains. The axial-symmetric specimens displayed Von Mises strain fields practically identical to the axial strains, resulting from the low and mostly constant shear strain fields. Slightly larger differences were found when comparing Von Mises to axial strains, this as consequence of the shear strain fields with scattered shear strain concentrations (Figure 3.16).

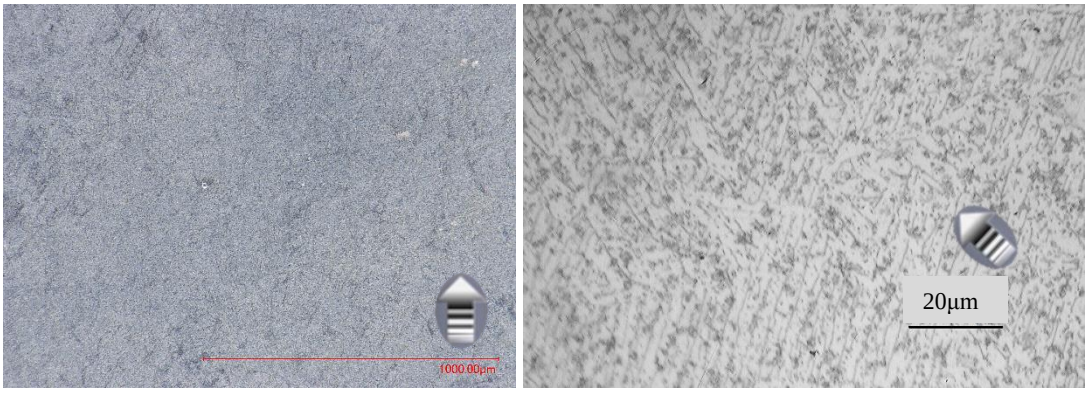

Figure 3.15 Micrographs of 90° specimen (left) and 30° Ti-6AL-4V microstructure.

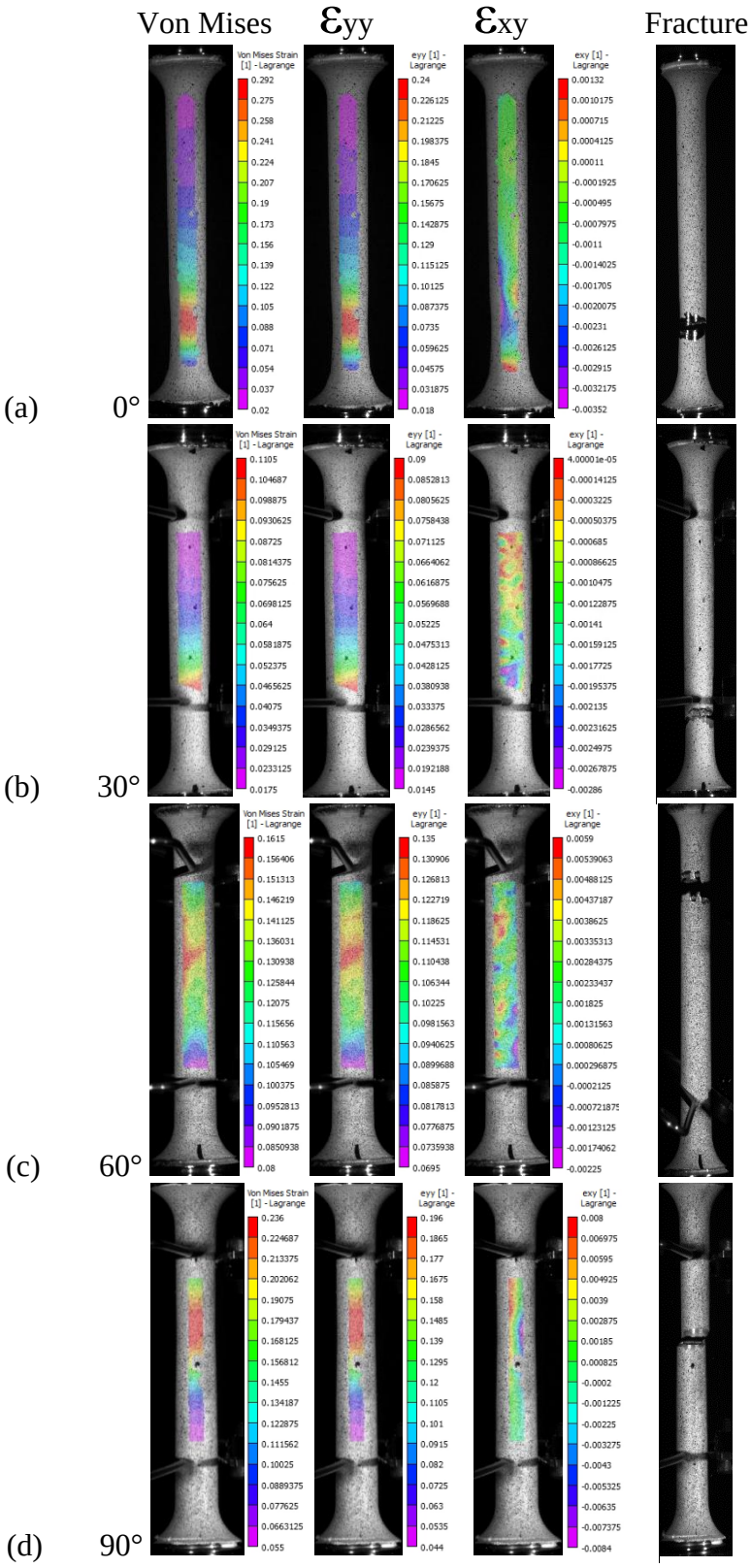

Figure 3.16 DIC strain fields comparison on specimens with different build angles.

Supporting the DIC recordings of shear effects, failure analysis revealed that shear stresses can develop in such a manner that could influence the failure modes of the components. From the fracture profiles of the 0° and 90° specimens, well defined features such as slight necking, shear lips and a failure plane normal to the main axial stress were observed, and are characteristic features of flat-face failure modes; a mode corresponding to a planar strain state from a triaxial tensile-stress system. On the other hand, the features in the fracture profiles from the asymmetric specimens were not clearly defined, indicating a stress system different than triaxial, thus the presence of larger shear strains (Figure 3.17).

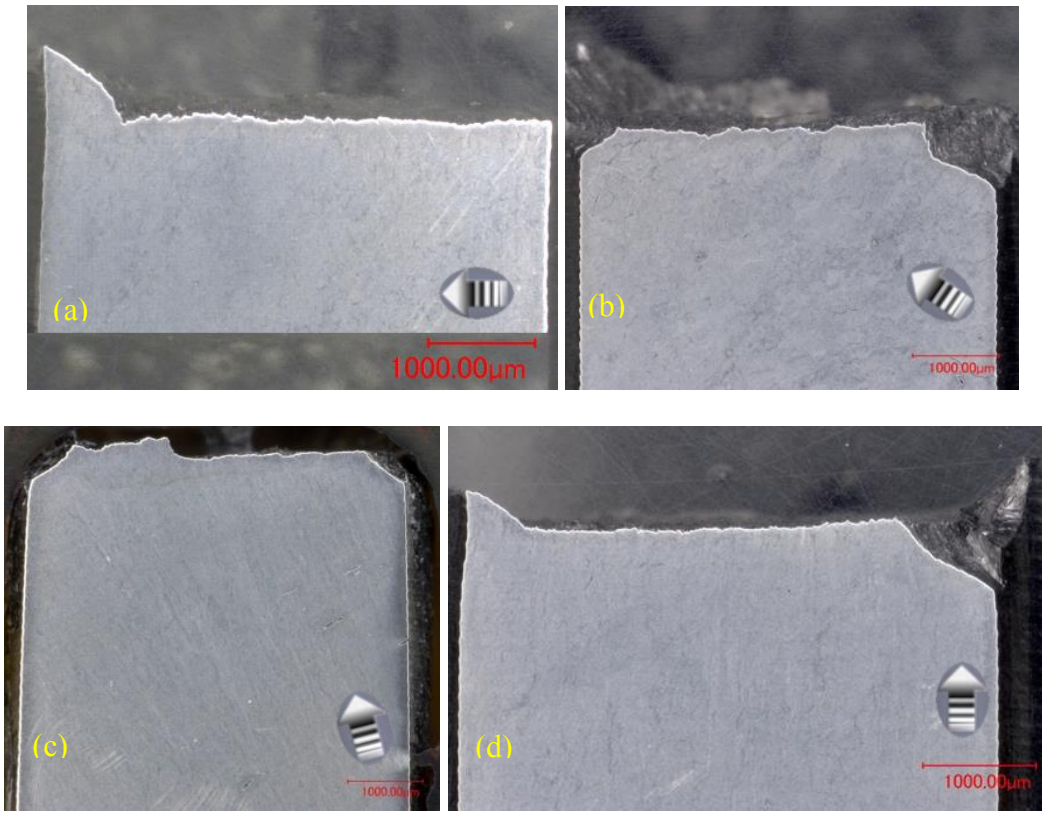

Figure 3.17 Failure profiles of 0°, 30°, 60°, 90° (a, b, c, d) specimens. 1mm scale marks.

The observed uniformity of the layering interface and material phase suggested them having minor influence in developing shear strains, and probably indicating flaws as the major contributors of these shear effects. It is important to be aware of the possibility of designing failure

modes by the development of strain fields that may counteract the most threatening strains by the intentional inclusion of manufacturing defects in the metal matrix that can also bias the component to less detrimental cracking.

3.3 Tension Test of EBM Ti-6Al-4V Microstruts

In exploring the possible approaches to obtain material properties under similar conditions to those within the lattices (Figure 3.18), long microstruts with different orientations were fabricated and tested under axial tensile loads. These tests allowed for the investigation of size effects influencing the mechanical properties of the Ti-6Al-4V. Procedures and apparatus were as much as possible in accordance to ASTM E8, as no standard specifically addresses testing of these specimens, to this date.

3.3.1 Test Specimens

Microstruts were fabricated at different manufacturing orientations (0°, 30°, 45°, 60° and 90°) (Figure 3.1). The specimens averaged 0.18g weight with nominal dimensions of 0.8mm x 0.8mm x 73mm. Because of their small mass, the thermal gradients are also small, and regardless of the orientation, none of the specimens required supports for a quality fabrication.

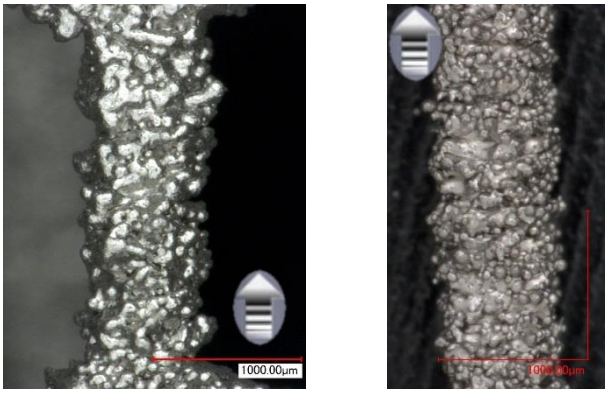

Figure 3.18 Comparison of a 90° internal microstrut in a hexagonal lattice (Left) and a 90° microstrut specimen (right). 1mm scale marks.

3.3.2 Apparatus

Microstruts were tested under tension in an ADMET expert 5603 with MTEST Quattro system, an installed load cell capacity of 4,500N, and equipped with wedge grips. Strain was measured using DIC system and VIC-gauge software, from Correlated Solutions (Figure 3.19).

Figure 3.19 ADMET expert 5603 (1); ADMET control (2); cameras (3); LED spotlights (4); wedge grips (5).

3.3.3 Procedure

Specimens were installed in the wedge grips; proper alignment was ensured by referenced observation, level and DIC. The grip length in the specimens was experimentally determined by trial and error as 17mm. The axial strain was measured by DIC virtual extensometer using Vic-gauge software. Noteworthy is the advantage of using DIC for strain measurements in specimens this small. The displacements are recorded only between previously specified points or regions of interest on the specimen imaging only, thus if any slipping may occur from the grips, or any other disturbance, it would not be recorded. The testing speed was controlled by a crosshead speed equivalent strain rate of 0.003mm/mm·min. until fracture of the specimen (Figure 3.20).

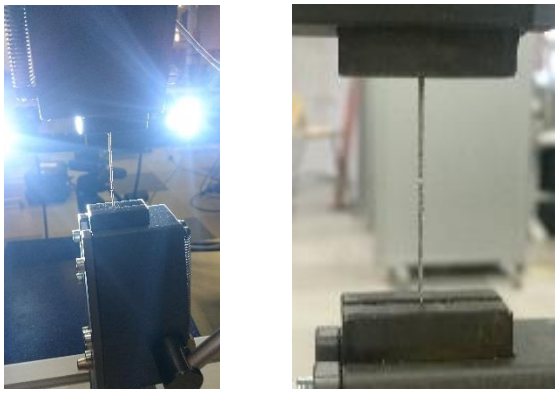

Figure 3.20 45° microstrut and DIC setup (left) and after failure (right)

3.3.4 Results

The stress-strain curves for the microstruts at different orientation were found describing a practically linear behavior with null plastic zone; the lack of plastic deformation, compared to the standard tension test specimens, is consequence of the size effect. The larger amount of the same material in the larger specimens represent more molecules, and therefore more molecules rearranging as well as more dislocation events withstanding ultimate stresses, thus describing a more noticeable plastic region before fracture.

The size effect also was found to influence the elastic modulus; regardless of the orientation of the microstruts, the values for this property were found to be significantly lower than those from the ASTM E8. An interesting finding is the variation of the Young's modulus with respect to the manufacturing orientation; in general, the elastic modulus tended to soften as the build angle increased. The step-like features from the layered fabrication may have a detrimental effect, where the ultimate strength of microstruts was observed to decrease as the build angle increased (Figure 3.21).

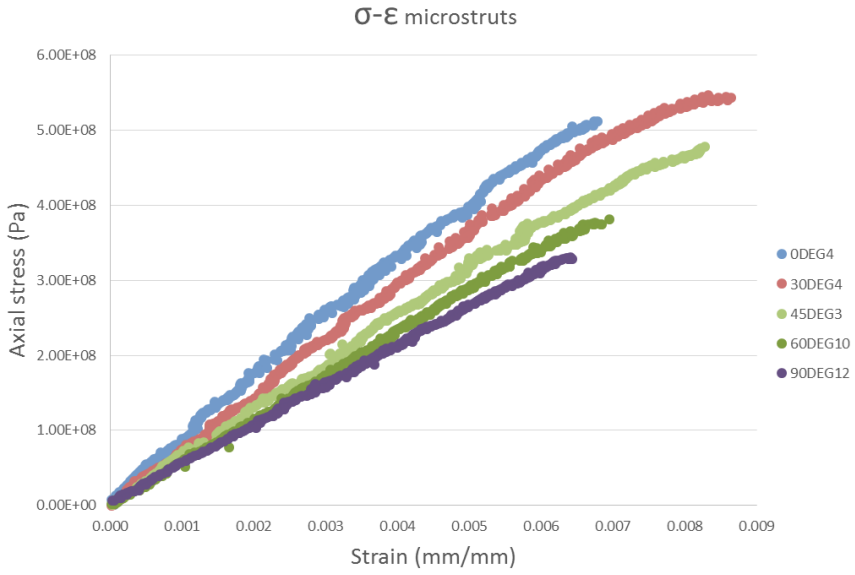

Figure 3.21 DIC linear stress-strain curves of 0°, 30°, 45°, 60° and 90° microstruts (top to bottom).

The determination of the properties was derived from averaging specimens (Table 3.1). It is important that although the few number of specimens to consider them a sample population, a variability of the properties was observed between microstruts fabricated in different batches, sharing the manufacturing chamber with other different components (Figure 4.3), thus with different thermal gradients that, as previously mentioned, can alter their microstructure and strengths in different manners. This variability is addressed in more detail in Chapter 4, highlighting the larger sensitivity of small components to thermal gradients, and thus the importance of considering it during the fabrication of components. In addition, this substantial variation of the properties sets the context for the observed errors of the results from the FEMs presented in Chapter 5 .

Table 3.1 Strength of microstruts.

Strength of microstruts (MPa)						
count	Orient.	Std.Dev.	Avg.	C.O.V.	max	min
7	0°	233.3725	744.2121	0.314	1025.141	511.875
8	30°	109.3798	562.0859	0.195	738.7031	483.1719
3	45°	16.69652	497.6563	0.034	509.3281	478.5313
14	60°	73.25843	480.558	0.152	594.2344	381.2969
14	90°	131.4335	371.9579	0.353	602.875	185.1406

3.4 Compression Test of EBM Ti-6Al-4V Cellular Lattices

For the evaluation of the performance of EBM cellular Ti-6Al-4V cellular metals, two different designs of lattices were subjected to uniaxial compression tests. Additionally to explore the mechanical properties of these two configurations of cellular metal, this testing was set to compare with the finite element models. As no standard was found specifically addressing compression tests on cellular metal lattices, the apparatus and procedures are as close as possible in accordance to ASTM E9.

3.4.1 Specimens

The lattices for experimentation were formed by 0.8mm x 0.8mm square-section microstruts in hexagonal (HEX) and reentrant hexagonal (REHEX) unit-cell configurations. As one of the most important properties, the relative density was explored in three variants resulting from selecting unit-cell sizes of 5mm, 6mm and 7mm, without modifying any other parameter. As a result, three lattice specimens of each unit-cell size, of each unit-cell configuration, were fabricated for a total of 18 specimens. For symmetry and reduction of free edge effects, the lattices were fabricated in arrangements of 5 x 5 x 5unit-cells (Figure 3.22). The lattices were fabricated with monolithic top and bottom 1mm plates for proper load distribution and avoiding damaging

the compression platens during tests. The average relative densities in g/cm^3, excluding the plates, are shown in Table 3.2.

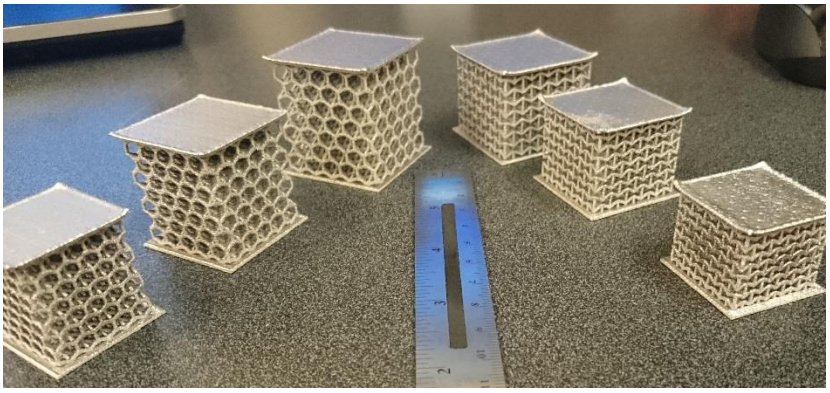

Figure 3.22 Hexagonal (left) and reentrant hexagonal (right) lattices with 7mm, 6mm and 5mm unit-cell size (back to front). Three of each specimens shown were fabricated and tested.

3.4.2 Apparatus

The lattices specimens were tested in an MTS Landmark 370 servo-hydraulic test system with an installed load cell capacity of 100kN, equipped with MTS 643.15B-01 compression platens with spherical seat and etched centering rings. Strain was measured using DIC system and VIC-gauge software, both from Correlated Solutions (Figure 3.23).

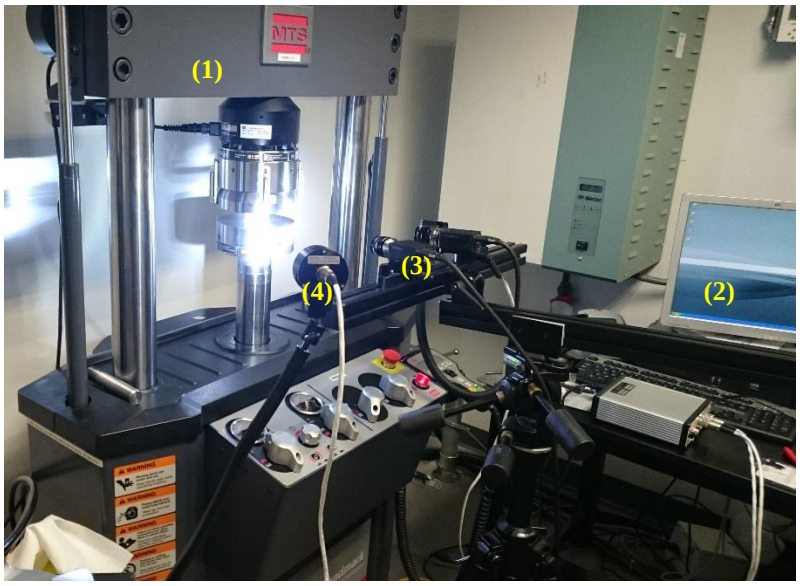

Figure 3.23 MTS Landmark 370 (1); MTS control (2); cameras (3); LED spotlights (4).

3.4.3 Procedure

Before testing, the plates of the specimens were carefully grinded at low speeds with silicon carbide sand paper up to #800 and generous amount of water, for a smooth contact interface with the compression platens. The specimens were carefully centered and aligned aided by the etched centering rings on the platens. A lithium complex additive lubricant was applied to all contact surfaces. The axial and cross-sectional strains were measured by DIC virtual extensometers using Vic-gauge for the whole lattice and an individual cell at the center of each specimen (Figure 3.24). As previously mentioned, DIC records displacements only between two previously specified points, or regions, of interest within the specimen imaging, thus, if any strain may occur due the monolithic plates, contact, or any other disturbance, it would not be recorded. Noteworthy was the advantage of using DIC for strain measurements in specimens with complex geometries, however the strains can only be measured at the visible surfaces, therefore prohibiting the strain measurement in the internal unit-cells. Testing was controlled by crosshead speed equivalent to a strain rate of 0.003mm/mm·min.

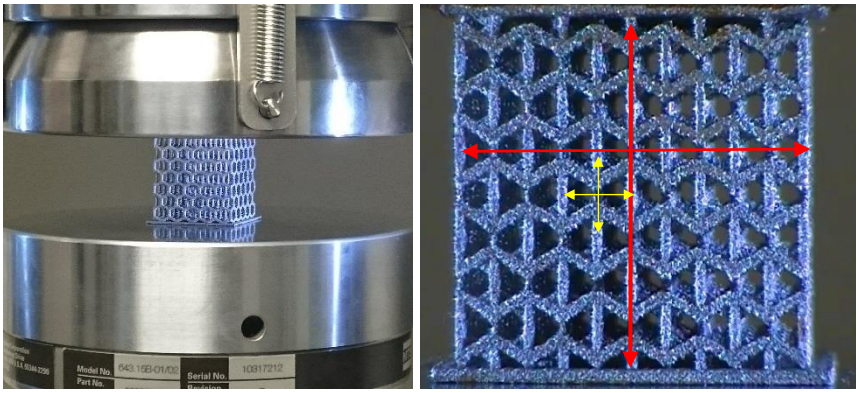

Figure 3.24 Setup of specimen (5mm HEX, left) and virtual extensometers (6mm REHEX, right).

3.4.4 Results

The stress-strain curves of both unit-cell variants were characterized by an initial linear stage with elastic moduli, much lower than those previously observed for bulk Ti-6Al-4V. Higher elastic moduli were observed for smaller unit-cells, thus manifesting the specific density as one mechanism to influencing the stiffness of the lattices. Whereas the reentrant hexagonal lattices displayed short to almost null nonlinear stages toward failure, the hexagonal lattices presented a substantially noticeable nonlinearity after a smooth transition from the initial stage, indicating that this unit-cell configuration may be preferable than the reentrant hexagonal, for energy absorption applications (Figure 3.25).

Figure 3.25 Stress-strain curves of hexagonal (top) and reentrant hexagonal lattices with different unit-cell size.

The specific strength and modulus, average of three specimens, were found increasing for higher densities; these two parameters compare how much strength and stiffness per mass, respectively, these cellular metals possess (Table 3.2). Therefore, materials with high specific strengths produce stronger structures with less mass, whereas materials with high specific modulus

are more suitable for stiffer, lighter structures. The comparison of these two parameters between the two unit-cell configurations was reserved given that the difference in density between the two unit-cell configurations results from a different spatial accommodation of the same number of microstruts, thus, the same amount of mass, but in a different cellular volume.

Table 3.2 Compressive properties of lattices. The mass of monolithic plates is excluded.

Lattice	ρ* *(gr/cm3)*	E *(GPa)*	Ultimate Strength *(kPa)*	Specific Strength *(kN*m/kg)*	Specific Modulus *E6(m2/s2)*
5mm HEX, 0.8mm strut	0.800	2.672	40,000	50.000	3.340
6mm HEX, 0.8mm strut	0.600	0.943	21,000	35.000	1.572
7mm HEX, 0.8mm strut	0.470	0.795	15,000	31.915	1.691
5mm RE-HEX, 0.8mm strut	1.130	1.500	35,000	30.973	1.327
6mm RE-HEX, 0.8mm strut	0.820	1.042	21,000	25.610	1.271
7mm RE-HEX, 0.8mm strut	0.650	0.786	13,000	20.000	1.209

Chapter 4: Multiscale Analysis of Cellular Solids Fabricated by EBM

The previous chapter presented the testing of different samples with the sole objective to determining the general mechanical properties of the material at different orientations, and different conditions. The data generated from measuring the mechanical properties may be enough to developing and evaluating a finite element model, but the understanding of the performance of the cellular Ti-6Al-4V might still be limited, and possibly narrowing the judgment when evaluating the computational mechanics. Thus, this chapter presents the multiscale analysis (Figure 4.1) of different factors found influencing the performance of the investigated cellular Ti-6Al-4V, as proposed in Chapter 2.

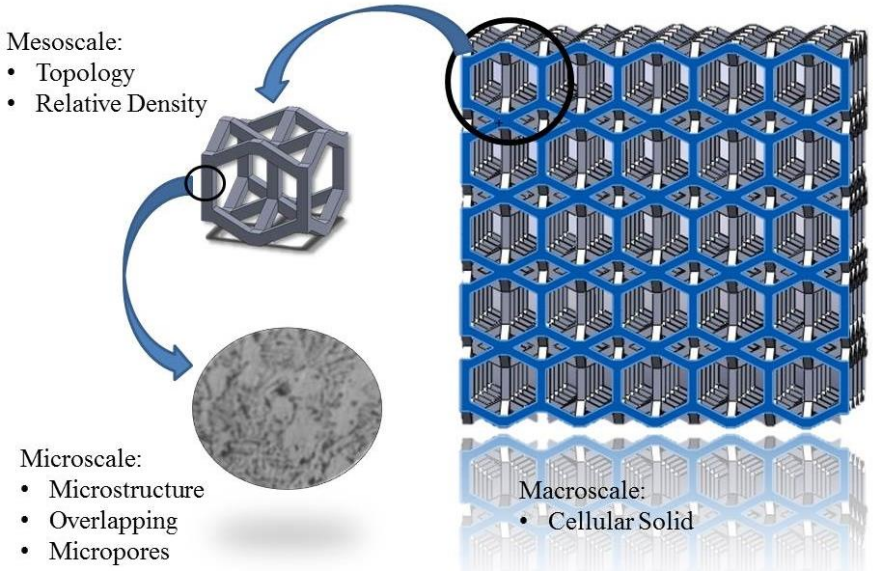

Figure 4.1 Scale levels for the analysis of cellular solids

4.1 Microscale

Some factors at the microscale level, such as manufacturing technology, file format and the constituent solid, are often subjected to availability. For example, access to a variety of expensive systems such as SLM or EBM can be difficult; nowadays, the .STL file format can be

considered almost universal for AM systems; and the use of a different powder metal implies cleaning up and resetting an active manufacturing system.

In this manner, from CAD designs exported to .STL format, the components studied herein were fabricated using Arcam AB Ti-6Al-4V prealloyed precursor powder with spherical particle size distribution from 40-100µm (Figure 2.3), in an Arcam A2 (EBM) system. Among the preferences in this study to using EBM and Ti-6Al-4V were, that components fabricated by EBM normally display lower residual stresses compared to SLM, this because of the preheating of the precursor in EBM; and the allotropy of titanium (L. E. Murr et al. 2009; Luca Facchini et al. 2010).

4.1.1 Manufacturing Parameters

The standard parameters are unique for each EBM system and have to be previously investigated during the first time system set-up. Thus, the standard parameters in the Arcam A2 system, that fabricated the components, consisted of a preheat step taking place to maintain the fabrication environment at approximately half of the material's melting point (~700-760°C for Ti-6Al-4V). Powder within the fabrication environment is deposited using a raking mechanism and selectively melted using a current of 18mA max with beam speeds of 500-1,000mm/s. The process takes place in a high vacuum environment of up to 10-4mBar and repeated layer-by-layer from the preheat step until fabrication is complete.

Heating focus offset relates to the energy density and diameter of the beam; larger focus offsets refer to wider diameters with less dense energy, and shallow heating/melting effects, which can result in defects from unmelted particles. *Focus offset* is any supplementary current though the electromagnetic lens that can be transferred into an offset in the focal plane (Jan Schwerdtfeger, Robert F. Singer, and Carolin Körner 2012).

Additionally to the following settings. For the first preheat step, a focus offset of 25mA and a heating focus offset of 130mA were set; whereas for the second preheating step, a focus offset of 50mA and a heating focus offset of 100mA were selected. For the melting stage, the

parameters were as follows: surface temperature of 850°C, minimum current of 12mA, max current increment of 0.5mA, and 4530mm/s beam speed. As previously mentioned, these settings were previously investigated to obtain commercial components with uniformly distributed microstructures. The optical micrographs of the specimens revealed a microstructure with no visible features due to the layering fabrication and a bi-modal uniform distribution of α and β-phase titanium (Figure 4.2).

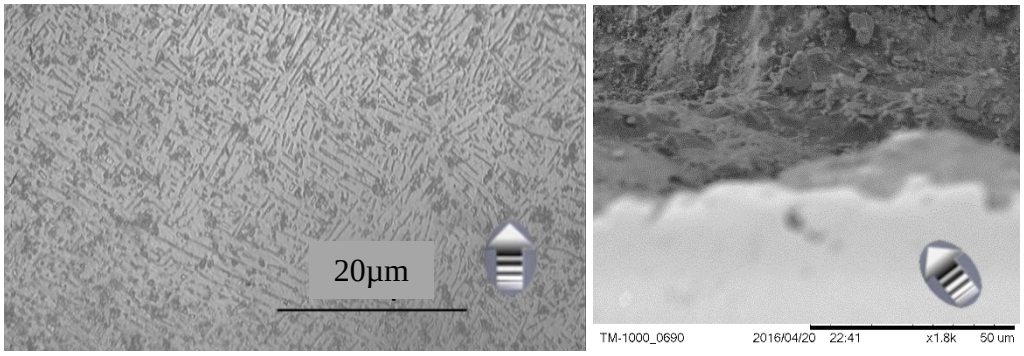

Figure 4.2 Bi-modal microstructure uniformly distributed acicular, α-phase (HCP) surrounded by β-phase (BCC) (dark) in Ti-6Al-4V cylindrical rods at 90° (left). Fracture surface at perspective displaying ductile features such a prominent crest and dimples; 50µm scale mark (right)

4.1.2 Manufacturing Process

As discussed in Chapter 2, the *Manufacturing process* contemplates all those aspects mainly from preferred practices of the manufacturers (e.g. location and orientation of components in the manufacturing chamber)

As a result of the different material densities, and thermal gradients, constantly created throughout the manufacturing space, the building strategies considering the spatial position, and the orientation and number of builds being fabricated, can also alter the microstructure. This effect is more noticeable in bodies with a large area to volume ratio such as the case of the microstruts fabricated individually. Although individual microstruts for tension tests were fabricated from the

same CAD file and manufacturing settings, the strength of the microstruts displayed some variability between batches, suggesting their higher sensibility to the thermal gradients due to the different layout of the components and its location within the manufacturing space (Figure 4.3).

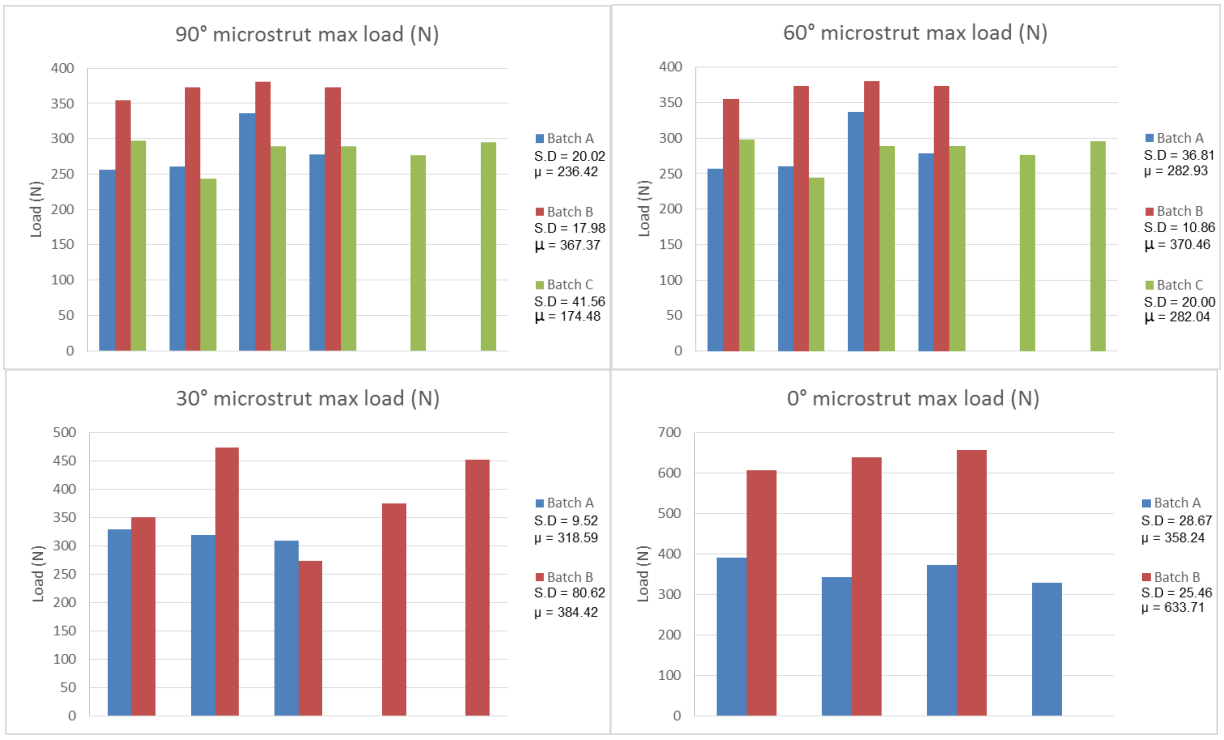

Figure 4.3 Strength variability between batches of microstruts with different orientations.

As a consequence of the layering building process in EBM, the quality of the microstrut surface is affected to great extent by the layer thickness and the build angle (Figure 4.4), threatening its integrity as the area of the microstrut decreases and the slenderness ratio is increased. Therefore, it is important to pay especial attention to the location of components sensitive to manufacturing orientation and thermal stresses when optimizing the manufacturing space in the chamber in addition to the layer thickness analyzed as a manufacturing setting.

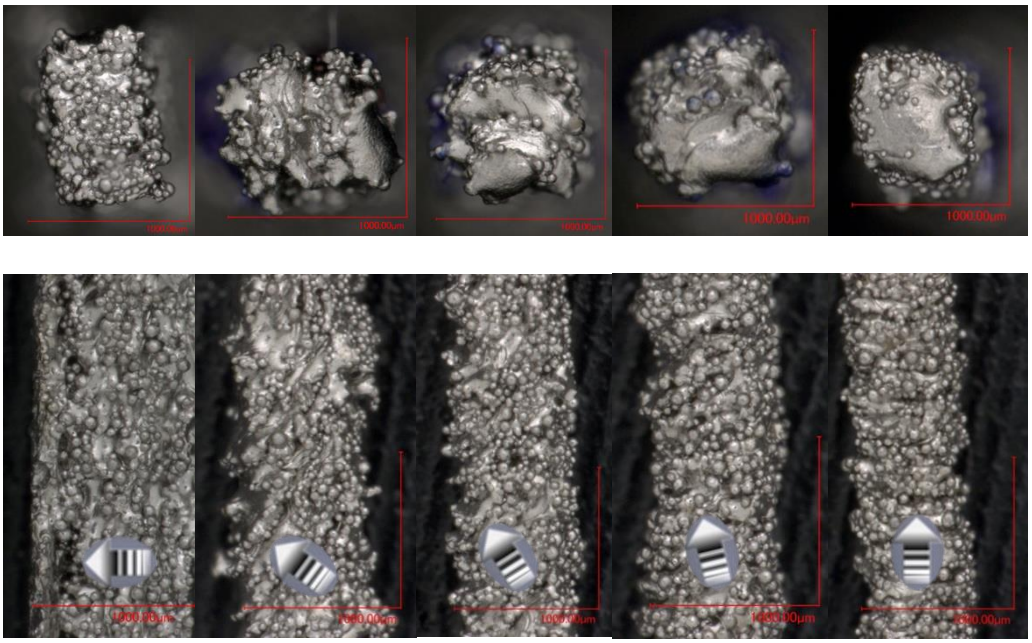

Figure 4.4 From left to right: 0°, 30°, 45°, 60° and 90° microstruts top and lateral-right views displaying layering striations with partially melted particles.

Whereas the microstructure in the standard tension test specimens was shown uniform with no trace of the interface between layers (Figure 4.2), the failure profiles of four orientations studied presented different failure modes. Those specimens with symmetrical layering with respect to the axial loading direction failed similarly. The fracture features such as a slight necking, shear lips, and failure planes normal to the main applied stress are well defined and characteristic of a flat-face failure mode, produced by a triaxial stress system. Whereas in the profiles of the specimens fabricated at 30° and 60°, the fracture features in the profile were not defined with the same clarity, possibly indicating some shear effect (Figure 4.5). Although the uniformity in the microstructure suggested that the interface between layers does not represent a major source of shear strains, because of material phases oriented differently in it, for the 30° and 60° specimens, the presence of oriented flaws (Figure 4.6) could develop stress concentrations with orientations other than the principal stress, leading to the shear strains that the failure profiles suggest. Again, a reminder that the spatial location and orientation of the components might result in favorable, or unfavorable performances, according to the intended application of the component.

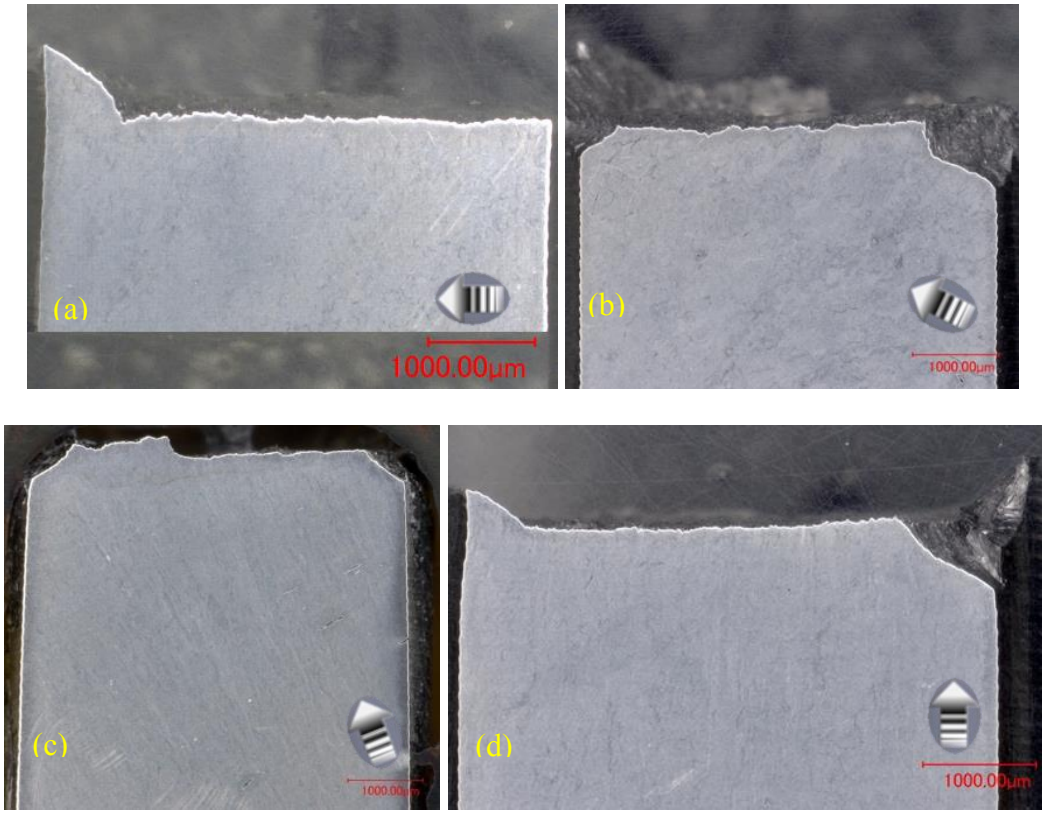

Figure 4.5 Failure profiles of 0°, 30°, 60°, 90° (a, b, c, d respectively) standard tension specimens displaying necking and shear lips for 0° and 90°. 1mm scale marks.

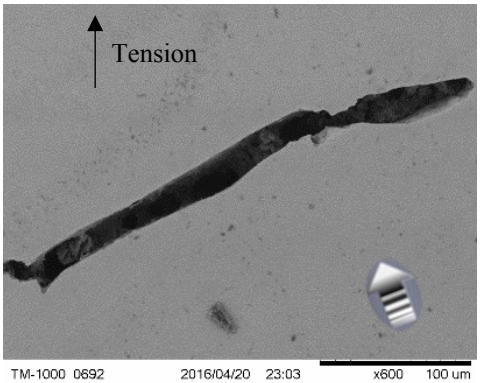

Figure 4.6 Flaw in a 60° standard tension test specimen. 100µm scale mark.

The *manufacturing settings* and *manufacturing process* can be managed to develop specific, localized behaviors, as well as convenient failure modes that could be advantageous for the performance of AM components over those traditionally fabricated. Thus, in an experiment with one of the tension test specimens from the *ASTM E8* STANDARD TENSION TEST OF EBM TI-6AL-4V tests in *Chapter 3*, it was possible to eliminate the plastic region; exhibiting the possibility to fabricate very similar Ti-6Al-4V components with similar strengths but displaying dissimilar performances: two (60deg12 and 60deg13) with long plastic regions, and another emulating a purely brittle material failure, like glass (60deg99) (Figure 4.7). The brittle-like failure with similar strength was made possible in the component by interrupting its building process, noteworthy is the ability to localize the fracture along the component by stopping the process (Mireles 2016). The fractography of the specimen revealed a mixture of ductile and brittle features in the same fracture surface (Figure 4.8). The weaker bonds between sintered powder particles originated the brittle features, resulting in an induced lower toughness, and yield strength; however, toughness was drastically reduced, compared to the yield strength.

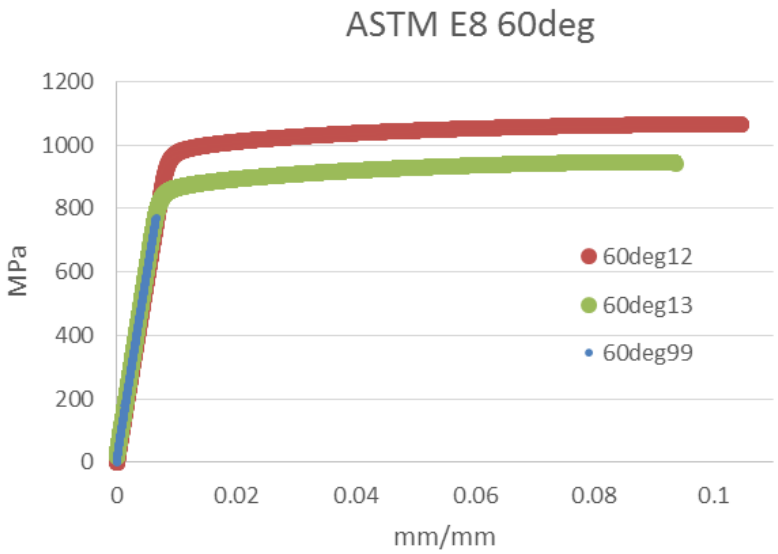

Specimen	Yield Strenght (MPa)	Toughness (MJ/m^3)
60deg12	990	100
60deg13	870	80
60deg99	770	2.5

Figure 4.7 Stress-strain of 60° tensile specimens. 60deg99 representing the specimen with an interrupted building.

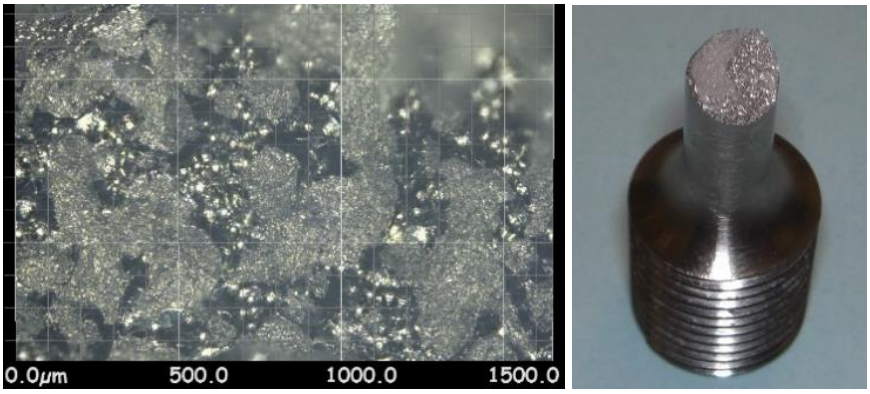

Figure 4.8 Fractography with mixed ductile and brittle features in a tensile specimen with the interrupted building process; 500µm scale grid (left). Failed specimen (right)

The lower variability of the compressive strength compared to the tensile strength of specimens is an indicator of the larger sensitivity of the metal to flaws and defects, under tension (Figure 4.9 and Figure 4.10); this could be explained by the stress alleviation mechanism over the internal surfaces in the flaw when the gap closes due compression, compared to the stress concentration at the sharp ends of the flaw when loaded under tension (Figure 4.11). The comparably similar average strength under tension and compression supports the assumption made about similar tensile and compressive behaviors of the Ti-6Al-4V, when obtaining the response from testing individual microstruts for the characterization of lattices. The buckling and eccentricities developed in the microstruts in the cellular metal may be addressed as geometric features under the mesoscale.

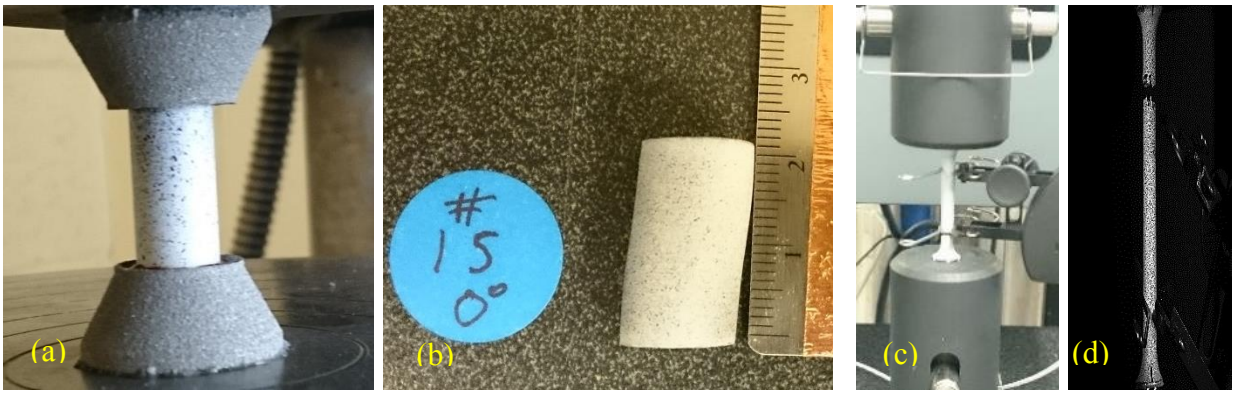

Figure 4.9 Setup and failed specimens under compression and tension (a, b and c, d).

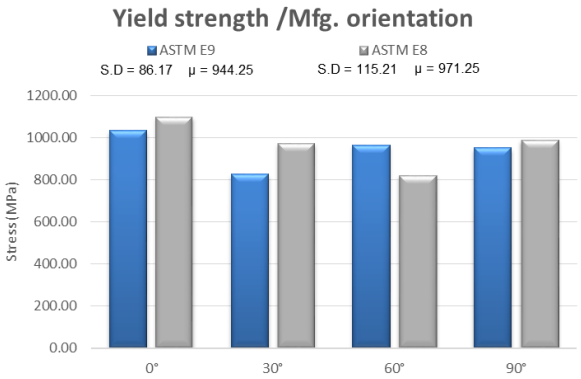

Figure 4.10 Average and standard deviation of tensile and compressive yield strengths on specimens at different orientations.

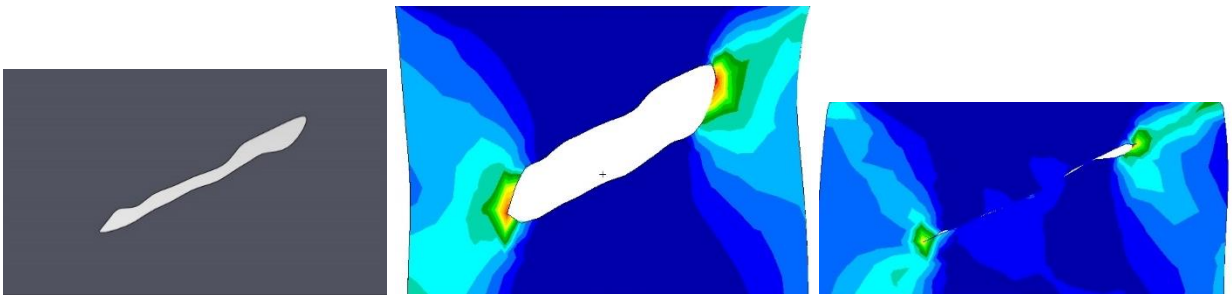

Figure 4.11 FEM of a flaw (left). Under tension, plastic strain concentrates at the ends of the flaw until rupture (center). Under compression, the relief of plastic zones after the gap closes and stress redistributes along the gap (right).

4.1.3 Degradation of the Mechanical Properties

The small cross-sectional areas in the microstruts demonstrate the sensitivity of its tensile elastic modulus to the manufacturing orientation (Figure 4.12). In addition, smaller cross-sections result in microstruts with higher slenderness ratios, and thus, more susceptible for elastic buckling failure, under compression. If the degradation of the elastic modulus is considered to be attributable only to the reduction of the cross-sectional area along the microstruts, resulting from the step-like features, the effective cross-section area is estimated to be approximately 75% of the

nominal area (0.8mm x 0.8mm), thus an indirect measurement of area is suggested for small components. Counterintuitive to the assumption that lower build angles result in smaller layer overlaps, diminishing the effective cross-section, the microstruts fabricated at low angles showed to be stiffer under axial tensile test (Figure 4.13). This can be explained by the consistent larger cross-section of the 0° microstruts, and the layers overlapping all along themselves, parallel to the load. In the 90° microstruts, the layers are stacked perpendicular to the load, thus a triaxial stress state is rapidly developed in planes weakened by flaws and surface imperfections reducing the effective area and resulting in lower strengths. Whereas on the 30° and 60° microstruts, the loading is alleviated by principal stresses, but also by shear stresses potentially developed from rotational deformations of each layer due to the asymmetry of the surface stress concentrators, eccentricity and loading being transferred oblique to the overlaps, where the weakest plane most likely exists (Figure 4.14 and Figure 4.4).

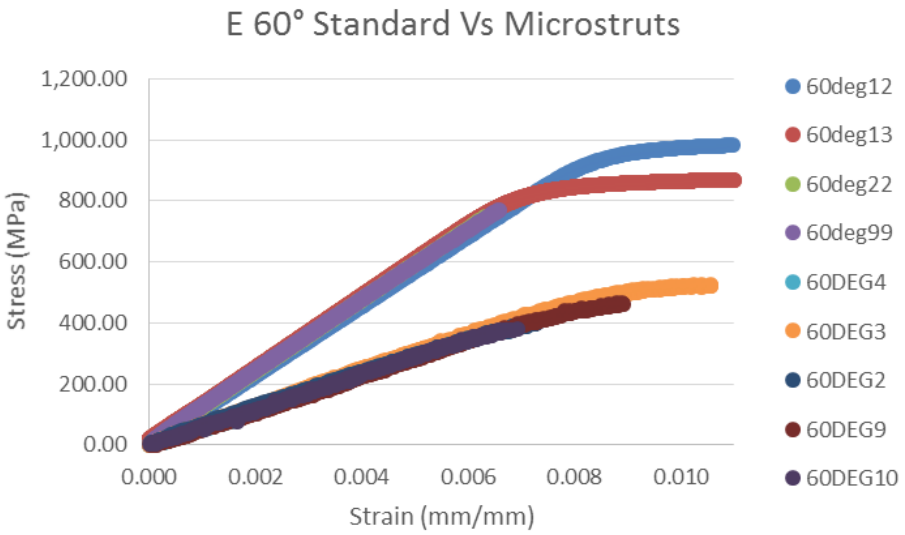

Figure 4.12 The elastic modulus of 60° Ti-6Al-4V calculated for 0.8mm x 0.8mm microstruts is over 25% lower than that for the standard tension test specimens (116Gpa approx).

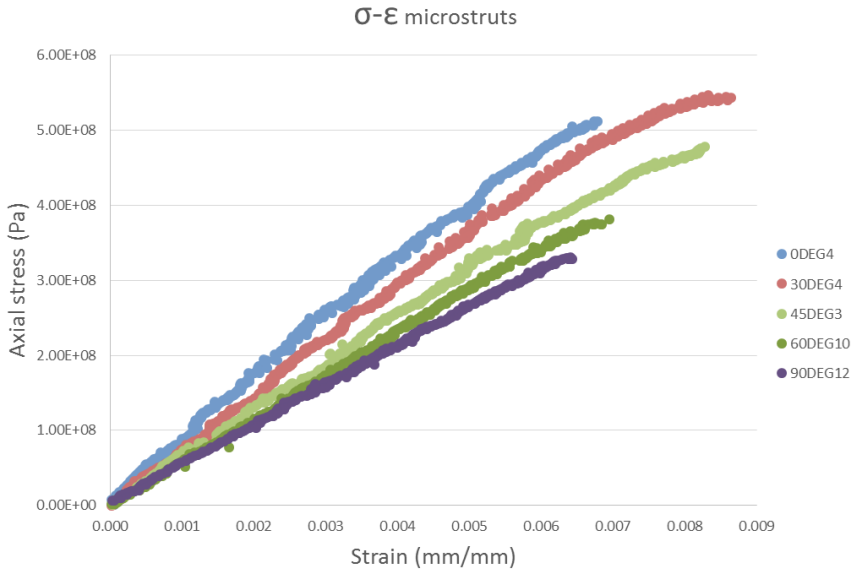

Figure 4.13 Stress-strain curve of 0°, 30°, 45°, 60° and 90° microstruts. Microstruts fabricated at lower build angles showed to be stiffer and stronger. All orientations observed a practically linear response.

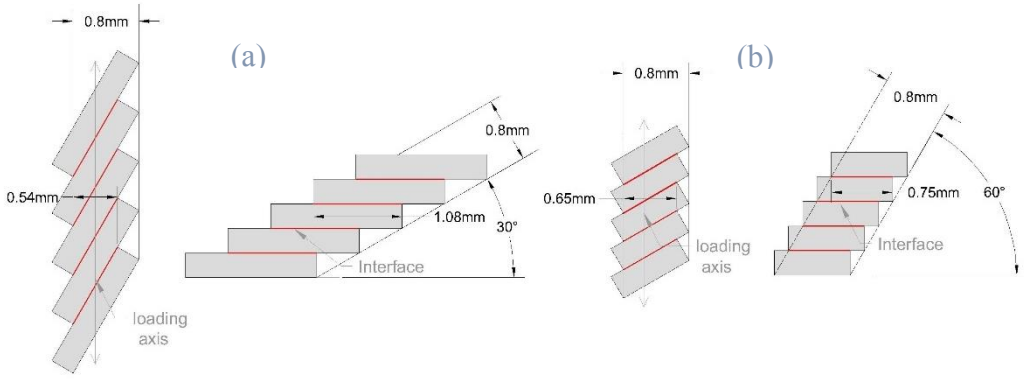

Figure 4.14 Representation of 30° (a) and 60° (b) microstruts. Conceptually, with a layer thickness of 0.3mm, the effective cross-section widths are 0.54mm and 0.65mm for the 30° and 60° microstruts when loaded axially.

4.2 Mesoscale

At mesoscale, stochasticity, the nested hierarchical levels, and the aspect ratio may not need further analysis than to mention the preferred selection for the lattices investigated. Thus,

lattices with a single hierarchical level and aspect ratio of 1:1:1 are presented in this study given their more uniform collapse and higher resistance to defects, compared to foams.

4.2.1 Maxwell Stability Criterion

The decision in selecting the hexagonal and reentrant hexagonal polyhedron shapes as unit-cells for the design of the lattices being investigated is based on the understanding that hexagons are among the simplest symmetric shapes that deform as mechanism, as defined by the Maxwell stability criterion. In exemplifying how geometrical features can produce beneficial behaviors, the reentrant hexagons were selected to creating cellular metals with auxetic behavior, which, as described in *Auxetics* in *Chapter 2*, are expected to display superior behavior for torsion, bending stiffness and energy absorption, with the same amount of material, the same Maxwell stability value, but different geometrical arrangement. The *necessary* Maxwell stability criterion for the both unit-cells herein investiged is M = -19 (b = 29, j = 18) (Figure 4.15).

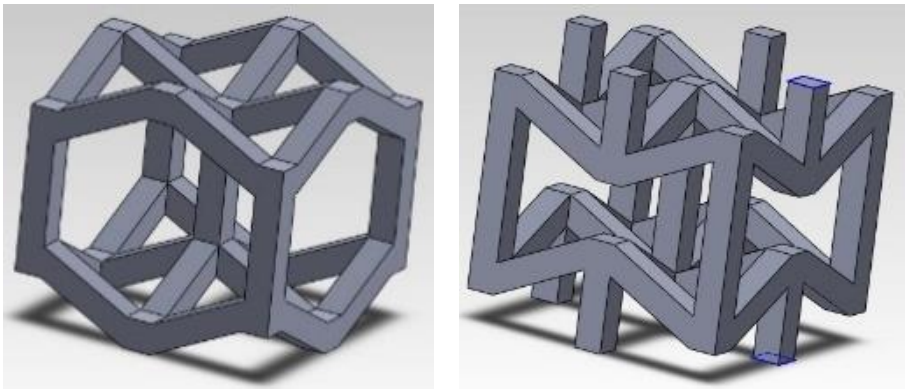

Figure 4.15 Examples of mechanistic unit-cells (M<0).

Individual testing of microstruts displayed linear responses with practically null plasticity (Figure 4.13), thus, we could expect the response of the unit-cell to be also linear. However, because of the principles of the mechanistic deformation derived by Maxwell, the response of the hexagonal unit-cell displaying non-linear behavior can be explained. In this manner, aided by DIC, a stress-strain curve was obtained by measuring the strain of a single load cell at the center of the

lattice, with a proportional point load of P/100 (P = total load on the lattice), corresponding to the outside face of the examined unit-cell (Figure 4.16); the recordings from testing displayed a non-linear response, best described by a parabola, according to the high R-value shown (Figure 4.17).

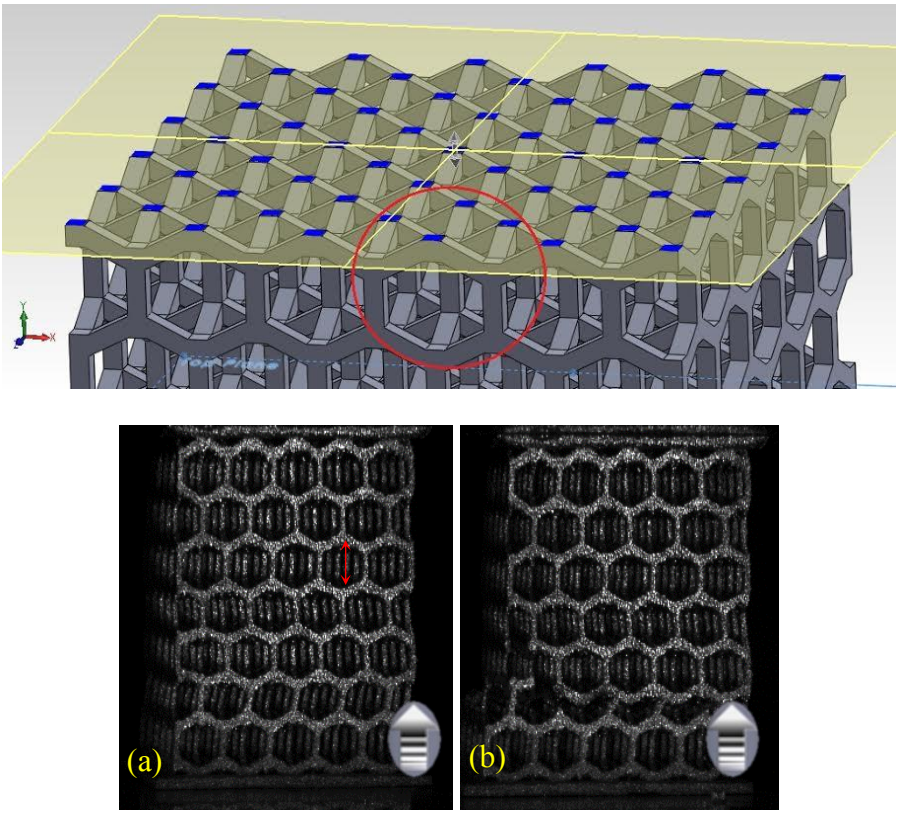

Figure 4.16 Cut-section of the lattice model highlighting the measured unit-cell and the bearing points where the load is transferred between unit-cells levels (Top). DIC images of 5mm hexagonal lattice: an instant before fracture (a) and after fracture (b). The double arrow at (a) indicates the location of the virtual extensometer.

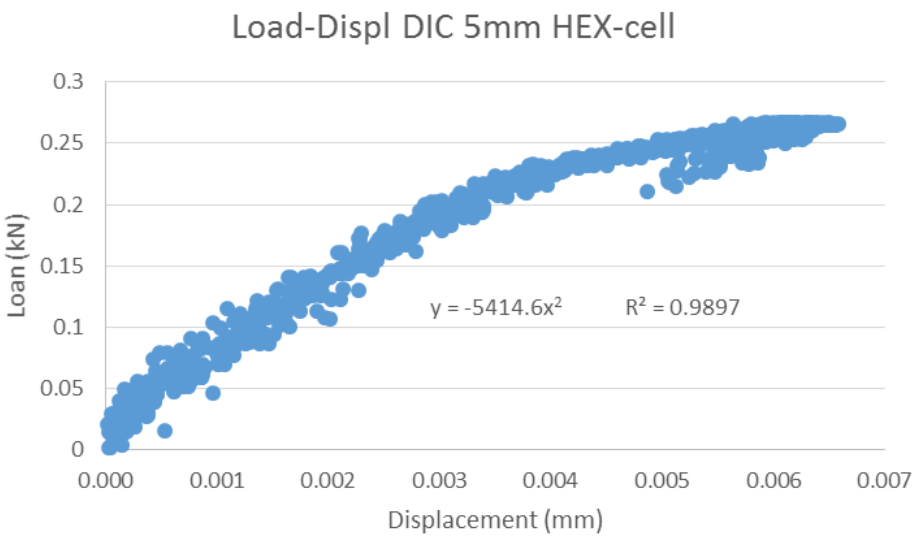

Figure 4.17 Nonlinear stress-strain curve of a single 5mm hexagonal unit-cell during the compression test on the lattice.

4.2.2 Auxetics

A reentrant hexagonal unit-cell was selected to analyze the negative Poisson's effect of metals lattices (Figure 4.18). During the compression test of 5mm reentrant hexagonal lattices, the axial and transverse strains were measured via DIC from an external unit-cell. The recordings displayed a linear negative Poisson's ratio of 0.21; a second nonlinear transition zone from positive to negative; and a third and final linear segment before with a positive Poisson's ratio of 0.06 before fracturing (Figure 4.19). In response to this individual behavior, the auxetic lattices described a line with positive and negative slopes when plotting its Poisson's ratio against the applied compressive stress during testing (Figure 4.20).

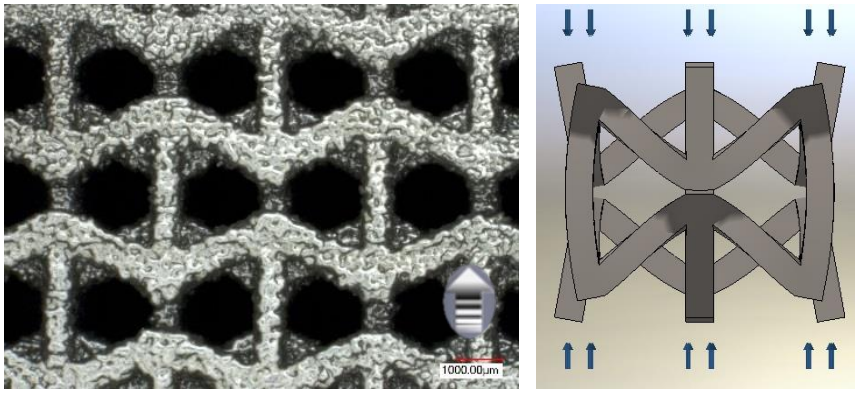

Figure 4.18 5mm reentrant hexagonal unit-cell (left) and FEM of a single unit-cell displaying negative Poisson's effect. 1mm scale mark.

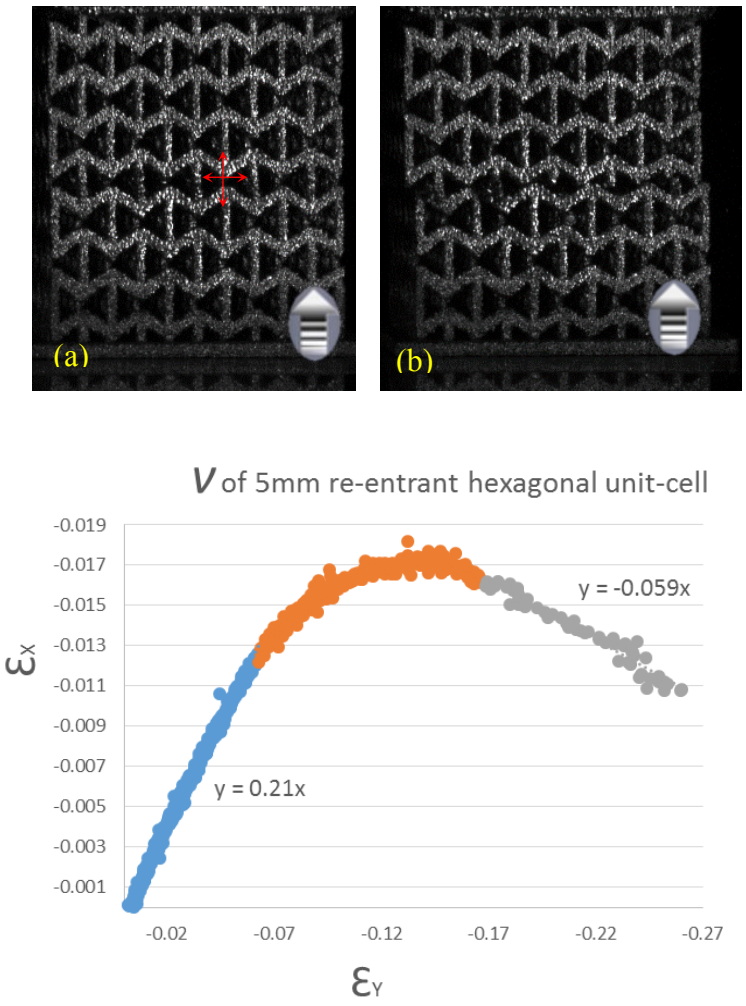

Figure 4.19 DIC images of a 5mm reentrant hexagonal lattice: an instant before fracture (a) and after fracture (b). The double arrows at (a) indicate the location of the axial and transverse virtual extensometers (Top). Measured Poisson's ration at the unit-cell indicated by the extensometers.

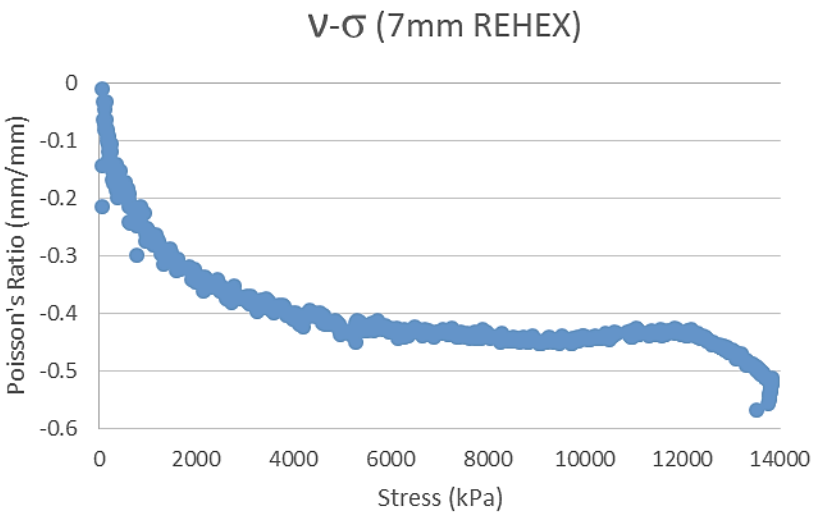

Figure 4.20 Poisson's ratio of a reentrant hexagonal lattice (7mm) during compression.

4.2.3 Relative Density

The relative density of the lattices being analyzed was defined by modifying the cubic size of it unit-cells only. In accordance with the Gibson-Ashby relationship, the denser lattices displayed higher strengths. The selected sizes of the unit-cells were 5mm, 6mm, and 7mm (Figure 4.21 and Figure 4.26).

Lattice	ρ* (gr/cm3)	Ult. Strength (kPa)
5mm HEX, 0.8mm strut	0.800	40,000
6mm HEX, 0.8mm strut	0.6	21,000
7mm HEX, 0.8mm strut	0.470	15,000
5mm RE-HEX, 0.8mm strut	1.130	35,000
6mm RE-HEX, 0.8mm strut	0.82	21,000
7mm RE-HEX, 0.8mm strut	0.65	13,000

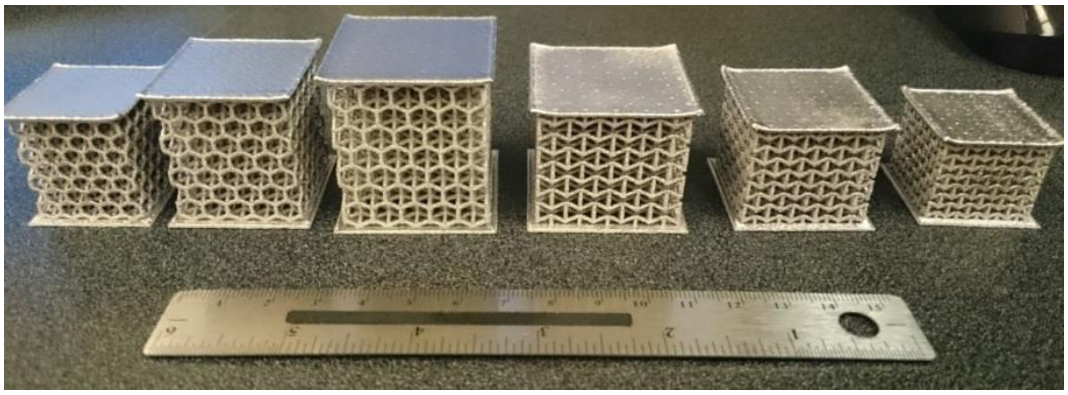

Figure 4.21 Ultimate compressive strength and specific density (top) of the EBM cellular Ti-6Al-4Vspecimens (bottom).

4.3 Macroscale

As previously mentioned, at this scale the analysis of the response of the cellular metal can be used to understand specific behaviors, their possible causes, and alternatives to manipulate them to obtain a desired response. Regarding the orientation of the lattices presented, the XY plane was defined by the monolithic bearing plate at the bottom, and fabricated in the Z direction; thus, this orientation, whose layering is perpendicular to the compressive loading, is presumed to favor larger deformations than that with layering parallel to the loading.

4.3.1 Deformation Mode

As previously discussed in Chapter 2, lattices formed by axially-dominated unit-cells ($M \geq 0$) are normally stiffer with higher yield strengths, but collapse abruptly, when compared to

bending-dominated lattices (M<0). Thus stretch-dominated lattices are, in general, stronger and lighter than the bending-dominated, however, because its progressive collapse at a nearly constant stress, these typically are better performers for energy absorption purposes.

The deformation mode of a lattice is a result from a combination of different factors. For example, axially-dominated unit-cells formed by linearly-behaving microstruts made of a stiff precursor are expected to form strong and stiff lattices displaying linear responses. However, if only the unit-cell is changed to a bending-dominated, the response can display nonlinearities that can compensate for the lack of plasticity in the precursor, therefore, potentially increasing the area under the stress-strain curve (specific energy).

In that manner, during this investigation, the lattices formed by bending-dominated hexagonal unit-cells (M<0) composed by linearly-behaving microstruts made from Ti-6Al-4V displayed a nonlinear response. Noteworthy is that regardless of the linear response of the microstruts (Figure 4.13), the use of a bending-dominated unit-cell allowed to obtain a nonlinear response (Figure 4.17), which was amplified in the response of the lattice because of the number of unit-cells forming the lattice (Figure 4.22).

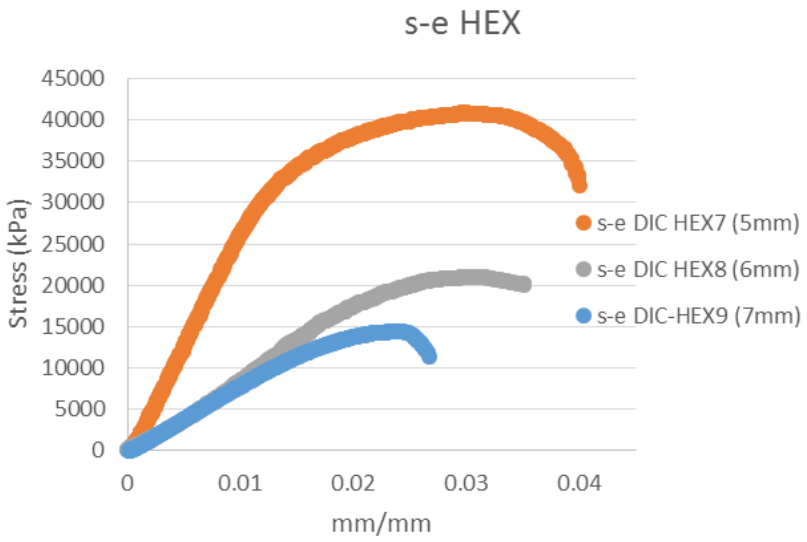

Figure 4.22 Compressive responses of hexagonal lattices with different unit-cell sizes.

4.3.2 Brittleness

As previously mentioned in Chapter 2, brittle constituent can be identified by several stress fluctuations, product of the microcracking developing in the collapsing stage of the lattice. Despite the efforts at the different scale levels to maximize the nonlinear behavior of the lattices, a close view into a segment of the nonlinear section of their stress-strain curves reveals remnants of brittleness from the Ti-6Al-4V (Figure 4.23).

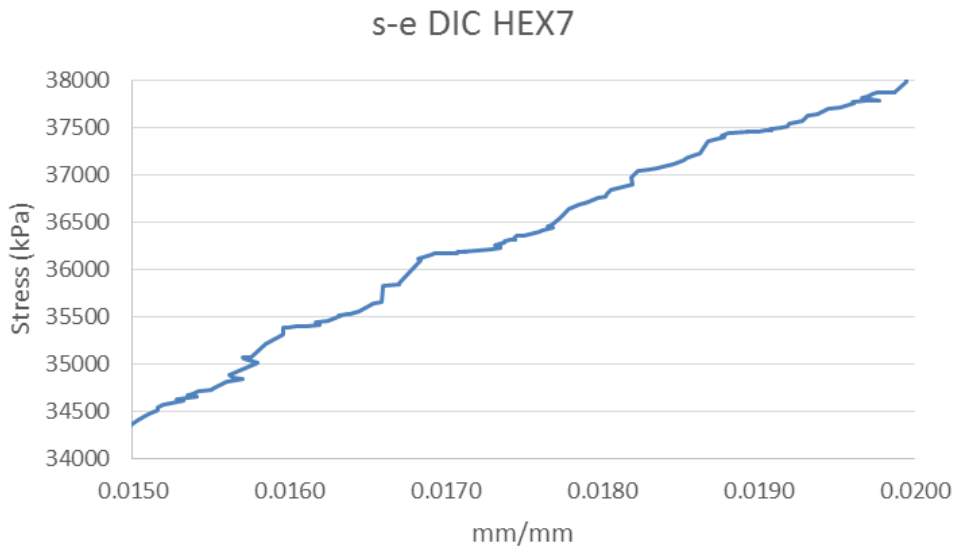

Figure 4.23 Stress fluctuations in a nonlinear segment of the response of a 5mm hexagonal lattice.

4.3.3 Recovery

The studied lattices presented an increasingly non-linear behavior as the unit-cell size decreased. Despite the microstructural and geometric design approaches that extended the deformation capability of the ductile-limited Ti-6Al-4V, the lattices failed catastrophically (Figure 4.27). The voids in the lattices were larger than the ultimate deformations from the microstruts, thus the stresses were not able to be relieved by contact between microstruts before fracturing. However, the strength recovering in the lattices of both configurations was perceived by the subsequent ultimate load of similar magnitude, supported by the next weakest unit-cells level. The

slight decrement of peak loads can be approximated by a constant slope, and can act as an indicator of accumulated damage, proportional to the loading history. This was observed in most, but not all of the lattices, a larger sample size will reduce the uncertainty and may confirm the trends of cumulative damage for all unit-cell sizes (Figure 4.24).

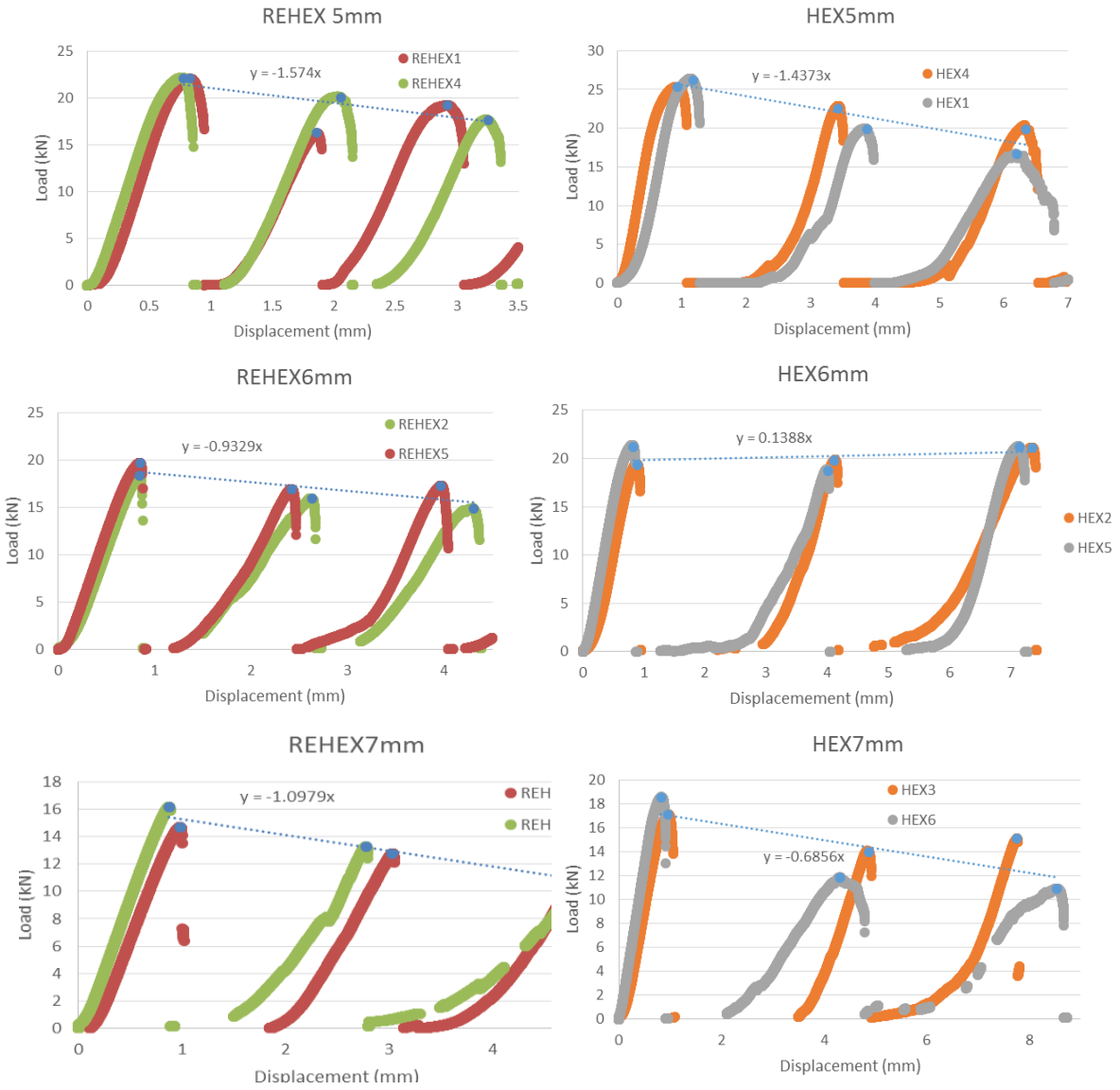

Figure 4.24 Progressive collapse of unit-cell levels in lattices displaying recovery and accumulated damage. Reentrant hexagonal lattices (left) and hexagonal lattices (right) at different unit-cell size.

4.3.4 Unit-cell Specifics

In general, during the experiments, the reentrant hexagonal lattices displayed very limited nonlinear behaviors, but they continued to follow the Gibson-Ashby relationship of higher strengths based on the same unit-cell at higher specific densities. However, it is important to note that although the density of the lattice was increased by the reentrant sides of the hexagon, the amount of solid precursor material is essentially the same when comparing unit-cells of the same size; therefore, when selecting the proper unit-cell geometry, the relative density should not necessarily be considered as a major contributor for specific energy (the area under the stress-strain curve) (Figure 4.25).

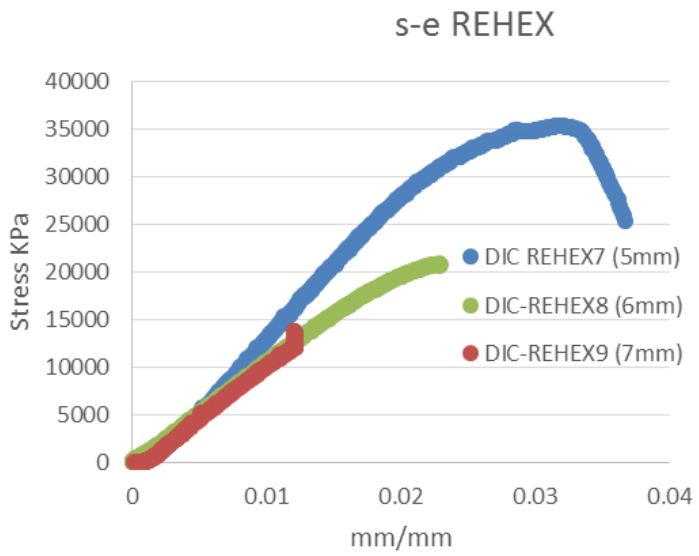

Figure 4.25 Compressive response of reentrant hexagonal lattices with different unit-cell sizes.

Experimental results from the compression tests revealed that the reentrant hexagonal lattices with large (6mm, 7mm) unit-cells were stiffer by approximately 10% and 25% respectively when compared to the hexagonal of the same size. The ultimate strength for both cell configurations was comparable within a 3%, however, the hexagonal lattices displayed considerably larger nonlinear strains. For the unit-cell size of 5mm, the previous observations were

reversed; the hexagonal lattice was stiffer and stronger than the reentrant hexagonal, however, their strains at failure were comparable within 10% (Figure 4.26). Turning into a purely geometrical approach, these results can be explained by reviewing how the load distributes throughout the structures: the reentrant hexagonal lattices develop a combined stress system of tension along the zigzagging microstruts and compression along the vertical microstruts, whereas the hexagonal lattices generate a purely compressive system. In a purely compressive system, the microstruts react as columns, thus as the unit-cell size increase, the unsupported length is also increased and critical instabilities are more likely arising, added to the larger number of elements under compression in hexagonal than in reentrant lattices.

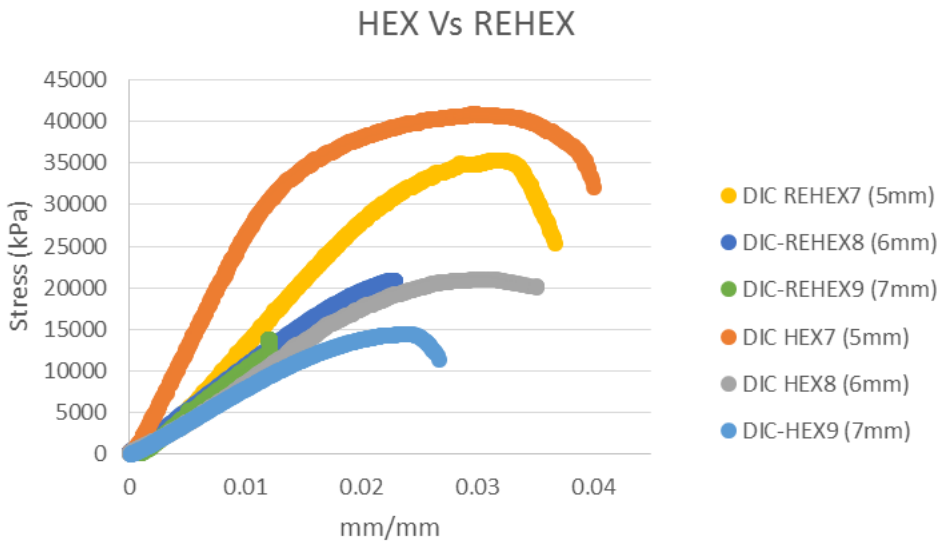

Figure 4.26 Stress-strain curves of hexagonal and reentrant hexagonal lattices at different unit-cell size.

Another interesting behavior of the auxetic structures is the capacity of confining the energy release during brittle failure. Despite the catastrophic brittle fracture, the reentrant hexagonal lattices imploded, maintaining the specimen in place; whereas an explosion was characteristic of the sudden energy release events in the hexagonal lattices (Figure 4.27).

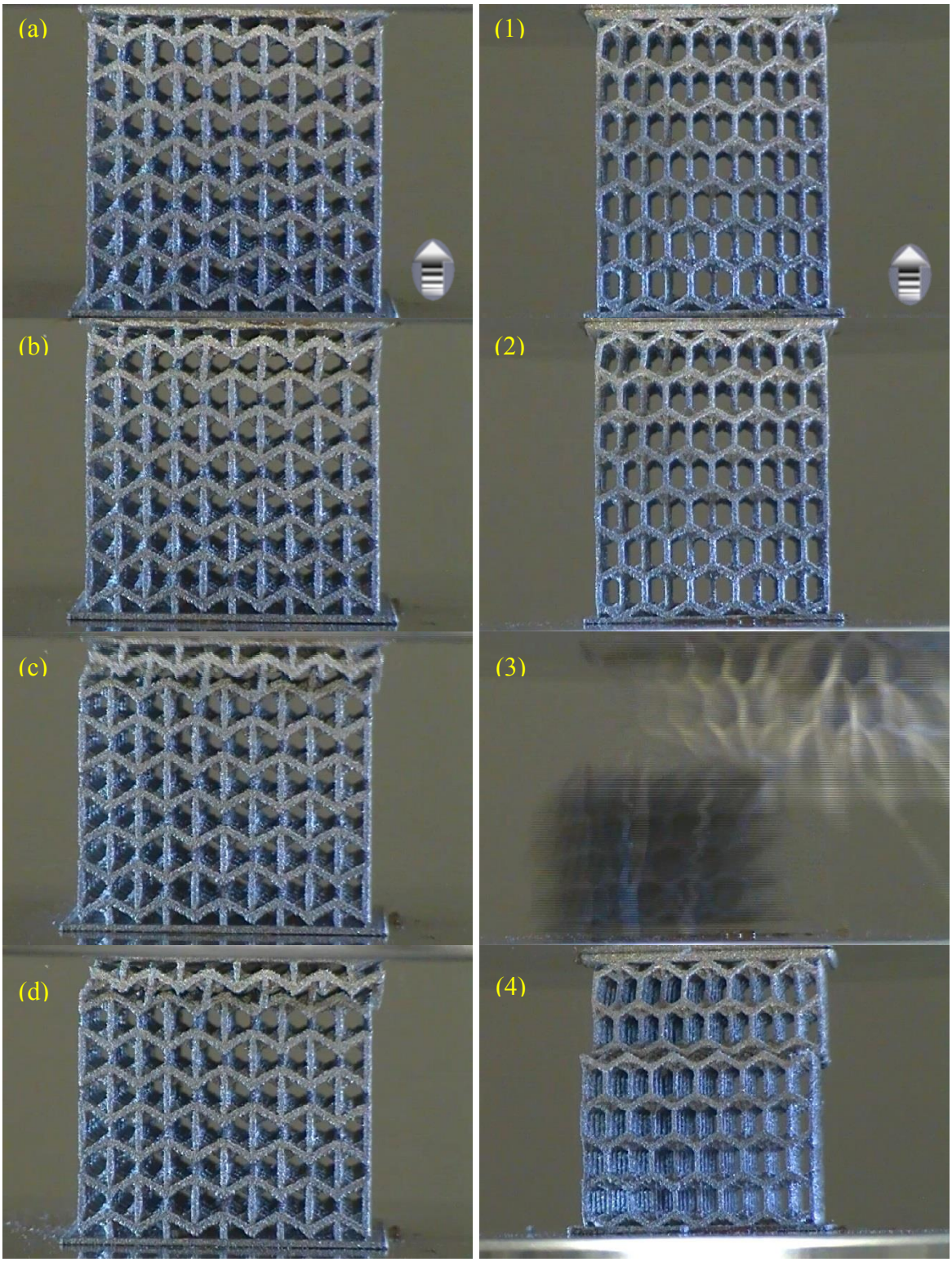

Figure 4.27 Comparison of lattices at different loading stages: unloaded (a, 1), an instant before failure (b, 2), the instant at failure (c, 3) and after failure (d, 4). The energy releasing events of the two unit-cell configurations totally opposite (c, 3). Images from video recordings at 29 frames/s.

The reentrant hexagonal designs were expected to display a two-stage response. After the initial behavior shown here and completing a first deformation stage, a jaw-like feature was intended to lock the deformed unit-cell (Figure 4.28a,b), creating a new nodal configuration and morphing the cell into four new, smaller, stiffer, and Poisson's-positive unit-cells, formed by four triangles each (Figure 4.28c) . It is important to note that these new unit-cells would neither comply with the Maxwell stability criterion to be defined as stretch dominated; this because of the square configuration of the four triangles arrangement from a top view (Figure 4.28d). However, given that the loading would be distributed on the planes of the triangles, the expected response would tend more toward rigid. Most of the presented lattices fractured before the jaw-like feature locked; the second stage of the response of these lattices could have been achieved by a design approach specifically aimed to enhance this as a required deformation, by means of any of the factors previously discussed, such as creating nodes richer in alpha phase titanium.

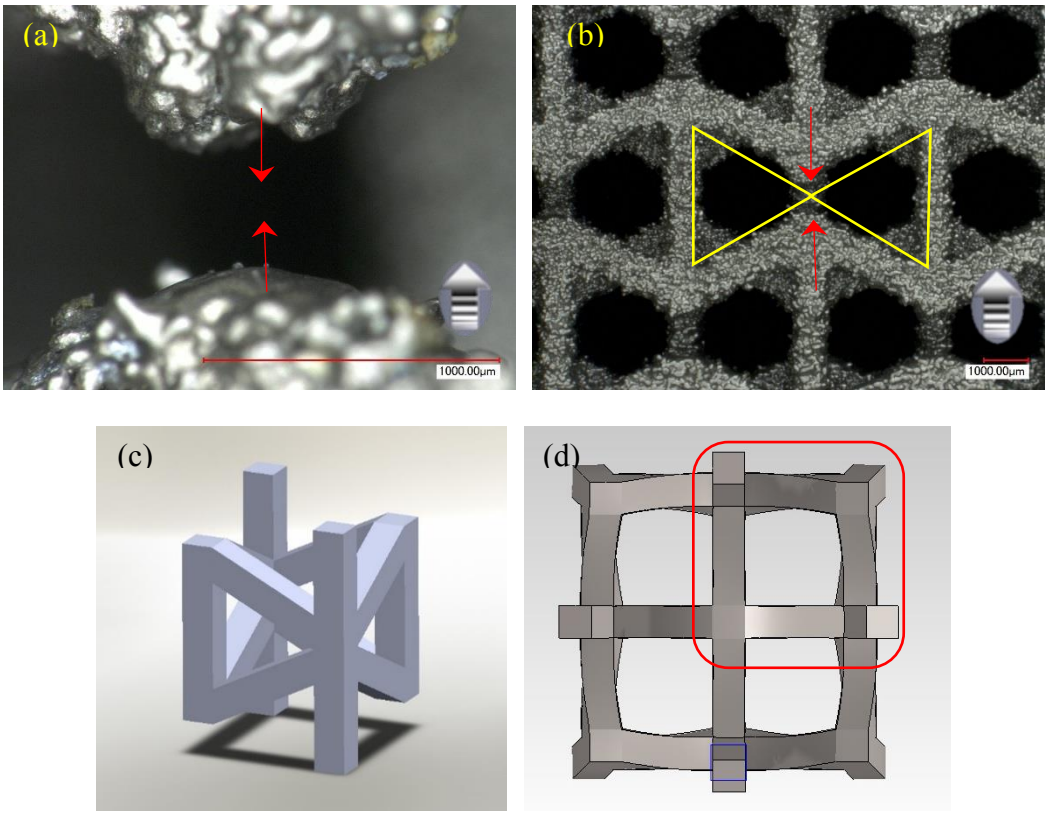

Figure 4.28 Deformation of a reentrant hexagonal unit-cell: jaw-like (a); schematic of the expected unit-cell transformation (b); rendering of the new unit-cell after transformation (c); rendering of the top view of a deformed reentrant hexagonal unit-cell reconfigured into four new triangular unit-cells (d)

Chapter 5: FEM of EBM Ti-6Al-4V cellular lattices

The preceding chapters provided a discussion of the different characteristics and properties of cellular metals, including experimental testing results. This chapter presents the results of an effort to incorporate what was learned in these previous chapters into the numerical modeling of these metamaterials with the goal of presenting best practices and guidelines. The previously presented test results and analyzes exposed the many complex interactions defining the characterization of cellular metal solids and how they distinguish themselves from standard solid metals. The introduction of hierarchical levels at mesoscale takes the metamaterials to another level of performance; their highly customizable mechanical properties make them of great interest for innovative applications, which require significant experimental work where reliable computational models are important in predicting results from experiments. However, because of the small-scale, the complex geometry and interactions in the lattices, the development of automatic meshers and the finite element model itself are still challenges of interest.

5.1 Finite Element Model

Presented in this chapter are the Finite Element Models (FEM) of the two types of lattices at the three different densities corresponding to unit-cell sizes of 5mm, 6mm and 7mm. The rapid prototyping process started with the 3D-solid CAD designing of the proposed lattices in Solidworks from Dassault Systèmes. This CAD served as the root file, from where the stereolithography (.stl) and the parasolid (.x_t) format files were exported for fabrication and FEM in the ARCAM A2 system and Patran software respectively. Thus, any modifications in the design can easily be applied in one and only CAD from where the process can restart.

The FEM started with importing the .x_t file into MSC Patran, at the correct scale and required tolerance of dimensions. Three different conditions were observed in the model: solid bearing plates fabricated at 90°, and microstruts fabricated at 90° and 30°; therefore, three different materials were created in the FEM. The load distribution plates were defined as *bulk* Ti-6Al-4V,

fabricated at 90° whose mechanical properties from the experiments were determined as isotropic with E=113GPa and υ = 0.33. The vertical microstruts were defined as *90° microstrut* Ti-6Al-4V, whose mechanical properties from the tensile experiments on microstruts at 90° were determined as isotropic with E=113GPa and υ = 0.33. The inclined microstruts were defined as *30° microstrut* Ti-6Al-4V, whose mechanical properties from the tensile experiments on microstruts at 30° were determined as isotropic with E=104GPa and υ = 0.31. The linear elastic and elastoplastic constitutive models were set for both *microstrut* Ti-6Al-4V properties, whereas for the *bulk* Ti-6Al-4V only the linear elastic model was set, given the expected strain distribution throughout the lattice. The elastoplastic constitutive models were defined by data fields extracted from averaging the stress-strain curves from the actual experiments (Figure 5.1). Additionally, the lattices were modeled with material properties from the ASTM E8 standard tension tests, and from the tension test on microstruts.

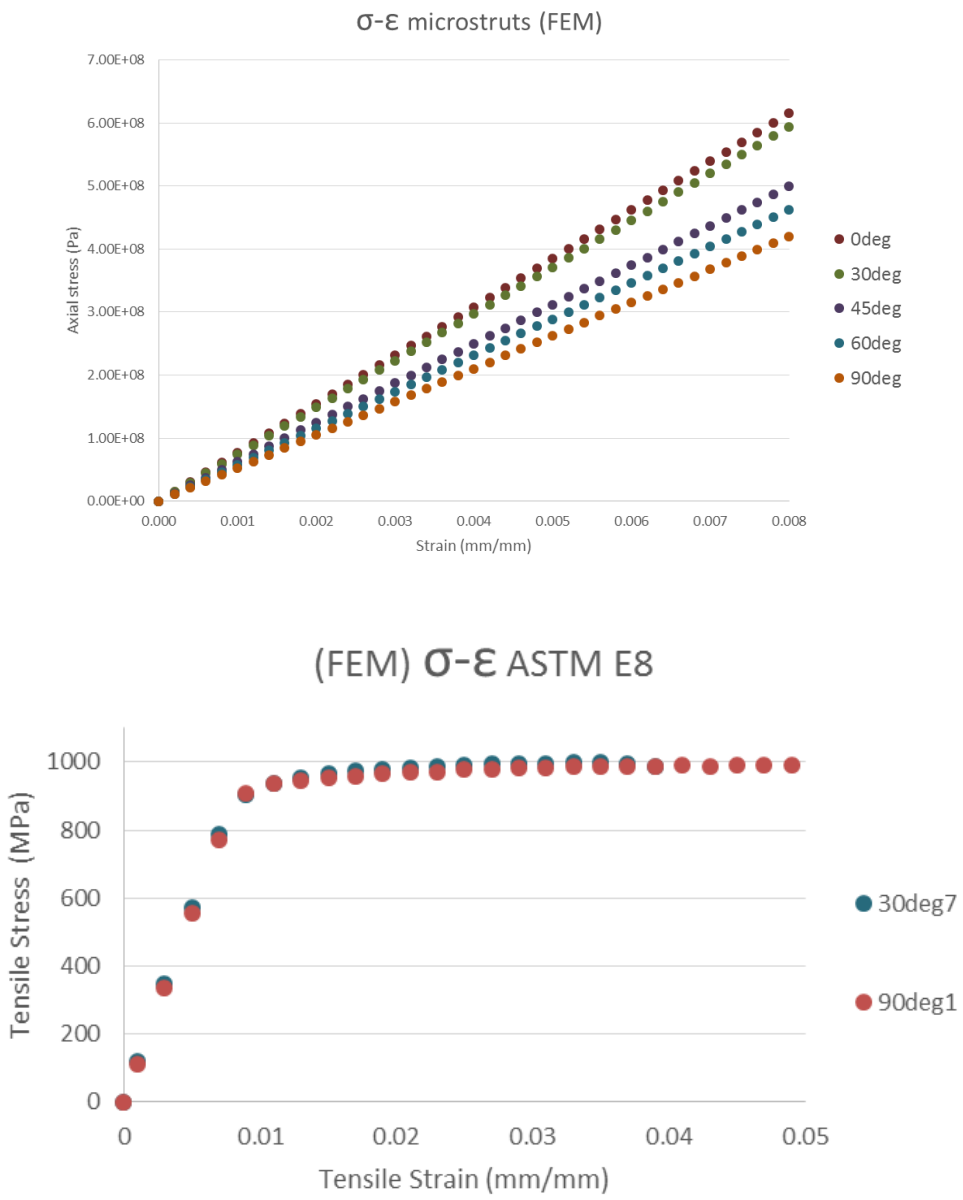

Figure 5.1 Stress-strain data plots. For clarity, only 30° and 90° standard tension are shown.

Defining T1, T2, and T3 as translations along orthogonal axes 1, 2 and 3, also named *x*, *y* and *z*, where *x*-*z* denotes the horizontal plane, the nodes in the bottom surface of the solid model were constrained for *z* displacements; similarly, for rotations around the axes R1, R2 and R3, these nodes at the bottom were also constrained for R1 and R3. Total constrain was applied only to nodes of the element at the center of this surface. The upper surface of the plate at the top was exclusively

loaded with the vertical element-uniform displacements corresponding to the ultimate strengths recorded by DIC during the experiments presented in Chapter 3 (Figure 5.2) (Table 5.1).

The complex geometry of the 3D CAD solids representing the lattices restricted the element selection to tetrahedrons; based on the nonlinear response observed during testing, the quadratic 10-node tetrahedron (Tet10) was suggested, because the extra node on its sides derives in quadratic shape functions permitting to better capture the nonlinear behavior observed in the testing.

For the initial simulations, the mesh was automatically generated by the solids mesher *TetMesh* by MSC Patran. The mesh density is controlled by the *global edge length* parameter; where the longest edge in the geometry, divided by this parameters defines the number of elements along the edge. *TetMesh* recognizes the longest edge from the geometry of the solid, automatically determining the *global edge length* based on the minimum element edge length, which has a default value of 20% of the *global edge length*, producing elements of acceptable quality. Thus, the *global edge* length was different for each size of lattice in meshes generated automatically.

As a gauge, that facilitated the measurement of the reaction force of the whole lattice at a single point, an additional multipoint constrain element (MPC-RBE2) collecting all the reaction forces from the surface nodes on the exposed face of the bottom bearing plate was included. The RBE2 is characterized by a relationship purely dependent on nodal displacements, meaning it does not possess neither stiffness, mass, force, nor any other relationship (Figure 5.2).

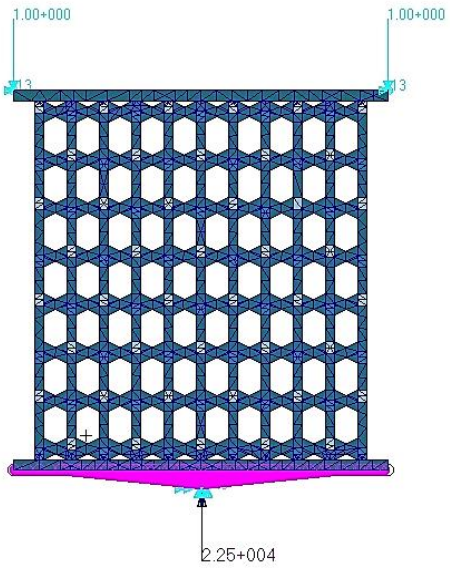

Figure 5.2 FEM of the hexagonal, 6mm lattice loaded with 1mm element-uniform displacement. MPC and resultant force vector at the bottom.

5.2 Finite Element Analysis

The simulations were run in a Dell Precision T5500 computer equipped with Intel Xeon E5603 processor and 6GB DDR3 SDRAM operating at 64-bit. For the solution, the model was divided into four domains with similar number of elements each, and the maximum RAM compromised to solve the model was set at 80%, saving the remaining 20% for the basic operation of the system. The project is solved in Nastran SOL600; a solver for implicit nonlinear solution, following full Newton-Raphson methods with a maximum of 20 iterations per increment, residual force of 0.1 and automatic abort if failed to converge. The adaptive feature is set for defining the loading increments.

5.3 Convergence Analysis

Convergence analyses were conducted for all models to ensure that the mesh density was not considerably affecting the results. Four different mesh densities were explored for each of the models representing each of the lattices. One of the densities was the one produced by *TetMesh*.

Given that the mesher takes in consideration the longest edge in the geometry, the mesh refinement controlled by the *global edge length* (longest geometrical/number of elements) would prioritize the bearing plates. A more effective way to properly size the mesh in these solids was found to define and control the separation of mesh seeds along the edges of the microstruts, in other words, adding more elements where the stress is distributed.

The convergence analysis compared the resultant force at the RBE2 element, produced from applying the displacements at the ultimate strength in the experiments, with the number of elements in the model. Starting at about 70,000 elements, the convergence curves showed a tendency to consistent results. In regards to the computational work, the models started to be significantly more expensive around the 100,000 elements, where the *relative efficiency* (number of elements / wall time) escalated with no significant change in the resultant force (Table 5.1) (Figure 5.3). Thus, the mesh seeding along the microstruts was demonstrated as an effective way for the mesh refinement, and that the consistency of the results may be acceptable in the range of 70,000 to 100,000 elements, when the computational work becomes considerably more expensive.

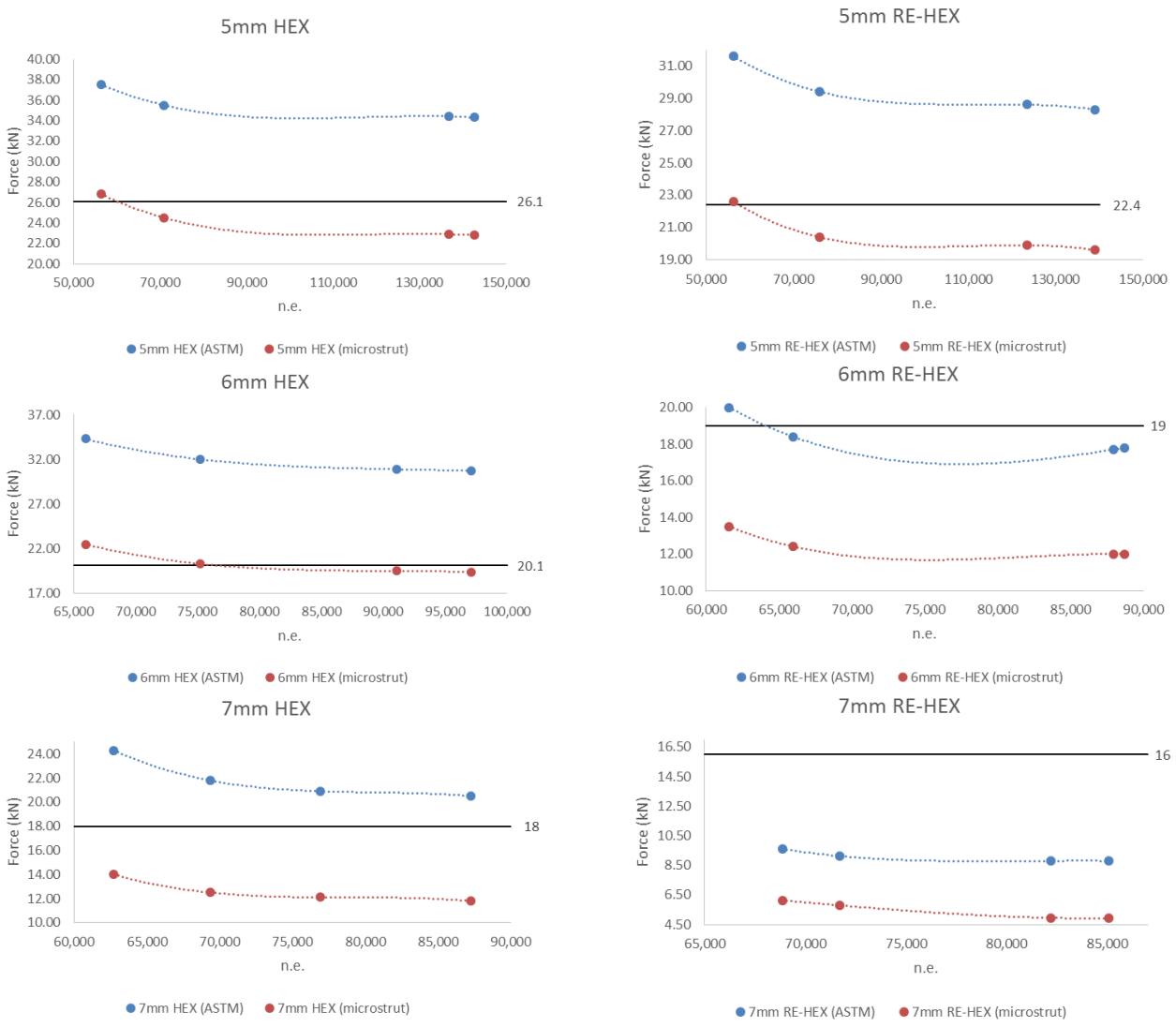

Figure 5.3 Mesh convergence curves for hexagonal (left) and reentrant hexagonal (right) models. 5mm, 6mm and 7mm unit-cell sizes (top to bottom); two material properties per graph are shown. Solid line representing the experimental average ultimate load.

5.4 Results

The results of the analyses were evaluated by comparing the nodal force reaction from the independent node at the RBE2 element and the average ultimate force from the experiments. The models were created in two variants: one using the material properties data from the ASTM E8 tests, and another with the data from the tension tests of microstruts.

In general, the models displayed a very uniformly distributed of stress fields throughout the latticed region, suggesting an efficient energy-distributing material (Figure 5.4). The models also indicated that inclined microstruts absorb most of the loading, thus it is advisable to optimize them for an increased capacity (Figure 5.6). The 90° microstruts showed a lower stress among both configurations, however, the reentrant hexagonal lattices presented columns with lower stresses than the hexagonal. These conditions are the result of the purely compressive state in the hexagonal cells compared to the combination of inclined microstruts in tension and columns under compression in the reentrant hexagonal lattice (Figure 5.5). It was observed that, by extending the compressive forces to the columns, the purely compressive state better distributed the stresses to more material, compared to the stress distribution at the nodes in the reentrant hexagonal lattices (Figure 5.7). This more uniform stress distribution by the hexagonal unit-cells explains the failure at lower loads of the reentrant hexagonal lattices that concentrates most of the stress in the inclined microstruts under tension (Figure 5.8). In similar manner, the inclined microstruts are observed to support most of the shear stress (Figure 5.9) .It is important to be aware that, because of the fragility of the Ti-6Al-4V, the reentrant unit-cells failed before completely developing its negative Poisson effect, and before the cells reconfigured for a second, purely compressive, loading stage that might result in stronger materials with the same amount of mass.

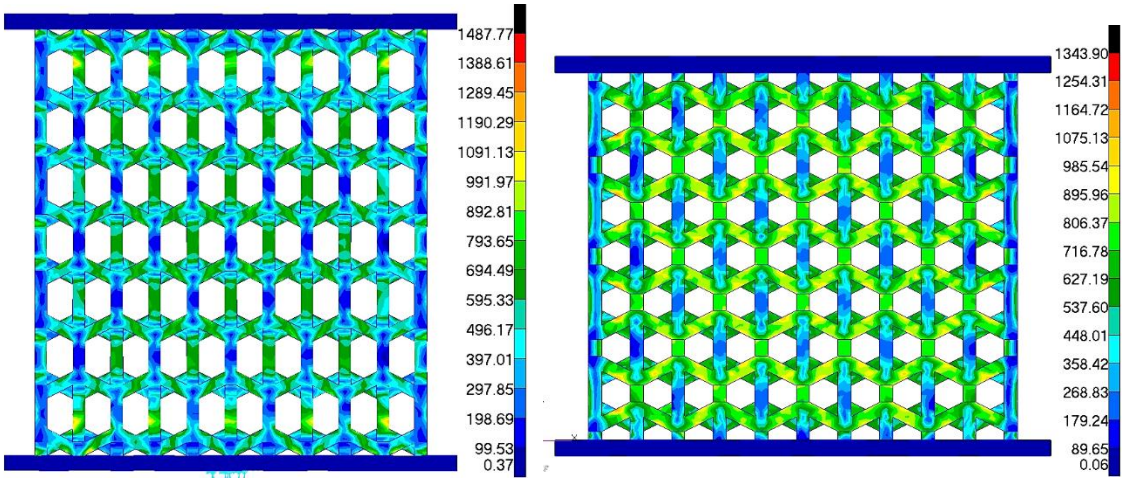

Figure 5.4 von Mises stress distribution (MPa) in hexagonal (left) and reentrant hexagonal (right) 5mm lattices. Darker colors indicate lower stress.

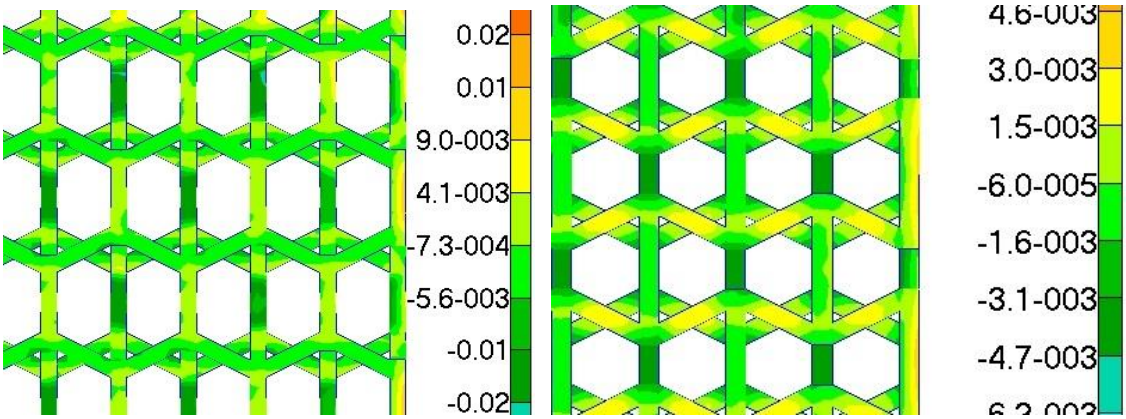

Figure 5.5 Stress "Y" component in MPa; purely compressive stress state in 7mm hexagonal lattices (left). Tension (-) and compression (+) stresses in 7mm reentrant lattices (left).

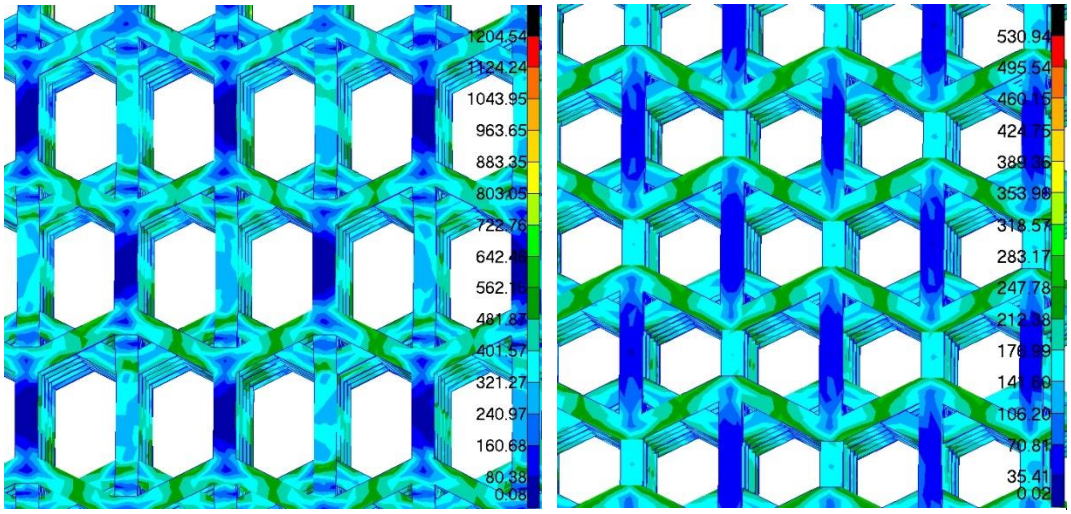

Figure 5.6 Inclined microstruts, in light color, indicating higher von Mises stress (MPa).

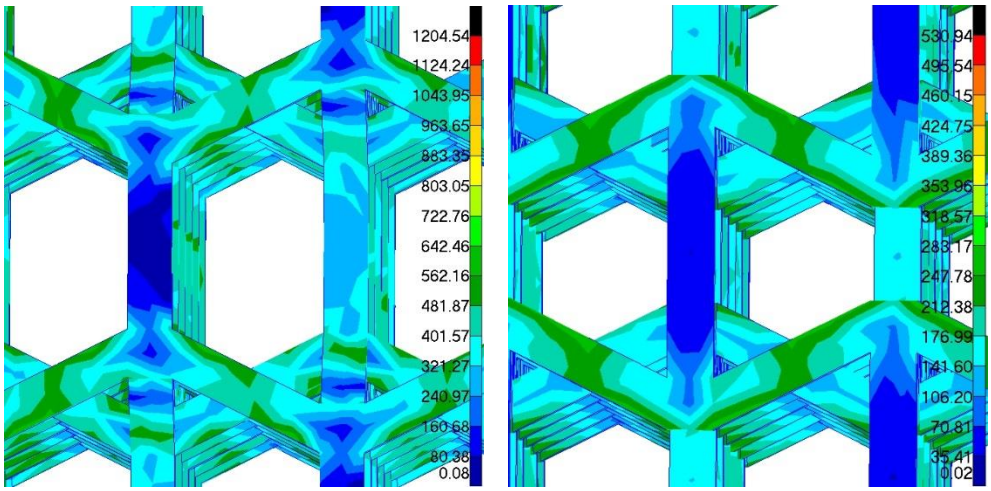

Figure 5.7 Stressed microstruts and low-stress columns in reentrant hexagonal lattices. Columns in hexagonal lattices dispersing compressive stresses from microstruts (left).

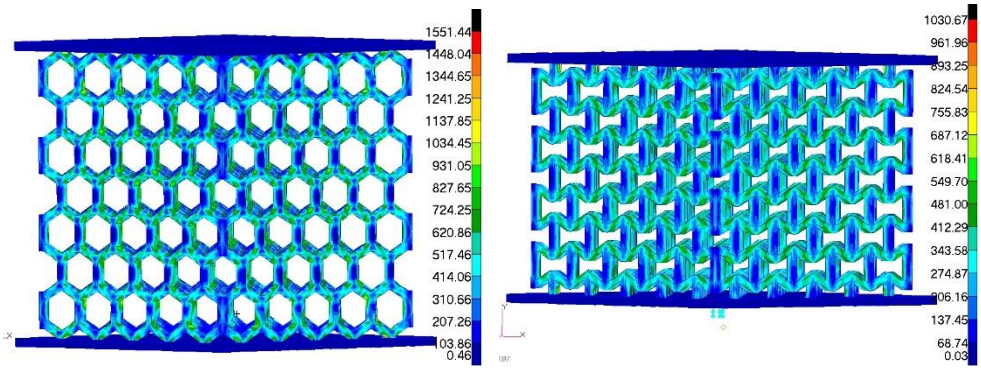

Figure 5.8 Dimetric of 6mm lattices displaying von Mises stress distribution (MPa).

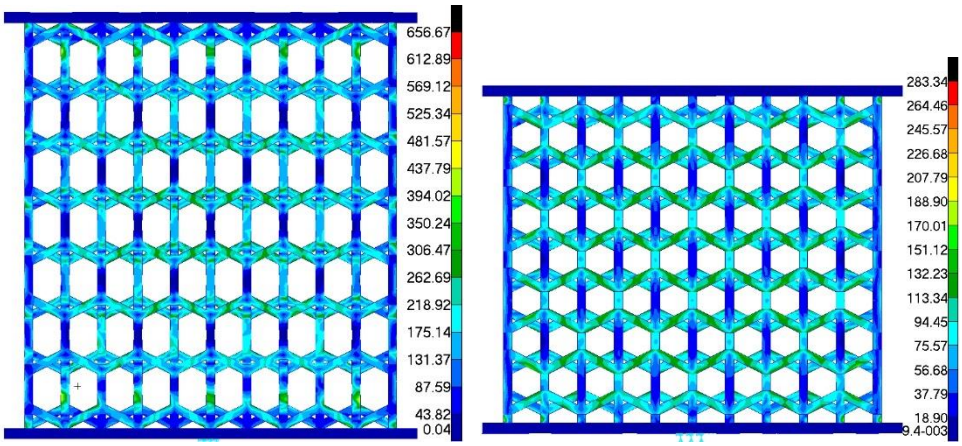

Figure 5.9 Shear stress distribution in 7mm lattices (MPa).

Although the models exhibited convergence, demonstrating that results stabilize with denser meshes, not all the models showed accuracy in predicting the experimental results. The hexagonal lattice models, with material properties from the experimental data from testing microstruts, displayed resultant forces (at the RBE2) closer to the average experimentally obtained values. On the other hand, results from the reentrant hexagonal lattices showed closer values to the experimental results, when the material properties input data derived from the standard tension tests (Table 5.1) (Figure 5.3). On the comparison of material properties, the models with materials properties developed from the microstrut tests showed to be more accurate than using data from standard tension tests (Table 5.1), this could be explained from the larger sensitivity to manufacturing defects of the microstruts, adding uncertainty; besides the removal of surface

defects in ASTM E8 specimens. On the comparison of the selected geometry; the hexagonal geometries exhibited values closer to the experimental results, when compared to the reentrant hexagonal (Figure 5.3), this could be caused by the more complex stress distribution subjected to tension and compression in the reentrant hexagons, compared to the purely-compressive stress state in the hexagonal lattice (Figure 5.5). On the comparison of the size of the unit-cell; the smallest size (5mm) showed more accurate (Figure 5.3); this, given the increased density of the lattice diminishing the geometrical nonlinearities introduced at the mesoscale, in other words, the smaller the unit-cell, the denser the lattice, and the closer of this to uniformly behave as a standard solid.

The two unit-cell configurations displayed more uniformly distributed plastic strain fields for larger unit-cell sizes (Figure 5.10). Another interesting, and expected, feature in the models is that the largest strains developed in the microstuts in the interior of the lattice, because the larger load received (Figure 5.11). The reentrant hexagonal lattice models were also capable of developing the negative Poisson effect (Figure 5.12); suggesting an additional argument favoring the confidence on the FEM for evaluating the auxetic deformation mechanisms, and therefore the strain field distribution.

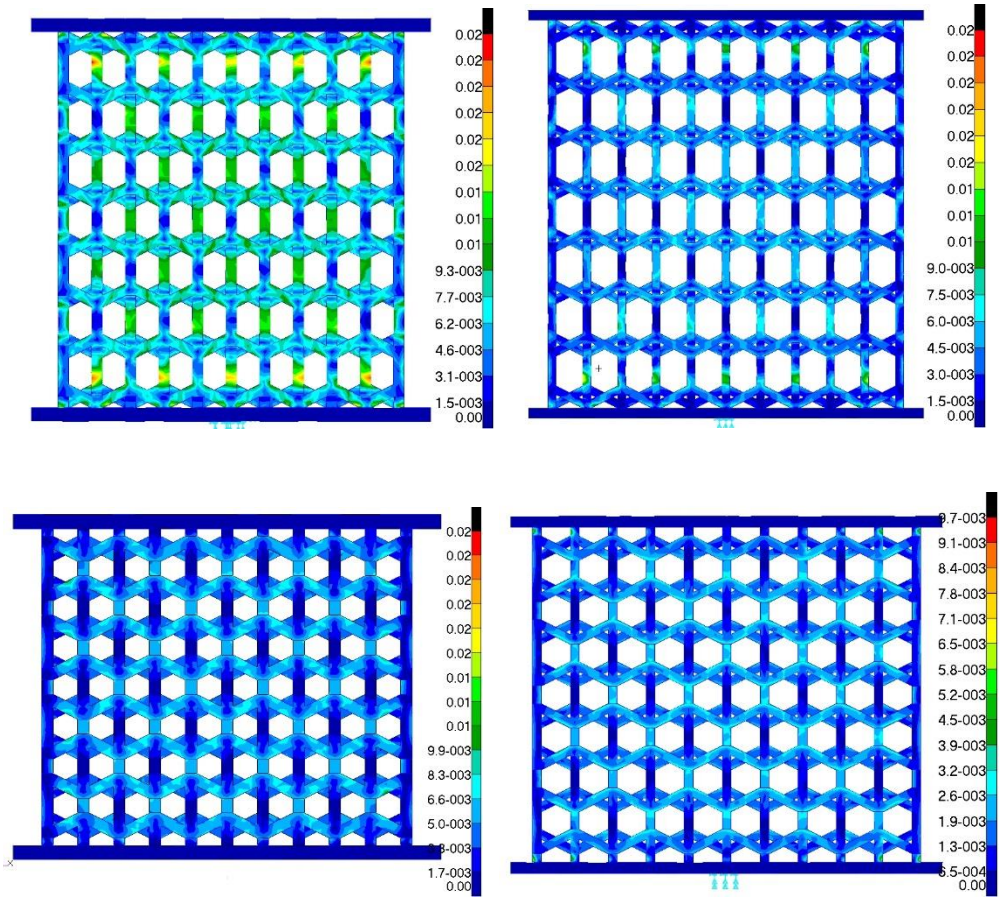

Figure 5.10 von Mises plastic strain hexagonal (top) and reentrant hexagonal (bottom) lattices with 5mm (left) and 7mm (right) unit-cells.

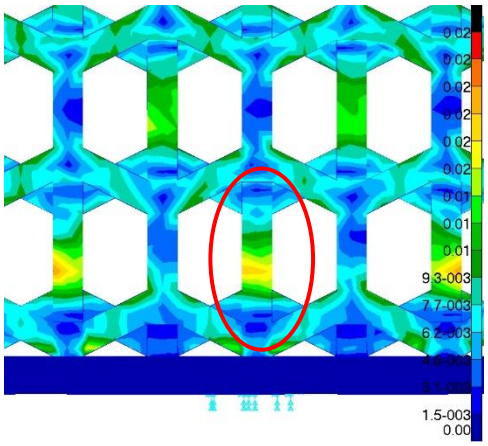

Figure 5.11 Plastic strain in interior microstruts.

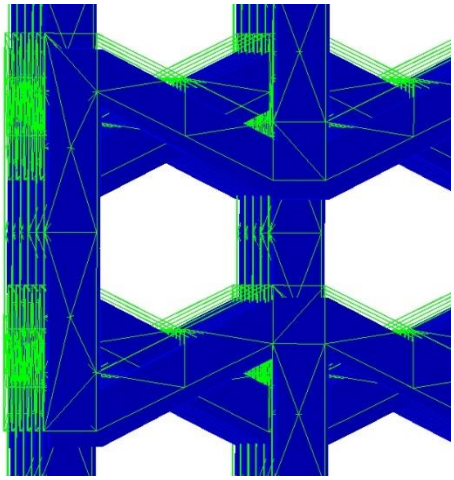

Figure 5.12 Undeformed model wireframe in highlighted light color on the left side face of the lattice, highlighting the auxetic behavior.

Table 5.1 Summary of FEMs at different mesh density and material properties.

Lattice	Exp.Avg. Ult.Load (kN)	Std.Dev. (kN)	c.o.v.
5mm HEX, 0.8mm strut	26.10	0.70	0.03
6mm HEX, 0.8mm strut	20.10	1.03	0.05
7mm HEX, 0.8mm strut	18.00	0.75	0.04
5mm RE-HEX, 0.8mm strut	22.40	0.50	0.02
6mm RE-HEX, 0.8mm strut	19.00	0.69	0.04
7mm RE-HEX, 0.8mm strut	16.00	1.34	0.08

FEM / Experimental	# of seeds 90° microstruts	# of seeds 30° microstruts	n.e.	Force (kN) *w/std. properties*	% change	Error Vs Exp.	Force (kN) *w/microstrut properties*	% change	Error Vs Exp.	Walltime (s) w/std. properies	% change	Relative efficiency (n.e./s)	Walltime (s) w/microstrut properties	% change	Relative efficiency (n.e./s)
5mm HEX avg.experimental (displ.=0.82mm, F=26.1kN)	auto	auto	56,364	37.50	-	43.68%	26.80	-	2.68%	912	-	61.8	955	-	59.0
	2	2	70,903	35.50	-5.3	36.02%	24.50	-8.6	-6.13%	2,255	147.3	31.4	1,211	26.8	58.5
	2	3	136,761	34.40	-8.3	31.80%	22.90	-14.6	-12.26%	31,318	3334.0	4.4	27,933	2824.9	4.9
	2	3	142,697	34.30	-8.5	31.42%	22.80	-14.9	-12.64%	31,173	3318.1	4.6	29,658	3005.5	4.8
6mm HEX avg.experimental (displ.=1.0mm, F=20.1kN)	auto	auto	65,955	34.30	-	70.65%	22.50	-	11.94%	1,156	-	57.1	1,182	-	55.8
	3	2	75,251	32.00	-6.7	59.20%	20.30	-9.8	1.00%	1,443	24.8	52.1	1,625	37.5	46.3
	2	3	91,101	30.90	-9.9	53.73%	19.50	-13.3	**-2.99%**	2,420	109.3	37.6	2,546	115.4	35.8
	3	3	97,120	30.70	-10.5	52.74%	19.40	-13.8	-3.48%	1,356	17.3	71.6	1,401	18.5	69.3
7mm HEX avg.experimental (displ.=0.9mm, F=18.0kN)	auto	auto	62,726	24.30	-	35.00%	14.00	-	-22.22%	1,000	-	62.7	1,021	-	61.4
	3	2	69,329	21.80	-10.3	21.11%	12.50	-10.7	-30.56%	1,098	9.8	63.1	1,120	9.7	61.9
	2	3	76,907	20.90	-14.0	16.11%	12.10	-13.6	-32.78%	1,375	37.5	55.9	1,228	20.3	62.6
	3	3	87,226	20.50	-15.6	13.89%	11.80	-15.7	-34.44%	3,582	258.2	24.4	3,525	245.2	24.7
5mm RE-HEX avg.experimental (displ.=0.68mm, F=22.4kN)	auto	auto	56,214	31.60	-	41.07%	22.60	-	0.89%	1,197	-	47.0	1,399	-	40.2
	3	2	76,005	29.40	-7.0	31.25%	20.40	-9.7	-8.93%	1,262	5.4	60.2	1,262	-9.8	60.2
	2	3	123,517	28.60	-9.5	27.68%	19.90	-11.9	-11.16%	14,708	1128.7	8.4	14,708	951.3	8.4
	3	3	138,970	28.30	-10.4	26.34%	19.60	-13.3	-12.50%	21,429	1690.2	6.5	21,429	1431.7	6.5
6mm RE-HEX avg.experimental (displ.=0.59mm, F=19.0kN)	auto	auto	61,584	20.00	-	5.26%	13.50	-	-28.95%	705	-	87.4	676	-	91.1
	2	2	65,992	18.40	-8.0	-3.16%	12.40	-8.1	-34.74%	848	20.3	77.8	957	41.6	69.0
	2	3	88,714	17.80	-11.0	**-6.32%**	12.00	-11.1	-36.84%	1,169	65.8	75.9	1,412	108.9	62.8
	3	3	87,944	17.70	-11.5	-6.84%	12.00	-11.1	-36.84%	1,728	145.1	50.9	2,129	214.9	41.3
7mm RE-HEX avg.experimental (displ.=0.38mm, F=16.0kN)	auto	auto	68,858	9.60	-	-40.00%	6.14	-	-61.63%	1,156	-	59.6	1,162	-	59.3
	2	2	71,701	9.13	-4.9	-42.94%	5.80	-5.5	-63.75%	1,116	-3.5	64.2	1,282	10.3	55.9
	3	3	82,183	8.80	-8.3	-45.00%	4.95	-19.4	-69.06%	1,471	27.2	55.9	1,718	47.8	47.8
	2	3	85,062	8.80	-8.3	-45.00%	4.93	-19.7	-69.19%	3,652	215.9	23.3	1,847	59.0	46.1
			Avg.err. (std.prop.) 32.76%	Avg.err. (microstruts) 25.32%	Avg.err. (HEX) 26.60%	Avg.err. (REHEX) 31.47%	Avg.err. (5mm) 21.13%	Avg.err. (6mm) 25.18%	Avg.err. (7mm) 41.06%						

Chapter 6: Conclusions

6.1 Remarks

Additive manufacturing, especially powder bed fusion, allows for the design and fabrication of cellular metals, or what could be defined as metametals. The extraordinary design freedom of powder bed fusion technologies empowered material designers to create these highly customizable metals whose properties are a consequence, mostly, of the introduction of hierarchical levels at the mesoscale.

The designing of cellular latticed metals is still far from a defined set of theoretical methods, such as in the case of solid mechanics. However, the multiscale approach presented could set the line of thought to developing design methodologies.

In the work presented here, DIC was an invaluable resource for the measurement of strain fields variations caused by the manufacturing orientation, as well as deformations in specimens with complicated shapes for which specific measuring instrumentation may be required, and without recording the error from the grips/platens in the UTM.

The mesh discretization in the modeling of cellular metals introduces, what can be seen as an additional hierarchical level, in which the shape and size of the elements also affect the models results, as well as the fidelity of the stress/strain fields displayed. Thus, the importance of the convergence analysis in reducing the effects of the mesh size on the performance of the model.

6.2 Conclusions.

a) Engineering of cellular metals is far from a standardized set of concepts and theories. However, the multiscale analysis approach presented herein provides a comprehensive understanding and a structured way of thinking on the multiple factors affecting the performance of lattices, and how these can be addressed to achieve a desired response (Chapter 4).

b) Nonlinear effects introduced by the unit-cell geometries into lattices can be used to compensate for the lack of plasticity in the constitutive solid (Figure 4.22) (4.3.1 Deformation Mode).

c) Auxetic cellular metals are made possible with solely changing the spatial location of microstruts; from a hexagonal to a reentrant hexagonal unit-cell (4.2.2 Auxetics).

d) Although the complex geometry of the lattices limited the selection of elements to tetrahedrons, the resultant compression force in the FEMs show convergence for mesh refinement (Figure 5.3).

e) *TetMesh* was found not effective in increasing the density of the mesh for these kind of models. A better approach was presented by mesh seeding the edges of the microstruts. Following the mesh seeding approach for the mesh generation, the variation of the results, because the size of the mesh, can be neglected for models over 70,000 elements, but no larger than 100,000, when the computational work dramatically increases.

f) On the prediction of the experimental compressive forces applied, some models showed considerable errors (up to 70.65%); however, this error needs to be viewed within the context of the variability in the material properties as shown in Table 3.1, where the COV of the failure loads for microstruts can be as high 0.353. In general; on the selected geometry, the hexagonal models showed more accurate compression forces compared to the reentrant hexagonal. On the material properties used for modeling, the models with input data derived from testing microstruts showed more accurate with an average error of 25.32% in predicting the average experimental force, compared to those with input data from ASTM E8 tests, with an average error of 32.76%. On the unit-cell size, the smallest (5mm) showed more accurate in estimating the experimental compression force (Table 5.1). In summary, in predicting the average experimental resultant compression force applied, the model for hexagonal lattices showed to be more accurate, with a 2.99% average

error, for the 6mm unit-cell and microstrut properties; whereas the most accurate models for reentrant hexagonal lattices was found with 6mm unit-cell and standard material properties, with an average error of 6.32%.

g) While some FEMs may not be accepted as accurate in predicting the resultant forces, the widely-accepted Gibson-Ashby model was also deficient in estimating the ultimate strength from the experiments. This can be explained by the fact that the unit-cell considerations from the analytic model differ from the proposed herein, such as the manufacturing orientation. However, the Gibson-Ashby model is conservative by emphasizing the experimental nature of the proportionality constant.

6.3 Recommendations and Future Work.

In the development of the designing of cellular metals toward a more standardized process, it is recommended to follow a multiscale approach and start developing mathematical models and statistical approaches that allow for the quantification of toughness, in function of the multiple factors presented.

On the development of more effective automatic meshers; it is recommended that commercial FEM platforms wishing to start modeling cellular lattices, to allow the user to specify the region of interest where the *global edge length*, as discussed in the convergence analysis, needs to be defined.

On the error of the models predicting the experimental results; it may be advisable to investigate the development of newer technologies for finite elements that allow to capture the nonlinear effects of the geometries introduced at the mesoscale.

On improving the accuracy of the presented models, a more elaborated model with mixed elements could be developed. For example, for mechanistic unit-cells, in regions where high stresses are expected, such as in the nodes of the lattices, elements of higher order are better suited

for capturing stress distribution, whereas first order elements may be suitable for the microstruts. However, this could be time consuming, and thus, it might be seem restrictive in rapid prototyping.

Although the material properties derived from testing microstruts include the effect of the manufacturing defects, the uncertainty on the properties remains high, because of the size of the microstrut. In that context, and because the nodes of the finite elements are assigned in a deterministic, the manufacturing defects could also be included in the FEM, by randomly varying the coordinates of the nodes at the free faces of the elements. The limits for this random variation could be defined by the metrics of the surface defects in microstruts.

Lastly, in further understanding the capabilities and limitations of the commercial FEM/FEM platforms simulating cellular solids with large deformations, it is recommended to evaluate the presented development of these models using more ductile constituent solid such as stainless steel.

Chapter 7: References

Arcam. n.d. “Arcam-Ti6Al4V-Titanium-Alloy.pdf.”

“Arcam History.” 2014. *Arcam AB*. Accessed May 16. http://www.arcam.com/company/about-arcam/history/.

Ashby, M. F., Evans, A., Fleck, N.A., Gibson, L.J., Hutchinson, J.W., and Wadley, H.N.G. 2000. *Metal Foams - A Design Guide*. Boston: Butterworth-Heinemann.

Ashby, M.F. 2006. “The Properties of Foams and Lattices.” *Philosophical Transactions of the Royal Society A: Mathematical, Physical and Engineering Sciences* 364 (1838): 15–30. doi:10.1098/rsta.2005.1678.

ASTM International. 2009. “ASTM E9-09 Standard Test Methods of Compression Testing of Metallic Materials at Room Temperature.”

———. 2016. “ASTM E8/E8M-16a Standard Test Methods for Tension Testing of Metallic Materials.”

Biamino, S., A. Penna, U. Ackelid, S. Sabbadini, O. Tassa, P. Fino, M. Pavese, P. Gennaro, and C. Badini. 2011. “Electron Beam Melting of Ti–48Al–2Cr–2Nb Alloy: Microstructure and Mechanical Properties Investigation.” *Intermetallics*, 3rd IRC International Workshop 13-14 May 2010, 19 (6): 776–81. doi:10.1016/j.intermet.2010.11.017.

Cansizoglu, O., O. Harrysson, D. Cormier, H. West, and T. Mahale. 2008. “Properties of Ti–6Al–4V Non-Stochastic Lattice Structures Fabricated via Electron Beam Melting.” *Materials Science and Engineering: A* 492 (1–2): 468–74. doi:10.1016/j.msea.2008.04.002.

Cheng, Alice, Aiza Humayun, David J. Cohen, Barbara D. Boyan, and Zvi Schwartz. 2014. “Additively Manufactured 3D Porous Ti-6Al-4V Constructs Mimic Trabecular Bone Structure and Regulate Osteoblast Proliferation, Differentiation and Local Factor Production in a Porosity and Surface Roughness Dependent Manner.” *Biofabrication* 6 (4): 045007. doi:10.1088/1758-5082/6/4/045007.

Cheng, X. Y., S. J. Li, L. E. Murr, Z. B. Zhang, Y. L. Hao, R. Yang, F. Medina, and R. B. Wicker. 2012. “Compression Deformation Behavior of Ti–6Al–4V Alloy with Cellular Structures Fabricated by Electron Beam Melting.” *Journal of the Mechanical Behavior of Biomedical Materials* 16 (December): 153–62. doi:10.1016/j.jmbbm.2012.10.005.

Deshpande, V. S., M. F. Ashby, and N. A. Fleck. 2001. “Foam Topology: Bending versus Stretching Dominated Architectures.” *Acta Materialia* 49 (6): 1035–40. doi:10.1016/S1359-6454(00)00379-7.

“EOS Global Presence.” 2014. *EOS Global Presence*. Accessed May 16. http://www.eos.info/about_eos/global_presence.

Giessen, Erik van der. 2011. “Materials Physics: Bending Maxwell’s Rule.” *Nature Physics* 7 (12): 923–24. doi:10.1038/nphys2146.

Gong, Haijun, Khalid Rafi, Thomas Starr, and Brent Stucker. 2013. “The Effects of Processing Parameters on Defect Regularity in Ti-6Al-4V Parts Fabricated By Selective Laser Melting and Electron Beam Melting.” In *ResearchGate*. https://www.researchgate.net/publication/272167481_The_Effects_of_Processing_Parameters_on_Defect_Regularity_in_Ti-6Al-4V_Parts_Fabricated_By_Selective_Laser_Melting_and_Electron_Beam_Melting.

Gorny, B., T. Niendorf, J. Lackmann, M. Thoene, T. Troester, and H. J. Maier. 2011. “In Situ Characterization of the Deformation and Failure Behavior of Non-Stochastic Porous Structures Processed by Selective Laser Melting.” *Materials Science and Engineering: A* 528 (27): 7962–67. doi:10.1016/j.msea.2011.07.026.

Gümrük, R., and R. A. W. Mines. 2013. “Compressive Behaviour of Stainless Steel Micro-Lattice Structures.” *International Journal of Mechanical Sciences* 68 (March): 125–39. doi:10.1016/j.ijmecsci.2013.01.006.

Hernández-Nava, E., C. J. Smith, F. Derguti, S. Tammas-Williams, F. Leonard, P. J. Withers, I. Todd, and R. Goodall. 2016. “The Effect of Defects on the Mechanical Response of Ti-6Al-4V Cubic Lattice Structures Fabricated by Electron Beam Melting.” *Acta Materialia* 108 (April): 279–92. doi:10.1016/j.actamat.2016.02.029.

Jan Schwerdtfeger, Robert F. Singer, and Carolin Körner. 2012. “In Situ Flaw Detection by IR-imaging during Electron Beam Melting.” *Rapid Prototyping Journal* 18 (4): 259–63. doi:10.1108/13552541211231572.

Kwon, Y. W., R. E. Cooke, and C. Park. 2003. “Representative Unit-Cell Models for Open-Cell Metal Foams with or without Elastic Filler.” *Materials Science and Engineering: A* 343 (1–2): 63–70. doi:10.1016/S0921-5093(02)00360-X.

Lakes, R. S., and R. Witt. 2002. “Making and Characterizing Negative Poisson’s Ratio Materials.” *International Journal of Mechanical Engineering Education* 30 (1): 50–58.

Lakes, Roederic. 1987. “Foam Structures with a Negative Poisson’s Ratio.” *Science*, no. 235: 1038–40.

Larsen, Ulrik Darling, Ole Sigmund, Siebe Bouwstra, Ulrik Darling Larsen, Ole Sigmund, and Siebe Bouwstra. 1997. “Design and Fabrication of Compliant Micromechanisms and Structures with Negative Poisson’s Ratio.” *I E E E Journal of Microelectromechanical Systems* 6: 99–106. doi:10.1109/84.585787.

Li, S. J., L. E. Murr, X. Y. Cheng, Z. B. Zhang, Y. L. Hao, R. Yang, F. Medina, and R. B. Wicker. 2012. “Compression Fatigue Behavior of Ti–6Al–4V Mesh Arrays Fabricated by Electron Beam Melting.” *Acta Materialia* 60 (3): 793–802. doi:10.1016/j.actamat.2011.10.051.

Liebenstein, Stefan, Stefan Sandfeld, and Michael Zaiser. 2016. “Modelling Elasticity of Open Cellular Foams: Size Effects and Disorder.” *arXiv Preprint arXiv:1604.03589*. http://arxiv.org/abs/1604.03589.

Lorna J. Gibson, and Michael F. Ashby. 1999. *Cellular Solids: Structure and Properties*. Second. Cambridge University Press.

Luca Facchini, Emanuele Magalini, Pierfrancesco Robotti, Alberto Molinari, Simon Höges, and Konrad Wissenbach. 2010. “Ductility of a Ti-6Al-4V Alloy Produced by Selective Laser Melting of Prealloyed Powders.” *Rapid Prototyping Journal* 16 (6): 450–59. doi:10.1108/13552541011083371.

Made in Space. 2013a. “First Space-Based 3D Printer Passes Crucial Milestone for Flight Certification.” *Made in Space*. http://www.madeinspace.us/space-based-3d-printer-passes-crucial-milestone-flight-certification.

———. 2013b. “Made in Space.” *Made in Space*. http://www.madeinspace.us.

Maxwell, J. Clerk. 1864. “L. On the Calculation of the Equilibrium and Stiffness of Frames.” *Philosophical Magazine Series 4* 27 (182): 294–99. doi:10.1080/14786446408643668.

Mireles, Jorge. 2016. “Joining of Metallic Structures Using Powder Bed Fusion Additive Manufacturing Technology.” In *Solid Freeform Fabrication Symposium*. Austin, TX.

“Multi-Year Overview | Ir.arcam.se.” 2014. Accessed May 16. http://ir.arcam.se/en/financial-information/multi-year-overview/.

Murr, L. E., S. M. Gaytan, F. Medina, H. Lopez, E. Martinez, B. I. Machado, D. H. Hernandez, et al. 2010. “Next-Generation Biomedical Implants Using Additive Manufacturing of Complex, Cellular and Functional Mesh Arrays.” *Philosophical Transactions: Mathematical, Physical and Engineering Sciences* 368 (1917): 1999–2032.

Murr, L. E., S. A. Quinones, S. M. Gaytan, M. I. Lopez, A. Rodela, E. Y. Martinez, D. H. Hernandez, E. Martinez, F. Medina, and R. B. Wicker. 2009. “Microstructure and Mechanical Behavior of Ti–6Al–4V Produced by Rapid-Layer Manufacturing, for Biomedical Applications.” *Journal of the Mechanical Behavior of Biomedical Materials* 2 (1): 20–32. doi:10.1016/j.jmbbm.2008.05.004.

Murr, Lawrence E., Edwin Martinez, Krista N. Amato, Sara M. Gaytan, Jennifer Hernandez, Diana A. Ramirez, Patrick W. Shindo, Frank Medina, and Ryan B. Wicker. 2012. “Fabrication of Metal and Alloy Components by Additive Manufacturing: Examples of 3D Materials Science.” *Journal of Materials Research and Technology* 1 (1): 42–54. doi:10.1016/S2238-7854(12)70009-1.

Paul, Ratnadeep, and Sam Anand. 2015. “A New Steiner Patch Based File Format for Additive Manufacturing Processes.” *Computer-Aided Design* 63 (June): 86–100. doi:10.1016/j.cad.2015.01.002.

Pellegrino, S., and C. R. Calladine. 1986. “Matrix Analysis of Statically and Kinematically Indeterminate Frameworks.” *International Journal of Solids and Structures* 22 (4): 409–28. doi:10.1016/0020-7683(86)90014-4.

Queheillalt, Douglas T., and Haydn N. G. Wadley. 2005. “Cellular Metal Lattices with Hollow Trusses.” *Acta Materialia* 53 (2): 303–13. doi:10.1016/j.actamat.2004.09.024.

Semiatin, S. L., K. T. Kinsel, A. L. Pilchak, and G. A. Sargent. 2013. “Effect of Process Variables on Transformation-Texture Development in Ti-6Al-4V Sheet Following Beta Heat Treatment.” *Metallurgical and Materials Transactions A* 44 (8): 3852–65. doi:10.1007/s11661-013-1735-6.

Sing, S. L., W. Y. Yeong, F. E. Wiria, and B. Y. Tay. 2016. “Characterization of Titanium Lattice Structures Fabricated by Selective Laser Melting Using an Adapted Compressive Test Method.” *Experimental Mechanics* 56 (5): 735–48. doi:10.1007/s11340-015-0117-y.

Smith, C. W, J. N Grima, and K. E Evans. 2000. “A Novel Mechanism for Generating Auxetic Behaviour in Reticulated Foams: Missing Rib Foam Model.” *Acta Materialia* 48 (17): 4349–56. doi:10.1016/S1359-6454(00)00269-X.

Smith, M., Z. Guan, and W. J. Cantwell. 2013. “Finite Element Modelling of the Compressive Response of Lattice Structures Manufactured Using the Selective Laser Melting Technique.” *International Journal of Mechanical Sciences* 67 (February): 28–41. doi:10.1016/j.ijmecsci.2012.12.004.

Tan, P. J., S. R. Reid, and J. J. Harrigan. 2012. “On the Dynamic Mechanical Properties of Open-Cell Metal Foams – A Re-Assessment of the ‘simple-Shock Theory.’” *International Journal of Solids and Structures*, Proceedings of International Union of Theoretical and Applied Mechanics Symposium Mechanics of Liquid and Solid Foams, 49 (19–20): 2744–53. doi:10.1016/j.ijsolstr.2012.03.026.

Tsopanos, S., R. A. W. Mines, S. McKown, Y. Shen, W. J. Cantwell, W. Brooks, and C. J. Sutcliffe. 2010. “The Influence of Processing Parameters on the Mechanical Properties of Selectively Laser Melted Stainless Steel Microlattice Structures.” *Journal of Manufacturing Science and Engineering* 132 (4): 041011–041011. doi:10.1115/1.4001743.

Ushijima, K., W. J. Cantwell, and D. H. Chen. 2013. “Prediction of the Mechanical Properties of Micro-Lattice Structures Subjected to Multi-Axial Loading.” *International Journal of Mechanical Sciences* 68 (March): 47–55. doi:10.1016/j.ijmecsci.2012.12.017.

Ushijima, K., W. J. Cantwell, R. a. W. Mines, S. Tsopanos, and M. Smith. 2011. “An Investigation into the Compressive Properties of Stainless Steel Micro-Lattice Structures.” *Journal of Sandwich Structures and Materials* 13 (3): 303–29. doi:10.1177/1099636210380997.

Vigliotti, Andrea, and Damiano Pasini. 2013. “Mechanical Properties of Hierarchical Lattices.” *Mechanics of Materials* 62 (August): 32–43. doi:10.1016/j.mechmat.2013.03.003.

Wallach, J. C, and L. J Gibson. 2001. “Defect Sensitivity of a 3D Truss Material.” *Scripta Materialia* 45 (6): 639–44. doi:10.1016/S1359-6462(01)01073-9.

Warren, Thomas L. 1990. “Negative Poisson’s Ratio in a Transversely Isotropic Foam Structure.” *Journal of Applied Physics* 67 (12): 7591–94. doi:10.1063/1.345826.

Wielewski, E., M. R. Arthington, C. R. Siviour, and N. Petrinic. 2015. “Characterising the Effects of Strain Rate, Crystallographic Texture and Direction of Loading on the Mechanical Behaviour of Ti-6Al-4V.” *Journal of Dynamic Behavior of Materials* 1 (4): 462–71. doi:10.1007/s40870-015-0040-4.

“W.M. Keck Center for 3D Innovation.” n.d. http://keck.utep.edu/.

Yang, Li, Denis Cormier, Harvey West, Ola Harrysson, and Kyle Knowlson. 2012. “Non-Stochastic Ti–6Al–4V Foam Structures with Negative Poisson’s Ratio.” *Materials Science and Engineering: A* 558 (December): 579–85. doi:10.1016/j.msea.2012.08.053.

Yang, Li, Ola Harrysson, Harvey West, and Denis Cormier. 2012. “Compressive Properties of Ti–6Al–4V Auxetic Mesh Structures Made by Electron Beam Melting.” *Acta Materialia* 60 (8): 3370–79. doi:10.1016/j.actamat.2012.03.015.

Zhao, S., S. J. Li, W. T. Hou, Y. L. Hao, R. Yang, and L. E. Murr. 2016. “Microstructure and Mechanical Properties of Open Cellular Ti–6Al–4V Prototypes Fabricated by Electron Beam Melting for Biomedical Applications.” *Materials Technology* 31 (2): 98–107. doi:10.1179/1753555715Y.0000000056.

Zhu, Feng, Guoxing Lu, Dong Ruan, and Zhihua Wang. 2010. “Plastic Deformation, Failure and Energy Absorption of Sandwich Structures with Metallic Cellular Cores.” *International Journal of Protective Structures* 1 (4): 507–41. doi:10.1260/2041-4196.1.4.507.

Vita

Edel Arrieta earned his Bachelor of Engineering degree in Civil Engineering from the Autonomous University of Chihuahua in 2003. In 2011 he received his Master of Science degree in Civil Engineering from The University of Texas at El Paso. In 2011 he joined the doctoral program in Civil Engineering at The University of Texas at El Paso.

In 2005 he joined a design-build private firm; as a representative Project Engineer/Manager for the engineering and construction of light-industrial and commercial facilities for worldwide corporates across Mexico. He has a background in concrete, tilt-up design-construction, and business negotiation. In 2013, he left this position.

From 2014 to 2017, he worked as an instructor for the engineering measurements lab and TA for different courses including statics, dynamics, structural design, design of concrete structures, and design of steel structures for the Civil Engineering department at UTEP.

His doctoral research was presented at the international 2015 Ground Vehicle & Heavy Machinery Industry Conference and was awarded first place in the poster presentation session. In 2016, his investigation was named Top 10 worldwide university winners at the MSC Simulating Reality Contest, currently showcasing at the MSC software website. (http://www.mscsoftware.com/simulating-reality-contest-winners-2016)

He is looking forward to continue a career in the private, or academic sector, aiming to bridge knowledge between them.

Contact Information: edelarrieta@gmail.com

This dissertation was typed by *Edel Arrieta*.